Universidade de Brasília - UnB

FACULDADE DE TECNOLOGIA

MASTER'S DISSERTATION

Full-Duplex Ku-Band Phased Array Antenna Using a Compact Rotman Lens Beamformer for Satellite Communications and Radar Front-End

Jeann Feitosa Figueiredo

Brasília, DF

24 November 2021

UNIVERSIDADE DE BRASÍLIA

FACULDADE DE TECNOLOGIA

DEPARTAMENTO DE ENGENHARIA MECÂNICA

Programa de Pós-graduação em Sistemas Mecatrônicos-PPMEC

MASTER'S DISSERTATION

Full-Duplex Ku-Band Phased Array Antenna Using a Compact Rotman Lens Beamformer for Satellite Communications and Radar Front-End

Jeann Feitosa Figueiredo

Dissertação de Mestrado submetida ao Departamento de Engenharia Mecânica como requisito parcial para obtenção do grau de Mestre em Sistemas Mecatrônicos

Prof. Dr. Sébastien R.M.J Rondineau (Orientador)
Universidade de Brasília-UnB

Prof. Dr. Olympio Lucchini Coutinho
Instituto Tecnológico de Aeronáutica-ITA

Prof. Dr. Daniel Mauricio Munoz Arboleda
Coordenador do Programa de Pós-graduação em Sistemas Mecatrônicos
Universidade de Brasília-UnB

Abstract

This manuscript presents a low cost phased array antenna on Ku-band for civil and military applications, which can be used for real-time direction-of-arrival (DOA) or for communication links where energy focus and high switching beam rate are desired. Using two stacks of Rotman lenses orthogonally connected, the system performs electronic scanning in the upper hemisphere. The proposed system is completely constructed as planar low profile structure, compatible with a simple etching process which can be manufactured in a single board as a product. Measurements were taken of the system's scattering and radiation parameters at the reception and transmission frequencies, the results shown good fidelity with the simulations.

Key-words: Microstrip Antenna, Phased Array Antenna, Satellite Communications, SATCOM on-the-move, Ku-Band, Beamforming. Rotman Lens.

Resumo

Este manuscrito apresenta um arranjo de antenas banda larga cofasadas de baixo custo que funciona em banda Ku para aplicações civis e militares, pode ser usada para detecção de direção de chegada em tempo real ou para estabelecer links de comunicação. Usando duas pilhas de lentes de Rotman compactas em planos espacialmente ortogonais, o sistema proposto é totalmente construído em uma estrutura plana de baixo perfil, compatível com processo de fabricação *Sequential Build Up* o qual pode ser fabricado em uma única placa como produto.

O sistema proposto é compatível com o norma IPC-2252 para fabricação de circuitos de RF em PCB. Possui 15 feixes apontando em diferentes direções, com capacidade de varredura no hemisfério superior. Os feixes medidos estão de acordo com as simulações. Portanto, mostra-se que o sistema pode ser utilizado em aplicações móveis que precisam de alta taxa de comutação entre feixes, seja para adaptar a direção de apontamento durante o movimento do dispositivo ou para comutar o link para outro satélite. O *front-end* RF consiste de um arranjo de antenas de 4 por 4 células irradiantes, 3 lentes de Rotman 2D empilhadas de 5 entradas por 4 saídas e 4 lentes de Rotman 2D empilhadas de 3 entradas por 4 saídas.

É apresentado seis modelos de células irradiantes, entretanto somente uma foi escolhida para ser fabricada. Os projetos incluem várias técnicas para aumentar a largura de banda de impedância e de relação axial. Essas técnicas foram validadas, provando que, apesar de antenas de microfita serem intrinsicamente banda estreita, elas podem ser aprimoradas para cobrir as frequências de recepção e transmissão na banda Ku.

O ângulo de varredura das lentes do plano θ é de $\pm 31^\circ$ (elevação), e para as lentes do plano ϕ (azimute) de $\pm 29^\circ$. Os valores medidos são consistentes com os valores simulados, mesmo com as imperfeições associados ao processo de fabricação o padrão de irradiação se mostrou robusto.

A estrutura de baixo perfil foi viabilizado pela implementação da intitulada *Capacitive Coupling Transition*, a qual foi essencial em todas a placas, a transição consiste em utilizar a cola Prepreg como dielétrico entre duas placas metálicas para construir um capacitor e assim viabilizar o fluxo de potência RF. Este trabalho traz a fabricação e medição dessas transições.

List of Figures

List of Tables

List of abbreviations and acronyms

ITU	International Telecommunication Union
UnB	Universidade de Brasília
PPMEC	Programa de pós-graduação em sistemas mecatrônicos
SBU	Sequential Build Up
MVTI	Metallic Via Through Interconnections
TTD	True Time-Delay
RHCP	Right Hand Circular Polarized
LHCP	Left Hand Circular Polarized
FEM	Finite Element Method
MoM	Method of Moments
FDTD	Finite-Difference Time-Domain Method
FIR	Finite Impulse Response
DSP	Digital Signal Processing

List of Symbols and Undescripts

$\mathbf{E}$	Time-harmonic electric field vector
$\mathbf{H}$	Time-harmonic magnetic field vector
ψ	Scalar Wave Function
ϵ	Dieletric permittivity
ϵ_r	Relative dieletric permittivity
μ	magnetic permeability
arg	Complex number argument in degrees
c	Free space speed of light
λ	Wave-length
λ_0	Free space wave-length
$\mathbf{A}$	Magnetic vector potential
$\mathbf{F}$	Electric vector potential
$\boldsymbol{F}_{rad}$	Radiation vector
$\boldsymbol{F}_{dn}$	Radiation vector translated
$\boldsymbol{J}$	Current density vector
$\mathbf{r}$	Radiant element position vector
$\mathbf{d}_n$	Position vector of the translated radiating element
$\mathbf{r}_n$	Radiant element path vector
A	Array factor
$\mathbf{k}$	Angular wave-number vector

Contents

1 Introduction

Ku-band has applications in geostationary orbit satellite communications, and recently, has been used in low Earth orbit satellites, *e. g.* by SpaceX's Starlink network system (ALBULET, 2016), (FCC News, 2018). Currently, there is a great demand for communication devices at this frequency band. Moreover, it is of commercial interest to shrink the antennas to reduce weight and costs, which is another advantage of using the Ku-band, since the designs are considerably reduced in size in comparison to other satellite broadcasting bands as C-band, for example (Johannsen; Mathur, 1987). On mobile terminals for satellite communications, it is desirable to have a high directivity antenna to avoid radiation in directions out of sight of the target satellite, optimizing energy usage and reducing interference at/from other sources (ITU, 1995).

For on the move satellite communications, there is also the need for steering the beams to maintain the link during terminal movements (Alessandro et al., 2015; Xu; Xu; Jin, 2009). Some solutions, including commercial ones, are based on fixed pattern antennas mounted on mechanical pointing systems (SANETEL, 2015; Technologies, 2016; Eom et al., 2007), but those generally result in bulky structures with flaw-likely points, slow direction, and several mechanical failures. In contrast, a variety of electronically steered beam-forming systems had been presented in recent years, using digital phased arrays (Kim et al., 2019; Hamici, 2019), spatially fed lens antenna arrays figure 1 (Rondineau et al., 2006; Lee et al., 2007), dielectric lenses (Fuchs et al., 2007; Fuchs et al., 2008; Li et al., 2019; Rondineau; Himdi; Sorieux, 2003), active array fed dielectric lenses (Lafond et al., 2008; Lafond et al., 2009), holographic antennas (Zhang et al., 2019; Lv et al., 2019), or stacked lenses figures 2, 3, (REMEZ; ZOHAR,), (SCHULWITZ; MORTAZAWI, 2010), all these solutions being very bulky and/or expensive.

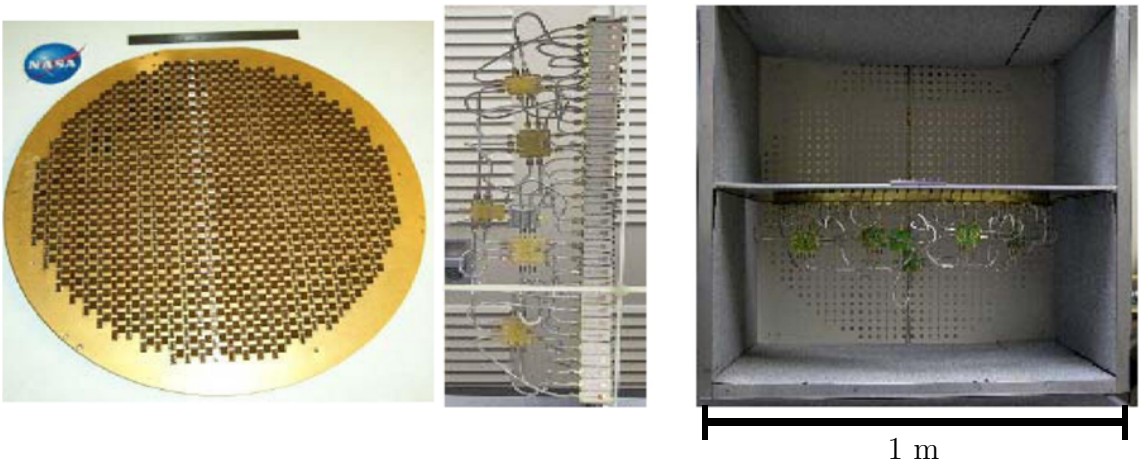

Figure 1 – Classic bulky assembly first example (Rondineau et al., 2006; Lee et al., 2007).

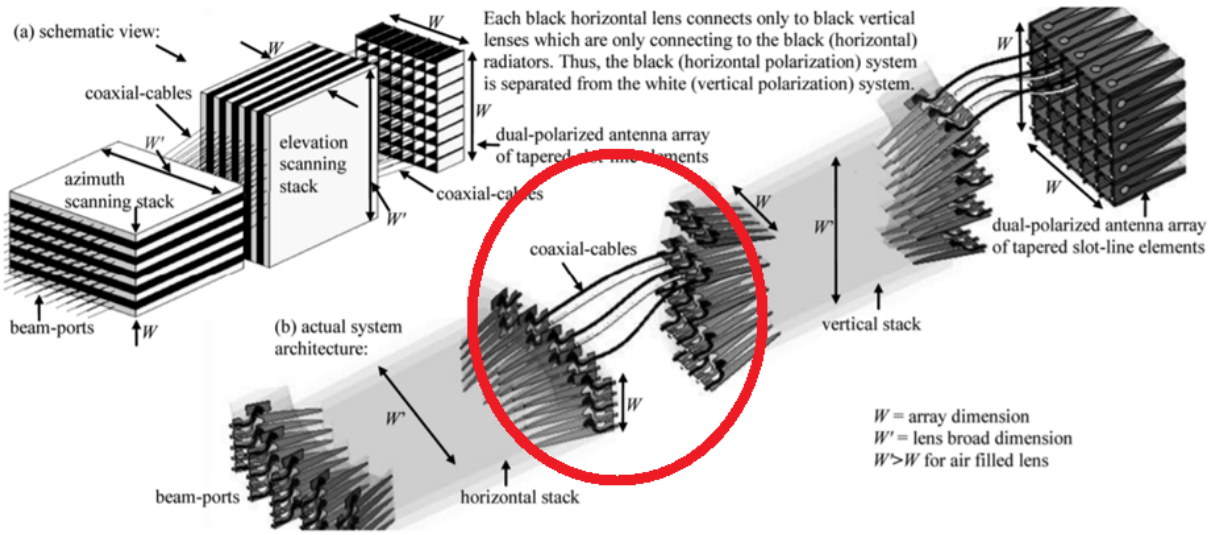

Figure 2 – Classic bulky assembly second example (REMEZ; ZOHAR,).

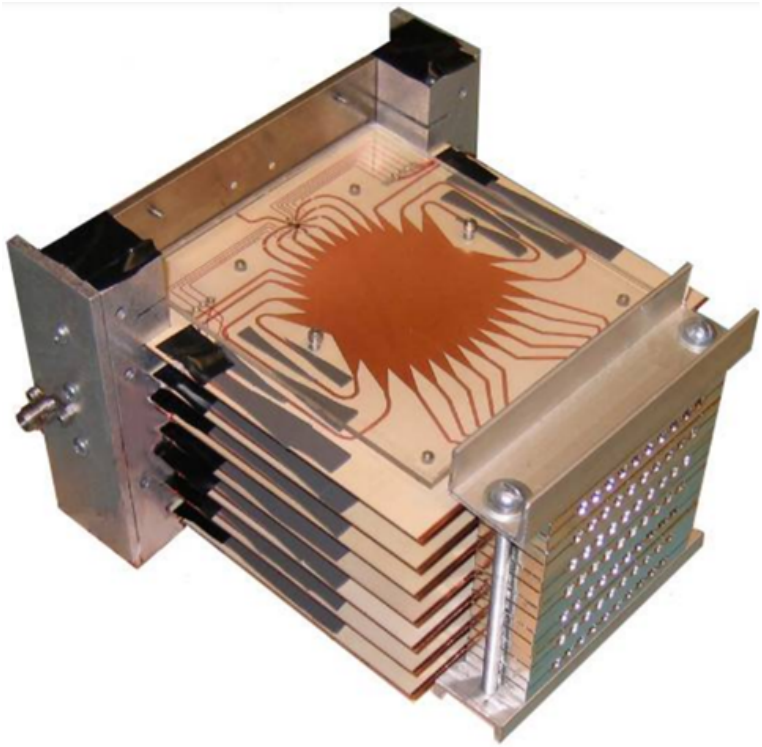

Figure 3 – Classic bulky assembly third example (SCHULWITZ; MORTAZAWI, 2010).

1.1 State-of-the-Art

The demand for high data rate in modern digital communication systems imposes a strong computational demand. In this work, the computational load of beamforming is transferred to 2D Rotman lenses, which perform discrete Fourier transforms on dedicated hardware. Beamformer's hybrid solutions have been gaining market share, but the

challenges are significant, including the large volume of digital data, the synchronization, and physical size constraints for the electronics needed behind every radiating element (DELOS, 2020).

Invented by Walter Rotman, the Rotman lens (RL) is a passive beamforming element that has a simple design and is widely used due to its robustness, ease implementation, and low cost (Rotman; Turner, 1963), (HALL; HANSEN; ABBOTT, 2002), (LEE; KIM; YOON, 2010). It mimics optical lenses by changing the phase of the impinging field through some true time delay (TTD). It has multiple inputs and outputs, allowing the operation of several simultaneous beams, as well as the use of Electronically Scanning Arrays (ESA) technology. By being flat, it reduces the size of the set as a whole (Sakakibara et al., 2018), (Hall; Vetterlein, 1990). Also, the Rotman lens can be seen as a waveguide, where the wave lag occurs in its cavity, i. e. it is a TTD circuit, it is robust and reliable concerning pointing directions, besides, the beam is oriented regardless of the operating frequency, the TTD behavior enables squint-free operation (LAMBRECHT; BEER; ZWICK, 2010), (Rahimian, 2010), (WEISS; KELLER; LY, 2006). Dual plane scanning using a discrete lens is proposed in (Zhou et al., 2005), (McGrath, 1986). Although it is reasonably light, the power combining is done in free space, turning this architecture not suitable for low profile applications because it occupies an exceedingly large volume. Due to its two-dimensional geometric nature, RL allows scanning in one spatial plane. To form the beams in two planes (elevation and azimuth) it is necessary to have two orthogonal sets of lenses.

1.2 Contributions

It is proposed a phased array antenna composed of two sets of Rotman lenses, designed to operate full-duplex at Ku-band, covering both reception and transmission frequency bands. The system has 15 pre-defined beams, selected by an RF switch matrix (not developed by this work) that routes the signal towards the corresponding port of the desired beam. The Rotman lenses are connected to achieve beam steering based on orthogonal spatial planes, thus having the beam directions as a combination of the angles in both planes. A unique feature about the system proposed in this work is the assembly scheme, which differs from other orthogonal Rotman lenses setups (European Space Agency, 2020), (Babar Abbasi; Fusco; Matthaiou, 2019), consisting of an entirely planar structure with all layers boards mounted in parallel planes. All the needed layer interconnections combinations in this structure are turned possible after the implementation of a capacitive radiofrequency coupling, which consists of a work-around on drilling limitations of the industrial manufacturing process. Therefore, the solution as a whole turns out to be an adequate option for mobile land terminals and radar front-end, given the mechanical robustness provided by a compact low profile structure. Moreover, the same connection scheme can be used to construct the whole system in one single board, which

makes it viable for large-scale production, hence, dramatically reducing product manufacturing costs. For the development of the elementary antenna, it is also necessary to take advantage of the same layer interconnections concept. Furthermore, some advanced techniques of patch antenna design are used to ensure coverage TX and RX satellite communication spectrum of the Ku-band using a single antenna that can work with the two circular polarizations (LHCP and RHCP) at the same time and frequency. The proposed approach allows a fast beam steering, providing robust assembly and stable link.

1.3 Objective

1.3.1 General Objective

To deliver a full-duplex RF system for satellite communication and radar front-end in Ku-band of low cost, low profile and compatible with *Sequential Build Up* (SBU) large-scale printed circuit fabrication technology.

The system must be able to focus electromagnetic radiation in predetermined directions to optimize the signal to noise ratio (SNR) without employing mechanical actuators.

1.3.2 Specific Objectives

- Design an antenna that features circular polarization.
- Design a phased array antenna.
- Design dedicated hardware for beamforming.
- Design a stack of Rotman lenses.
- Fabrication of individuals prototypes and integration of components that enables to validate a proof of concept.

1.4 Dissertation Structure

This work has 6 parts: Introduction, Capacitive Coupling Transition, Elementary Microstrip Antenna, Beamformer, Phased Array Antenna, Conclusion, Bibliography, organized as follow:

- Capacitive Coupling Transition: Chapter 2 describes a solution for non-standard metallic via through interconnection (MVTI) to attend capabilities of standard PCB

manufacturing processes, permitting the construction of the architecture proposed later;

- Elementary Microstrip Antenna: Chapter 3 expose four antenna design, including geometry, performance curves and design tips, which make use of several techniques to improve impedance and axial bandwidth of microstrip antennas;
- Beamformer: Chapter 4 presents the characteristics of the designed Rotman lenses and details some critical design variables and techniques that enhance performance over the desired bandwidth, as well as details the beam-forming architecture and the novel orthogonal Rotman lenses assembly that resulted in a planar low profile structure;
- Phased Array Antenna: Chapter 5 presents the manufactured Phased Array Antenna, the complete radiating system, the measurement setup as well as the measured and simulated results;
- Conclusion: Chapter 6 concludes with some considerations about the system's performance, and suggestions for future work.

2 Capacitive Coupling Transition

This chapter presents the component created to electrically connect layers of a multi-layer board, it also presents the inherent limitation of the SBU technology which motivated the development of the presented component titled capacitive coupling transition. The entire architecture has been manufactured following the IPC-2252 standard for industry, resulting in the PCBs shown in the Figures 4, 35, 62, 61. The characterization of each board has been carried out and is presented as follows.

2.1 *Sequential Build Up* Technology

During the definition of the antenna array and lens ensemble stack-up, it has been observed the need for a complex combination of different types of metallic via through interconnections (MVTI), shown by the cut planes in Figure 32.

Due to the capabilities of the standard PCB fabrication process, the *Sequential Build-Up* technology (Ho, 1997; Blackshear, 2005), simple blind vias can not be used in that specific combination. There cannot be an intersection, for example, MVTIs that start in the first layer and end in the third, cannot be manufactured with MVTIs that start in the second layer and end in the fourth layer. Thus, there are constructed sets of discrete MVTIs electrically connected by capacitive gaps, then any kind of layer interconnection can be done using combinations of these discrete structures. This feature is achieved using aligned blind and buried MVTIs at each layer of the stack and terminating them with parallel circular plates. Since the individual layers are pressed together with a gluing Prepreg layer that polymerizes with heat, the plate terminations become parallel plates spaced by a dielectric (Prepreg), as shown in Figure 4, turning it into a capacitor. All the presented designs comply with the IPC-2252 standard for industrial microwave printed circuit board manufacturing processes.

Proceeding with this idea, it is necessary to select thin Prepreg, here 76 μm[1] thick (around $\lambda_0/300$) to improve the coupling between the two plates and reduce dielectric losses through all the layers. Indeed it is desirable to have the thinnest Prepreg possible, at the price of a very sensitive transmission line impedance to the manufacture process errors.

The reflection coefficient is degraded when the signal MVTI diameter is increased (Dong et al., 2017), so it is chosen as the small drilling diameter (150 μm), but still in

[1] The manufacturer recommends the use of two layers of Prepreg on each pressing step. The individual film thickness is 38 μm.

agreement with the IPC-2252 standard.

At the stripline layer, where the signal is routed, there is the last plate termination, which also presents a capacitive behavior. This is compensated by an immediate inductive section. It is necessary to match the impedance to the 50 Ω, it is used a quarter-wavelength stripline transition, as depicted in Figure 4. A chamfer at the quarter-wavelength section significantly improves the impedance matching in the overall bandwidth.

The relation between plate radius and coupling efficiency is directly related to the signal wavelength, therefore the radius is fixed to 0.56 mm as a compromise to fit both reception and transmission bands with satisfactory performances. This is the most sensitive variable in the whole transition design, producing a maximum variation of 0.5 dB on the transmission coefficient at higher frequencies.

It is needed to place GND MVTIs around the signal via, creating a coaxial transition and avoiding radiation leakage (Tsai et al., 2011). Also, an SMA connector matching structure is designed, consisting of a semi-circle of blind ground MVTIs around the signal path (Pawlak M. S. Reuther, 2007).

It is desired to have a low phase difference between paths to avoid adding phase error to the lenses, and thus keep the pointing angles as projected. The layout of the connections (Figure 32) intrinsically keeps a uniform delay, because the relative lag at the stripline entries added by the different path lengths of the first set o transitions is compensated by the second set at the output. Nevertheless, some critical design parameters were optimized to ensure this uniformity. Being the distance of shielding MVTIs from the stripline and the chamfer length (Figure 4) the key variables to tune this effect.

Regarding manufacturing, as shown in Figure 5, it is estimated a 75 μm misalignment between fabricated signal capacitive MVTIs, but the simulations performed show that this does not represent a significant impact on system performance, as depicted in Figure 5. Thus, the transition has a tolerable performance for layer misalignment until 200 μm.

The substrate used is the RO4730G3, with dielectric constant $\epsilon_r = 3$, thickness $h = 0.526$ mm, and loss tangent $\tan\delta = 0.0029$. The Prepreg layers are Bondply 2929, with $\epsilon_r = 2.94$, $h = 0.038$ mm, $\tan\delta = 0.003$. The same materials are used in the antenna and Rotman lenses.

In one of the boards (Figure 35), it is placed a set of transitions for characterization. It consists of 4 different stripline paths, each one passing through one layer, precisely as it is at the ports of the Rotman lenses stack, but in this case, using 50 Ω striplines with 44.5 mm length to connect the ports of the transitions. The cut planes in Figure 32 depicts the routing scheme of this structure. On one side the ports are identified as {J30, J31, J34, J35} (Figure 34), and are respectively connected to ports {J29, J32, J33, J36} at

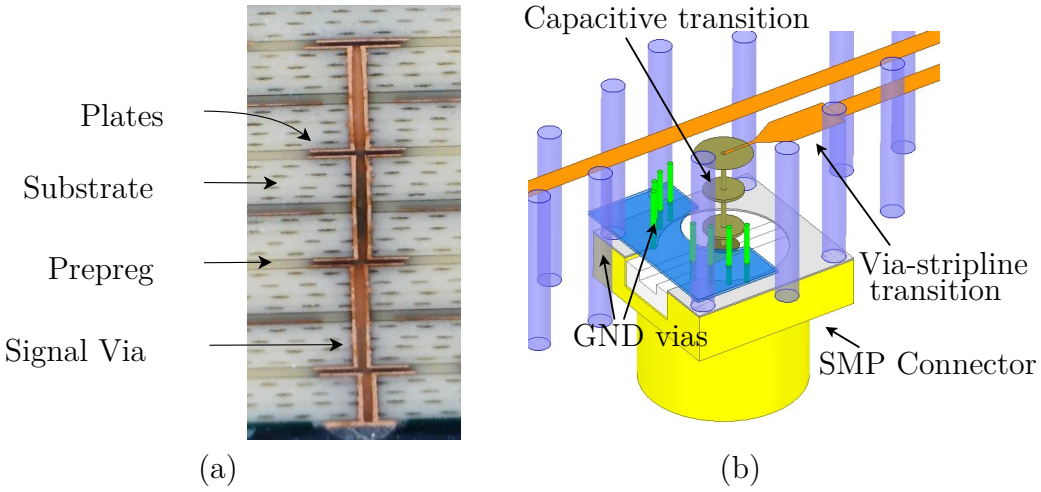

Figure 4 – Capacitive multilayer via-stripline transition. (a) Transverse cut of the manufactured capacitive MVTI. (b) Isometric view of the capacitive transitions. The signal couples between parallel plates spaced by the PCB Prepreg. It is necessary to design an impedance matching section to connect it to the stripline, as well as at the connector pin. There are used GND thru MVTIs around the structure to stabilize potentials all through the transition height.

the opposite side.

The use of this contactless multi-layer transition allows for some critical components used either in the antenna stack-up such as the *Feed* shown in figure 10, and in the specific routing setup proposed on the Rotman lenses stacks.

2.2 Results

The S-parameters of the capacitive transitions with 50 Ω striplines are presented in Figure 6. It shows an average insertion loss of 1.9 dB. Also, the transmission coefficient does not present large variation between paths, proving that the transitions are robust to the manufacturing variations, as predicted by the yield analysis.

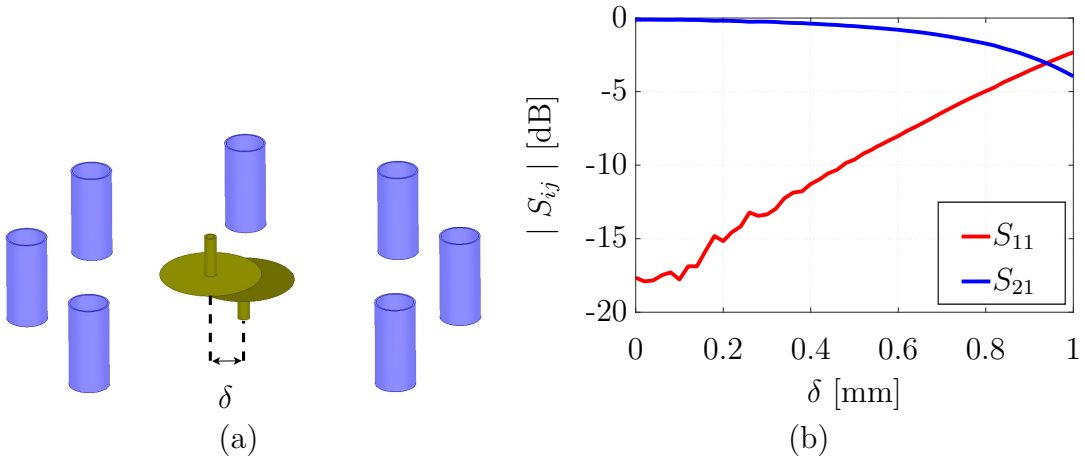

Figure 5 – (a) Misalignment simulation setup. (b) Misalignment effect on S-parameters. The 75 μm misalignment between plate layers does not produce a significant impact on the overall system performance.

The phase difference between paths observed in Figure 7 reaches 8.7°, with an average of 3.8° inside the band of interest. This low phase difference between paths is necessary to avoid adding phase error to the phased array, thus preserving the predicted beam shapes and pointing directions.

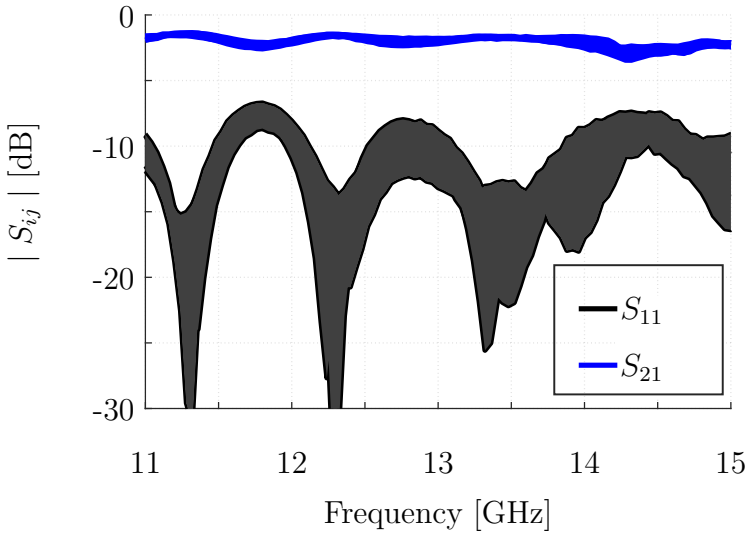

Figure 6 – Envelopes between maximum and minimum measured S-parameters of capacitive transitions. Insertion loss with an average of 1.9 dB.

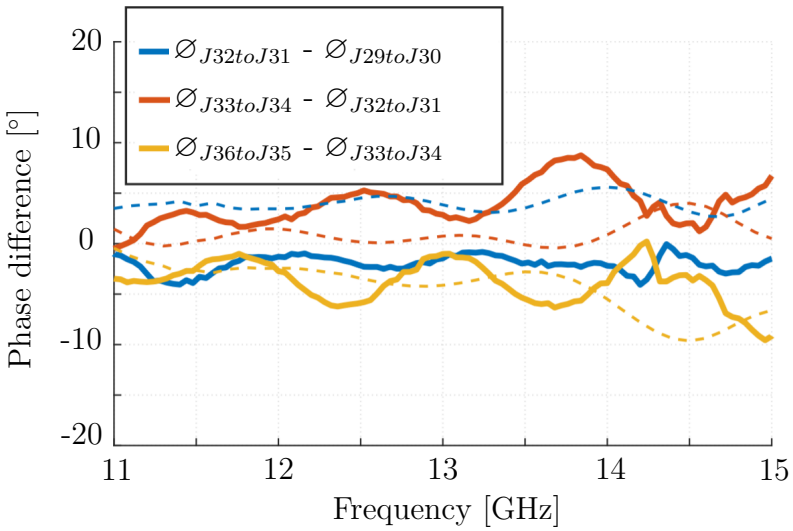

Figure 7 – Phase difference between paths. The average phase difference of 3.8° and worst case 8.7° at 14 GHz. Dashed lines: simulation. Solid lines: measurements.

3 Elementary Microstrip Antenna

The increase in frequency has been reducing the size of the antennas, enabling the possibility of having an array of high directivity in a small area. A full duplex broadband antenna array with electronic scanning capability has a wide range of applications in modern problems such as mobile satellite communications, radar, jammers. It has been shown to be a good choice for aeronautic and aerospace conditions such as aircraft, rocktes and missiles.

In printed antennas, narrow bandwidth, low efficiency, high quality factor are observed (Balanis, 2016a). This technology, however, presents a high degree of freedom in the the metal shape, being an important parameter to mitigate these disadvantages.

3.1 Microstrip Antenna Theory

3.1.1 Ressonant Cavity

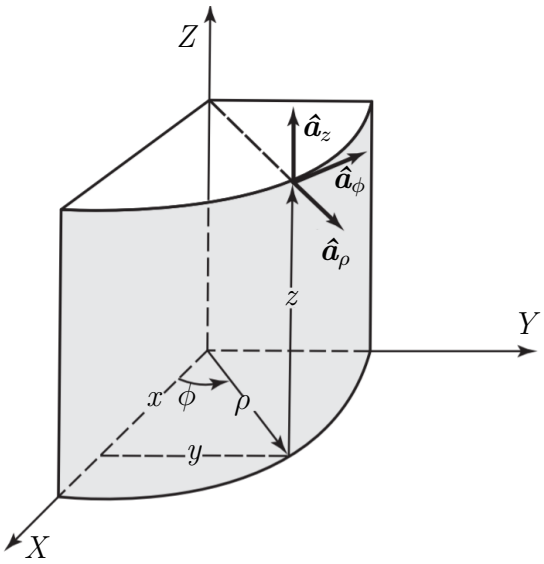

Figure 8 – Cylindrical coordinate system with corresponding unit vectors.

For Linear, homogeneous, isotropic and source-free medium, fields be write as,

$$-\nabla \times \mathbf{E} = \mu \frac{\partial \mathbf{H}}{\partial t}, \tag{3.1}$$

$$\nabla \times \mathbf{H} = \epsilon \frac{\partial \mathbf{E}}{\partial t}, \tag{3.2}$$

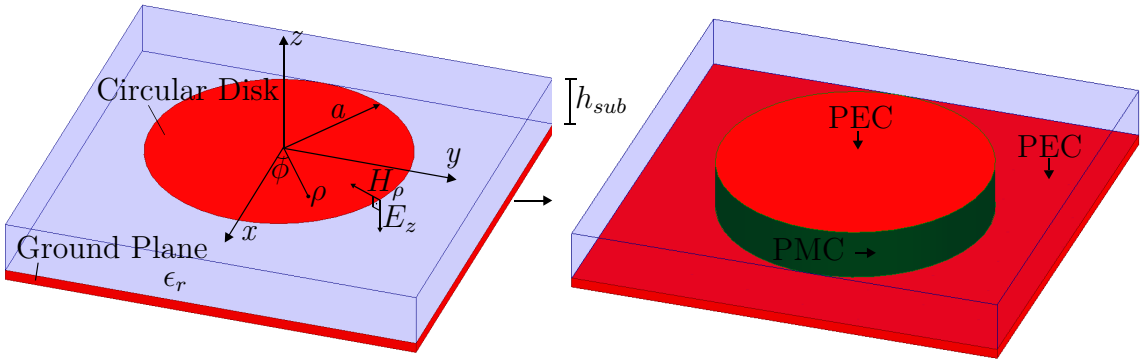

Figure 9 – Microstrip Antenna

$$\nabla \cdot \mathbf{H} = 0, \tag{3.3}$$

$$\nabla \cdot \mathbf{E} = 0. \tag{3.4}$$

Using auxiliary vector $\mathbf{A}$ for magnetic potential, and $\mathbf{F}$ for electric potential, defined below in the equations 3.5 and 3.6.

$$\mathbf{H} = \nabla \times \mathbf{A} \tag{3.5}$$

$$\mathbf{E} = -\nabla \times \mathbf{F} \tag{3.6}$$

Putting in for time harmonic ($\frac{\partial}{\partial t}$ becomes $j\omega$),

$$\mathbf{E} = -\nabla \times \mathbf{F} + \frac{1}{j\omega\epsilon} \nabla \times \nabla \times \mathbf{A}, \tag{3.7}$$

$$\mathbf{H} = \nabla \times \mathbf{A} + \frac{1}{j\omega\mu} \nabla \times \nabla \times \mathbf{F}, \tag{3.8}$$

$$\mathbf{E} = -\nabla \times \mathbf{F} - j\omega\mu\mathbf{A} + \frac{1}{j\omega\epsilon}\nabla(\nabla \cdot \mathbf{A}), \tag{3.9}$$

$$\mathbf{H} = \nabla \times \mathbf{A} - j\omega\epsilon\mathbf{F} + \frac{1}{j\omega\mu} \nabla(\nabla \cdot \mathbf{F}). \tag{3.10}$$

Applying the boundary condition $\mathbf{H}_z = 0$, ie transverse magnetic to z (TM^z), this implies $\mathbf{F} = 0$ and $\mathbf{A} = \hat{\mathbf{a}}_z\psi$.

$$\mathbf{E} = -j\omega\mu\mathbf{A} + \frac{1}{j\omega\epsilon} \nabla(\nabla \cdot \mathbf{A}) \tag{3.11}$$

Using ψ in cylindrical coordinates,

$$E_\rho = \frac{1}{j\omega\mu\epsilon}\frac{\partial^2\psi}{\partial\rho\,\partial z}, \tag{3.12}$$

$$E_\phi = \frac{1}{j\omega\mu\epsilon\rho}\frac{\partial^2\psi}{\partial\phi\,\partial z}, \tag{3.13}$$

$$E_z = \frac{1}{j\omega\mu\epsilon}\left(\frac{\partial^2\psi}{\partial^2 z} + k^2\psi\right), \tag{3.14}$$

$$H_\rho = \frac{\partial\psi}{\mu\rho\,\partial\phi}, \tag{3.15}$$

$$H_\phi = -\frac{1}{\mu}\frac{\partial\psi}{\partial\rho}, \tag{3.16}$$

$$H_z = 0. \tag{3.17}$$

For the geometry shown in figure 9, interesting boundary conditions are perfect electric conductor (PEC) for the Circular Disk and the Ground Plane, and perfect magnetic conductor for the z-bounded plane by the upper PEC (circular disk) and lower PEC (ground plane) sweeping the entire axis ϕ with constant radius a.

Due to the proximity between the Circular Disk and the Ground Plane, we can assume that E_z is constant along z.

The slits radius will be a little bigger than the a radius because of fringing fields not considered in the model. Analytical approximations based on the cavity method for fringing fields can be found at (Balanis, 2016b).

Substituting in the equation C.42, where J_m is the cylindrical Bessel function, leads to,

$$E_z = C_1 J_m(k_\rho\rho)C_4\cos(m\phi). \tag{3.18}$$

Where k_ρ is related to the wave-number k ($k \equiv \frac{2\pi}{\lambda}$) and the separation constant k_z defined in C.11 by equation,

$$k_\rho^2 = k^2 - k_z^2. \tag{3.19}$$

Defining $E_0 \equiv C_1C_4$ the equation remains,

$$E_z = E_0 J_m(k_\rho \rho)\cos(m\phi). \tag{3.20}$$

The magnetic field component stays,

$$H_\rho = \frac{j}{\rho\mu\omega}\frac{\partial E_z}{\partial \phi}, \tag{3.21}$$

$$H_\rho = -\frac{jm}{\rho\mu\omega} E_0 J_m(k_\rho \rho)\sin(m\phi), \tag{3.22}$$

$$H_\phi = -\frac{j}{\mu\omega}\frac{\partial E_z}{\partial \rho}, \tag{3.23}$$

$$H_\phi = -\frac{jk_\rho}{\mu\omega} E_0 J'_m(k_\rho \rho)\cos(m\phi). \tag{3.24}$$

Inside the cavity the following field components cancel each other out,

$$\sqrt{\frac{\mu}{\epsilon}}\, H_z = E_\rho = E_\phi = 0. \tag{3.25}$$

Observing Ampère law, H_ϕ is approximately zero along the edge ($\rho = a$) because the normal component of the electric current (in the direction of $\hat{\mathbf{a}}_\rho$) is null. Looking at the equation 3.24 H_ϕ can be zero if and only if $J'_m(k_\rho a) = 0$ for any ϕ. The roots of the Bessel equation are tabulated (table A), for the fundamental mode $m = 1$, $k_\rho a = 1.84118$. Resonance frequency (f_r) may be write as,

$$f_r = \frac{1.84118}{2\pi a\sqrt{\mu\epsilon}}. \tag{3.26}$$

3.2 Microstrip Antennas on Ku Band

3.2.1 Circular Microstrip Broadband

Microstrip antenna typically achieves less than one percent of impedance bandwidth (Balanis, 2016a). However, this work achieved 25% of impedance bandwidth.

The antenna array represents an essential component of the system. Therefore, lots of attention has been put in its design to ensure its performances in terms of s-parameters, axial ratio (AR) and radiation pattern, considering errors of classical RF industrial PCB manufacture process.

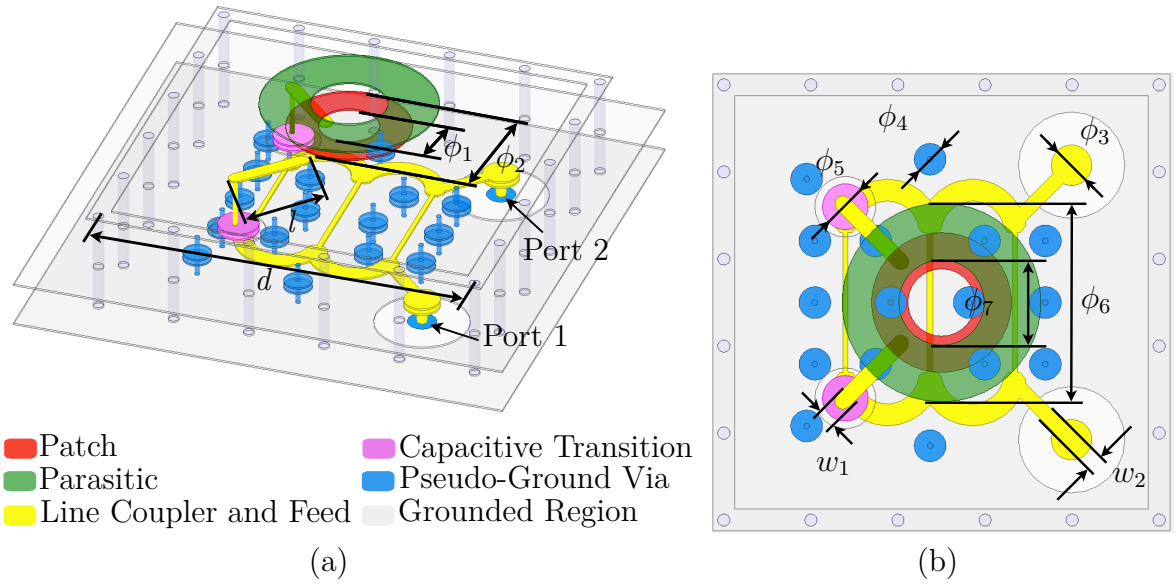

Figure 10 – A circular patch visible in red, right below the parasitic element in green on the upper side. The MVTI in pink and blue. It is also drawn two feeds with a 90° rotation in yellow. On the bottom side in yellow is shown a three branch line coupler made in stripline that generate 90° electrical difference.

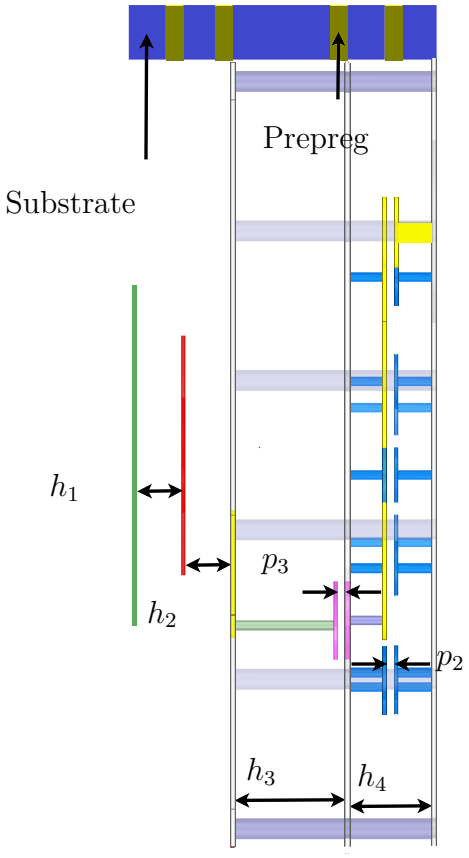

Figure 11 – Side view of the antenna model with the heights, and the stack structure with the substrate indicated in blue and the prepreg in yellow.

Table 1 – Design Parameters.

ϕ_1	1.77	ϕ_4	0.84	ϕ_7	2.25	$h1, h2$	0.60	l	2.16
ϕ_2	3.68	ϕ_5	1.20	d	11.45	h_3	1.60	w_1	0.44
ϕ_3	1.07	ϕ_6	5.23	$p2, p3$	0.076	h_4	1.13	w_2	0.38

Note: parameters are given in [mm].

It is designed as a circularly polarized patch antenna with a parasitic element to improve the impedance bandwidth since it adds resonant frequencies and reduces the antenna quality factor. Usually, the spacing between the patch and parasitic is done using post-mounted air gap spacers (Wu; Y.Lou; Yung, 2007), (Cheung et al., 2017), (Parikh; Pandey; Modh, 2012). However, to avoid manual processes and to ensure repeatability of the manufacturing process, the spacing is done with a Prepreg and a substrate layer of thicknesses 0.076 mm and 0.508 mm, respectively. Yield analysis were carried out to ensure the robustness of the model to the manufacturing process. The patch and the parasitic element have a central hole, as shown in Figure 10, to improve impedance matching.

3.2.1.1 Three Branch Line Coupler Design

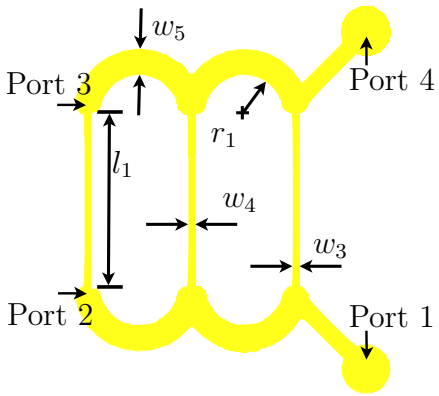

Figure 12 – Model of the 3 dB three-branch line coupler its pertinent widths and lengths.

The scattering parameter matrix of the coupler may be written as,

$$[S_{ij}] = \begin{bmatrix} S_{11} & S_{21} & S_{31} & S_{41} \\ S_{21} & S_{11} & S_{41} & S_{41} \\ S_{31} & S_{41} & S_{11} & S21 \\ S_{41} & S_{31} & S_{21} & S_{11} \end{bmatrix}.$$

In ideal behavior the matrix is,

$$[S] = \frac{1}{\sqrt{2}} \begin{bmatrix} 0 & j & 1 & 0 \\ j & 0 & 0 & 1 \\ 1 & 0 & 0 & j \\ 0 & 1 & j & 0 \end{bmatrix}.$$

Where

$$|S_{11}|^2 + |S_{21}|^2 + |S_{31}|^2 + |S_{41}|^2 = 1, \tag{3.27}$$

and

$$|S_{11}|^2 = |S_{41}|^2 = 0, \quad |S_{21}|^2 = |S_{31}|^2 = 0.5, \quad \arg(S_{21}) - \arg(S_{31}) = 90°. \tag{3.28}$$

The design of the *Three Branch Line Coupler* (or for convenience simply coupler) followed the steps:

- Choose substrate thickness. For thick substrates imply a low quality factor Q that can degrade the return loss and the insulation, it can also appear lowest order TM surface waves at high operating frequencies. Thick substrate can also limit the minimum linewidth (highest impedance) although it is more often limited by the capability of the printed circuit manufacturer. Larger linewidth (smaller impedance) are usually limited by unwanted appearance of transverse waves.
- Find the track impedances that approximate performance specified in equation 3.28 across the requested bandwidth. For this, the Advanced System Design (ADS) software was used, using the *Grandient Minimax* optimization algorithm. In this step, the ideal transmission line component (TLIN) was used, whose main input parameters are impedance, electrical length and frequency.
- In this step we repeat the optimization of the previous step, but now replacing the ideal transmision line (TLIN) by stripline component (SLIN), whose main input parameters are, substrate characteristics, linewidth and length.
- Having the dimensions, the coupler was remodeled in a ADS full-wave simulation environment, using the MoM method. Optimizations are run with the goals shown in equation 3.28.
- The Coupler was remodeled in the Ansys HFSS software and added to the antenna model as shown in Figure 10. The last optimizations generated the dimensions shown in the Table 1.

A *Three Branch Line Coupler* (TBLC) is connected to the antenna feeding points because it splits the power and add 90° phase shift between those two ports to create circular polarization. Traditional hybrid couplers do not deliver required bandwidth for this project, but with the three-branch architecture, the bandwidth is increased by creating two resonances (Muraguchi; Yukitake; Naito, 1983). Indeed, due to isolation between ports 1 and 4 of the coupler (shown in figure 12), the antenna can operate at Right-Handed Circular Polarization (RHCP) and Left-Handed Circular Polarization (LHCP) at the same time and frequency, the corresponding input port of the coupler. That means the possibility of two independent channels with the same radiating element. The isolation between the two channels is sensitive to the TBLC lines width, which consequently impacts the axial ratio. By increasing the widths w_3 and w_4, the AR is increased for lower frequencies bands and decreased at the high ones. Therefore, it is necessary to tune it in order to balance those effects. To avoid coupling between the TBLC and other elements of the circuit and to have a stacked structure, the coupler is placed on an exclusive stripline layer under the patch. Given its connections with the patch and the connectors simultaneously, it is required to use the capacitive transition described in chapter 2 to turn it industrially manufacturable. Moreover, given the lack of possible drilling, the transitions are also used to virtually connect ground planes at both sides of the coupler layer, by the called *pseudo-ground via through interconnects* in Figure 10, forcing equipotential grounded planes. Because of those transitions, the TBLC becomes sensitive to the Prepreg thickness, with slight performance degradation at the reception band, since the capacitive coupling is intrinsically weaker for lower frequencies.

The Figures 13, 14 and 15 show the simulated spreading parameters of the TBLC. Figure 13 shows the imbalance observed between ports 2 and 3 (reference in Figure 12), in the worst case at 14.5 GHz, the imbalance reached 0.39 dB. The phase between ports 2 and 3 got worse at 11.7 GHz, deviating only 2.77°. These are important metrics to generate pure circular polarization of the antenna.

In Figure 14, $|S_{41}|$ is the coupling between ports 1 and 4, together with the metric $|S_{11}|$ ensures that the power level is returning is within the operational limit without generating feedback and unwanted oscillations, both were better than -15 dB across the range.

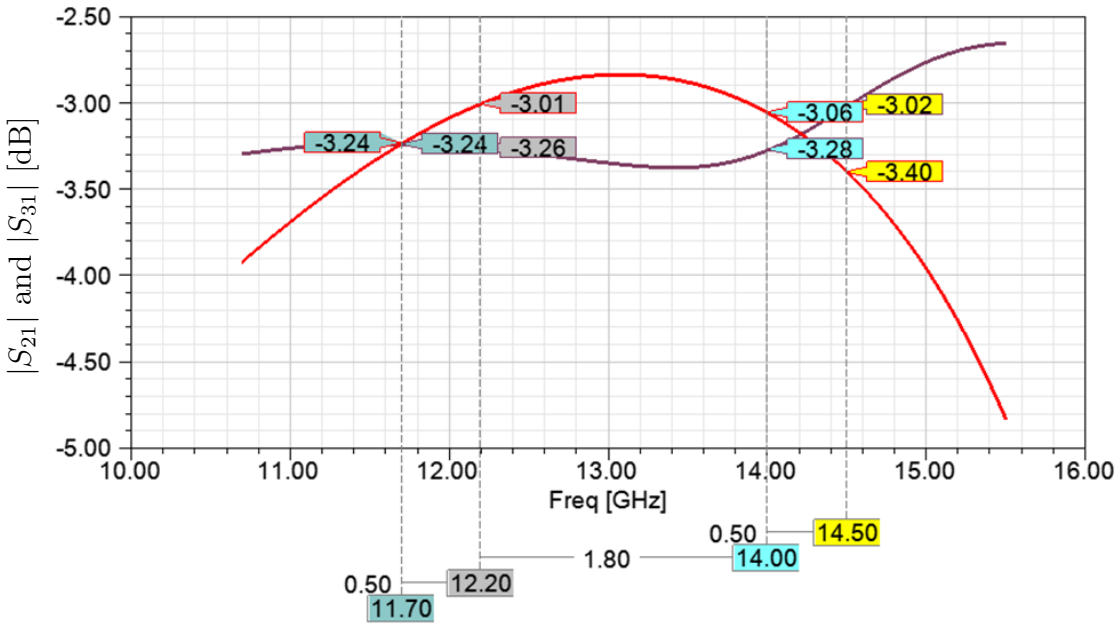

Figure 13 – Broadband behavior of the *Tree Branch Line Coupler*. The worst unbalance is observed at 14.5 GHz of approximately 0.38 dB.

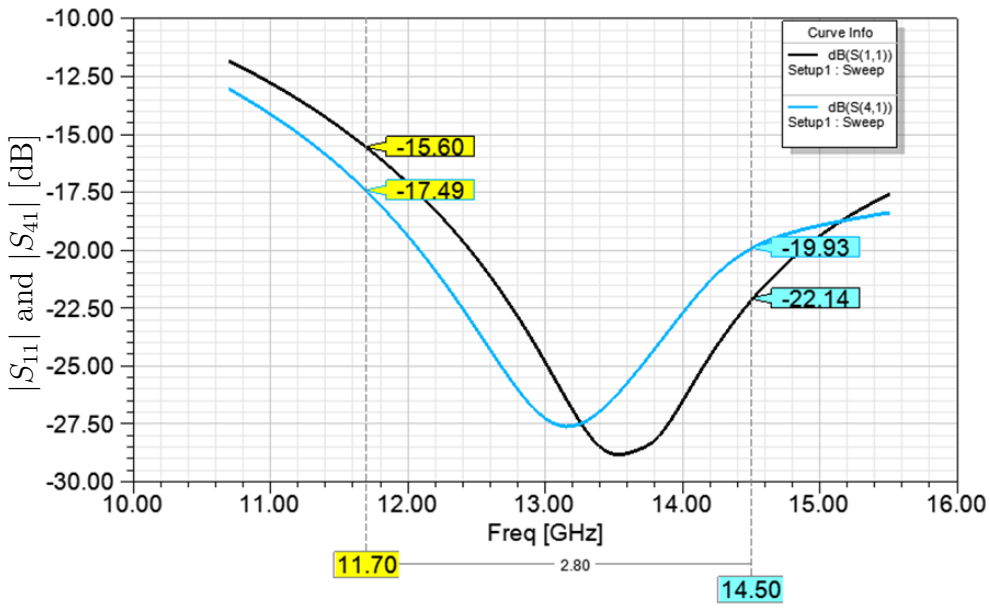

Figure 14 – Black color the impedance matching ($|S_{11}|$) and in blue the isolation ($|S_{41}|$) between ports 1 and 4 of coupler.

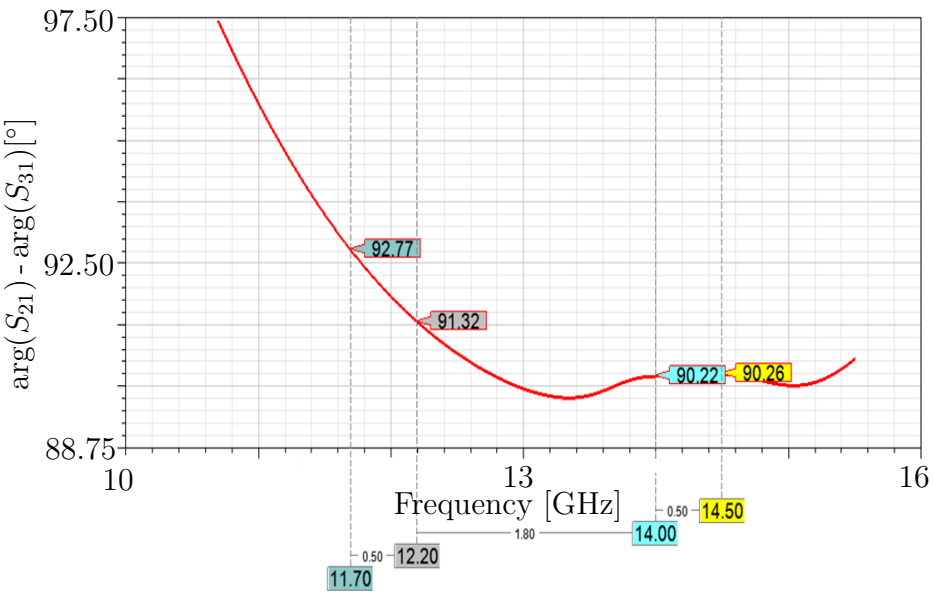

Figure 15 – Coupler broadband phase shift between output ports.

3.2.1.2 Antenna Performance

The elementary antennas are organized in a 4×4 array with a $\lambda_0/2$ spaced rectangular grid, designed at the central frequency $f_0 = 13.1\,\text{GHz}$.

For each elementary antenna in the array, GND MVTIs were placed up to the same level as the patch to surround the elements, separating them from each other. These electrical walls create a cavities-like effect which prevents some possible surface waves from flowing, and so drastically reducing any coupling effect between nearby antennas in the array. An analysis has been carried out to show that it is required to have at least 5 ground MVTIs at each side of the elementary antenna to reach a $-25\,\text{dB}$ inter-element decoupling.

Two arrays have been manufactured, as shown in Figure 62, to evaluate the effects of construction variations in the measurements.

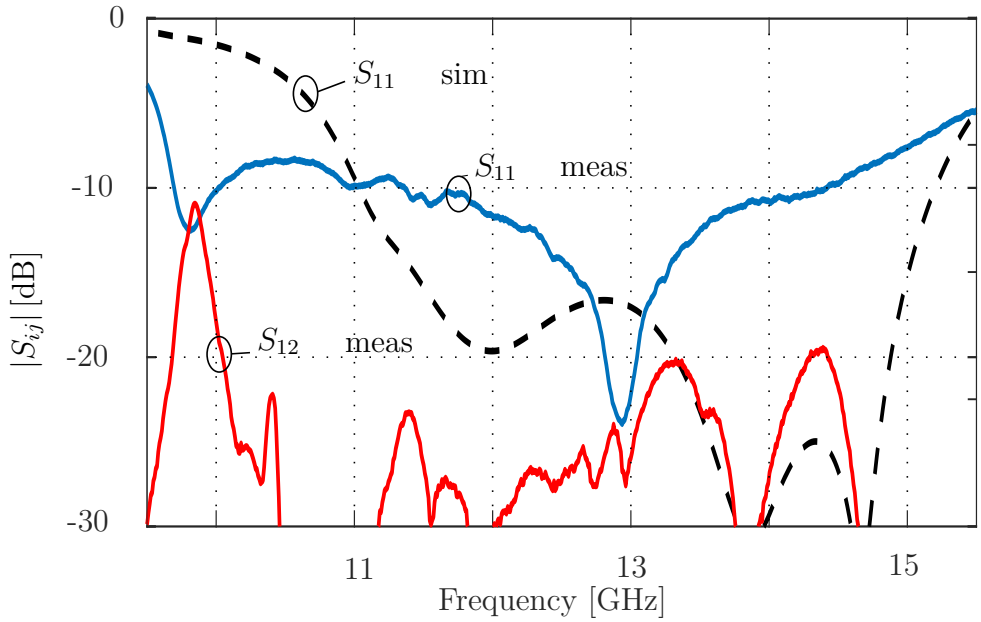

Figure 16 – Measured reflection coefficient of the elementary antenna in blue. In red, the measured isolation between adjacent elementary antennas. Even with the uncertainties from the manufacturing process, the antenna showed about 25% of impedance bandwidth (IBW), ranging the desired frequency band 11.3 - 14.5 GHz.

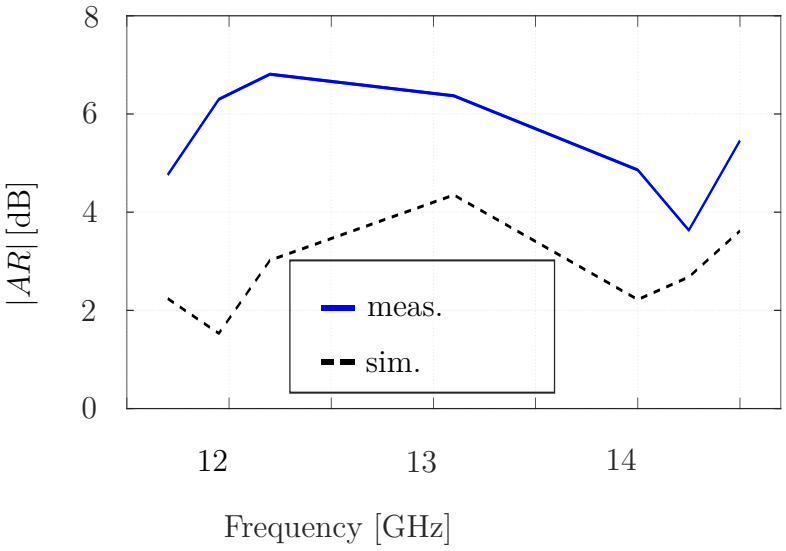

Figure 17 – Measured and simulated AR of the elementary antenna. The AR is strongly dependent on the widths of the *Three Branch Line Coupler* (TBLC) tracks. As shown in (George; Castro; Sharma, 2017) and (Hall, 1989), AR and reflection coefficient falls significantly when applied sequential rotation.

Figure 16 shows the antenna S-parameters, with a measured reflection coefficient better than -10 dB from 11.3 to 14.5 GHz. S_{21} parameter shows that the antennas on the array are decoupled. Figure 17 presents the AR of the elementary antenna, which is slightly above expected, given the uncertainty associated with the manufacturing process. As shown in (George; Castro; Sharma, 2017) and (Hall, 1989), AR and reflection coefficient falls significantly when applied sequential rotation. Therefore it is a point to be considered for any future solution.

3.2.2 Dual-Band Patch with Bents Slots

Even among microstrip antennas, the antenna entitled *Dual-Band Patch with Bents Slots* stands out for its low cost, requiring only one layer of substrate. As shown in figure 19 the antenna works from 11.7 to 12.2 GHz, and from 14 to 14.5 GHz.

The antenna has two linear polarizations, one for transmission and one for reception. In mobile applications where the possibility of antenna rotation must be assumed and, consequently, polarization losses become severe in antennas with linear polarization. In this case sequential rotations of elementary cells antenna attenuate the loss.

Table 2 – Design Parameters of *Dual-Band Patch with Bents Slots*

W_{slot}	6.69	L_{slot}	5.15	$p1_{slot}$	1.38	$p2_{slot}$	1.23	SL_{slot}	4.53
w_{slot}	0.24	s_{slot}	0.31	ϵ_r	2.5	-	-	-	-

Note: parameters are given in [mm]. Laminate Rogers AD250C of thickness 1.524 mm.

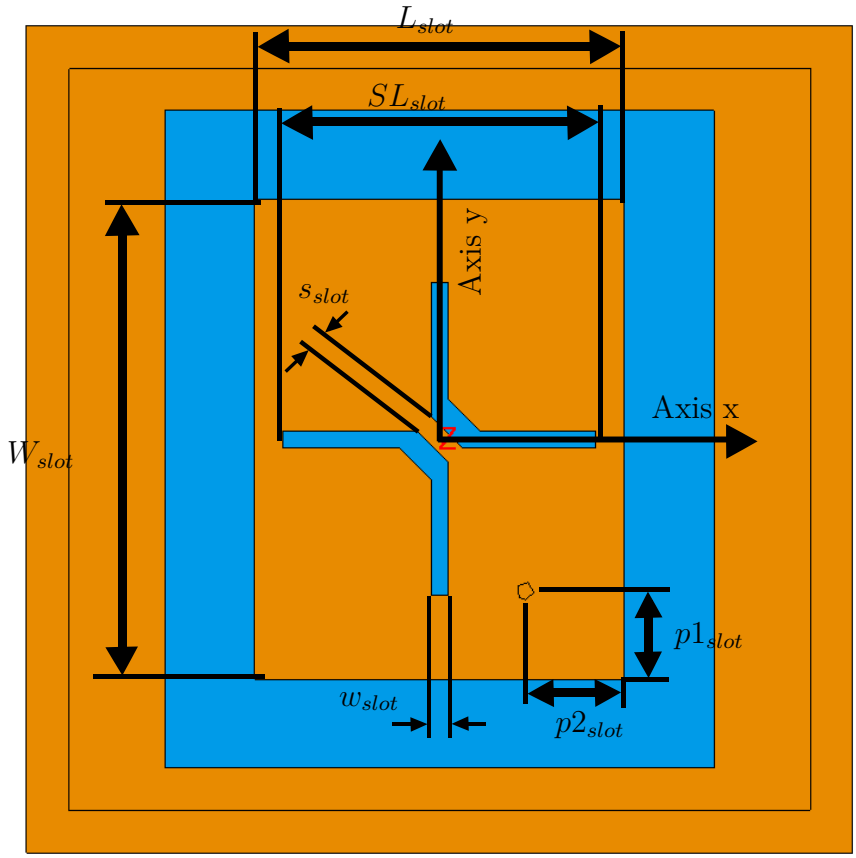

Figure 18 – The *Dual-Band Patch with Bents Slots* antenna geometry and its dimensions are shown. Blue represents Rogers AD250C dielectric and orange represents metal.

The introduction of the slots achieves dual-band operation, where both upper and lower frequency bands are lower in frequency than the centre frequency of the same sized patch used in single-band operation mode. This technique results in significant miniaturization with area reduction by up to 32% reported (Wang; Yang, 1998).

May be put on the x axis for TM_{01} excitation only, or on the y axis for TM_{10} excitation only and point on diagonal for dual-frequency operation. The two fundamental resonant frequencies occur at the TM_{01} (lower frequency) and the TM_{10} mode (upper frequency). The frequency ratio between the upper and lower frequencies is mainly controlled by the length and width (aspect ratio) of the patch (Dassault Systemes, 2019).

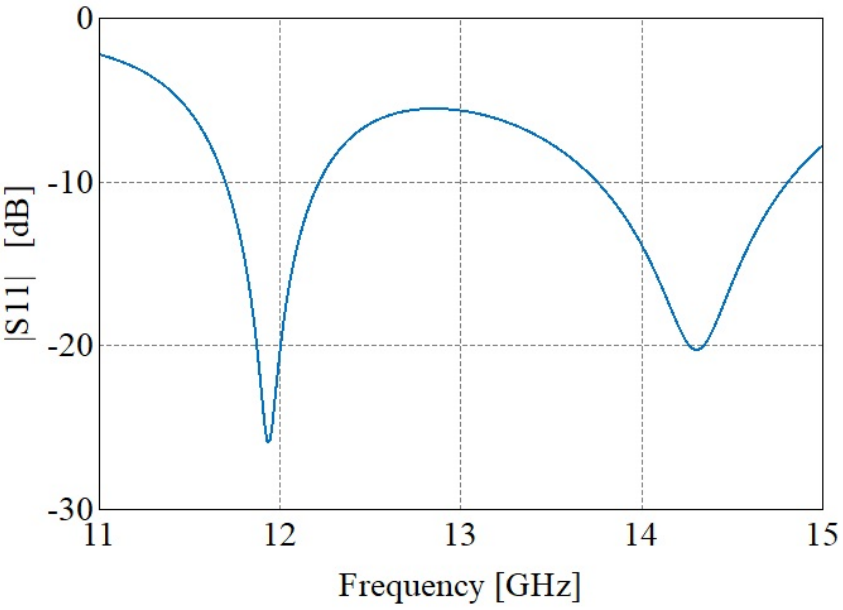

Figure 19 – Reflection coefficient (S_{11}) of antenna, is better than -10 dB both in reception and transmission for the same radiant element (figure 18).

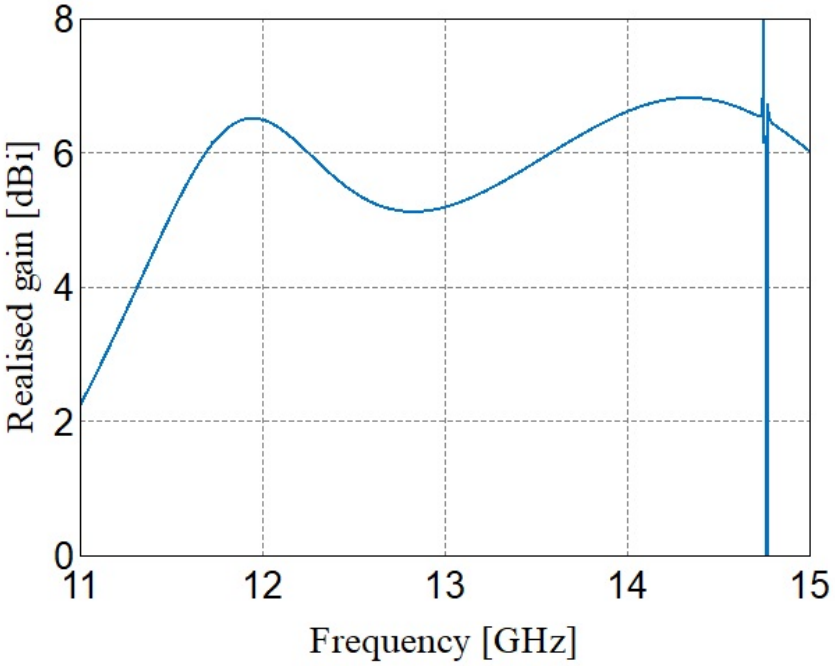

Figure 20 – Realised gain of radiant element *Dual-Band Patch with Bents Slots* shown in figure 18.

- To increase the lower resonant frequency, decrease the parameter L_{slot}, shown in Figure 18.
- To increase the upper resonant frequency, decrease the parameter W_{slot}.
- The operating bands can be increased by decreasing the parameter s_{slot}.

- To increase bandwidth, increase the substrate height and/or decrease the substrate permittivity (this will also affect resonant frequency and the impedance).
- To increase the input impedance at the lower frequency, decrease the parameter $p2_{slot}$.
- To increase the input impedance at the upper frequency, decrease the parameter $p1_{slot}$.

The Table 2 brings the parameters of the antenna shown in Figure 18, which was designed in Altair Feko software. The curves in the Figure 19 and 20 show the reflection coefficient and the gain respectively. The reflection coefficient was well centered in the reception band, at 11.95ĠHz, and in the transmission band at 14.25 Ghz. The gain presented a typical behavior of a microstrip antenna, around 6 dBi.

3.2.3 Truncated Rectangular Patch Feed on Center

The differential of this antenna is suitability for phased array antennas with circular polarization. All antennas presented in this dissertation have a feed point displaced from the center, if sequential rotations are desired, this introduces an extra difficulty in designing the phase shifters that lie between the antenna and the beamforming circuits. This antenna however has a centralized feed point that facilitates the design of the phase shifters. Keeping the advantages of simple and inexpensive to manufacture using consolidated printed-circuit technology, only one substrate layer, conformal possibility, reduced area, circular polarization already in the radiating element and improved when applied sequential rotation techniques.

The cut at the corner of the antenna generates a second mode, orthogonal to the first one with a 90° time phase difference. The antenna operates with four slits, two being parallel (TM_{01}) and the other two geometrically orthogonal (TM_{10}).

Table 3 – Design parameters of *Truncated Rectangular Patch Feed on Center*

W_s	3.18	C_s	1.22	F_s	1.71	R_s	0.72	L_s	2.65
W_d	3.97	C_d	1.34	F_d	2.22	R_d	0.92	L_d	3.28
ϵ_r	3.66	-	-	-	-	-	-	-	-

Note: parameters are given in [mm]. Laminate Rogers RO4350B of thickness 1.524 mm.

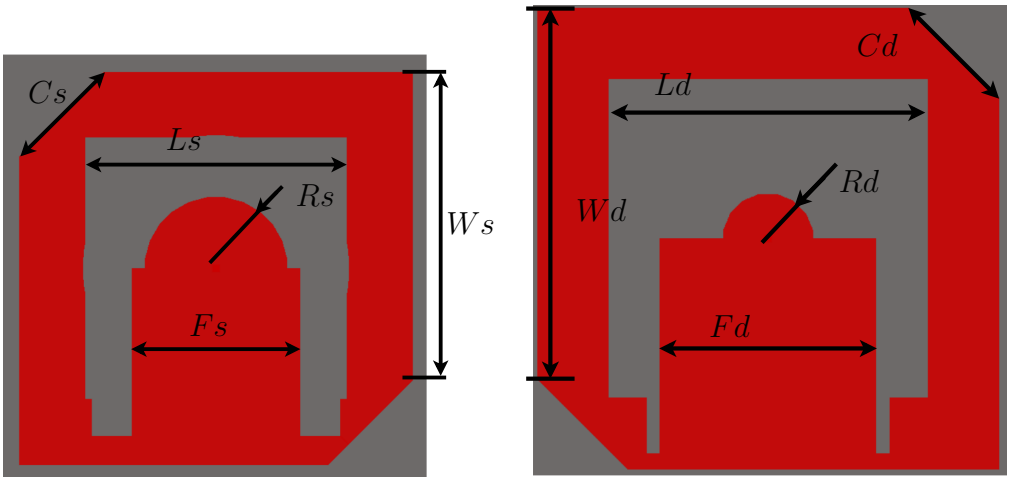

Figure 21 – Design parameters of antenna *Truncated Rectangular Patch Feed on Center*.

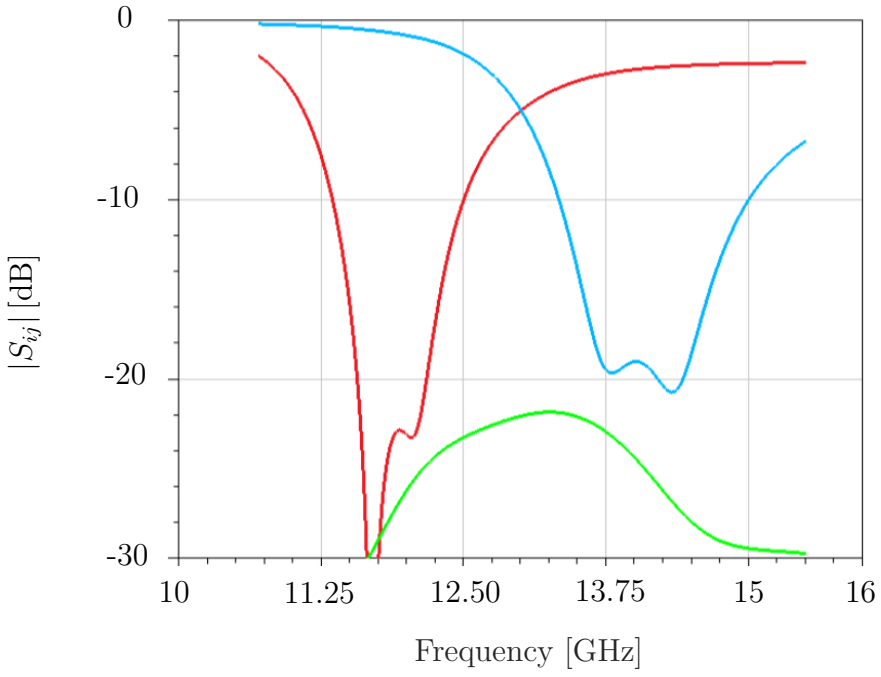

Figure 22 – In red the reflection coefficient of the receiving antenna (figure 21 b), in blue the reflection coefficient of the transmitting antenna (figure 21 a) and in green the coupling between receiving and transmitting antennas.

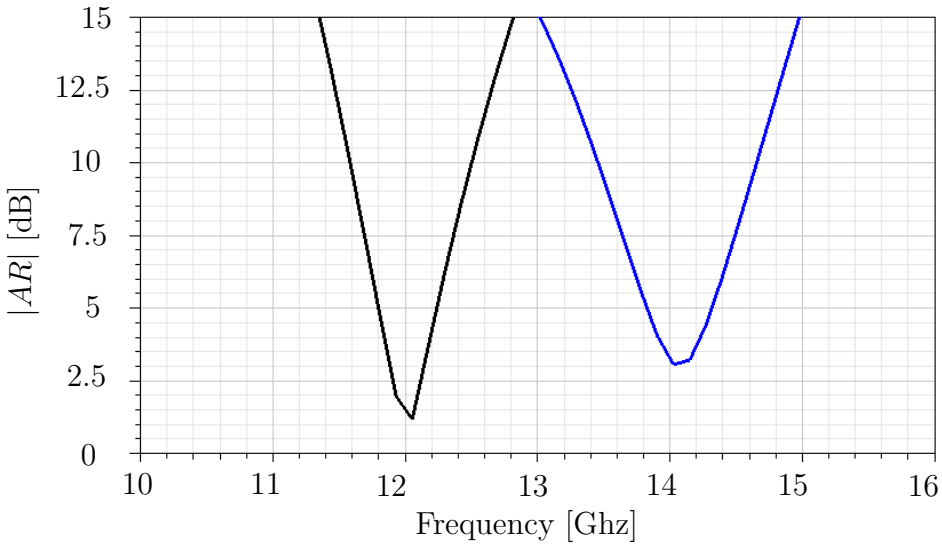

Figure 23 – In black the reflection coefficient of the receiving antenna (Figure 21 b) and in blue the reflection coefficient of the transmitting antenna (Figure 21 a).

- The centre frequency may be increased by decreasing the patch, mapped to the parameter W_s and W_d.
- The port resistance may be increased by reducing the feed inset.
- The patch width should be kept equal to the patch length and width to maintain good circular polarisation. Increasing the substrate height will result in an increased pin inductance, leading to a reduced bandwidth. Changing the polarisation variable between -1 (LHC) and 1 (RHC) changes the position of the truncations (C_d and C_s) on the patch element.

The *Truncated Rectangular Patch Feed on Center* antenna was designed in Ansys HFSS software, Table 3 has its parameters, which are mapped in Figure 21.

The reflection coefficient shown in Figure 22 was better than -18 dB for the transmit antenna, and better than -22 dB for the receive antenna. The axial ratio was better than -4.5 dB over the entire reception range as shown in Graph 23.

3.2.4 Capacitive Coupling Ratangular Patch

With similar operational characteristics to the *Truncated Rectangular Patch Feed on Center* antenna, the *Capacitive Coupling Ratangular Patch* antenna shown here has higher axial and impadance bandwidth. Microstrip antennas have high quality factor which implies narrow bandwidth (Balanis, 2016a). Regarding the previous antenna, a capacitive effect (metal-dielectric-metal) was added by the metalic circle delimited by Rc_1 dimenssion and the metal delimited by Rc_2 dimension, associated with the inductive effect of the metallic via (MVTI) feeder, the bandwidth was increased. It also contributed to the increase in bandwidth, the freedom associated with the Sc dimension.

Table 4 – Design Parameters of *Capacitive Coupling Ratangular Patch*.

W_c	5.67	C_c	1.95	R_{c1}	0.59	R_{c2}	0.69	S_c	0.89
ϵ_r	3.66	S_q	0.67	W_q	4.61	-	1.87	R_{q1}	0.49
R_{q2}	0.59	-	-	-	-	-	-	-	-

Note: parameters are given in [mm]. Laminate Rogers RO4350B of thickness 1.524 mm.

For safety we work with a minimum spacing between tracks of 100 μm. In fact, the capability specified by the manufacturer is 50 μm. Rectangular microstrip antenna most often has inductive behavior, reducing R_{c2} and R_{q2} increases the capacitive behavior of the antenna and tends to increase the impedance and axial bandwidth.

The Table 4 brings the parameters of the antenna shown in Figure 24, which was designed in Ansys HFSS software. The curves in the Figure 25 and 26 show the reflection

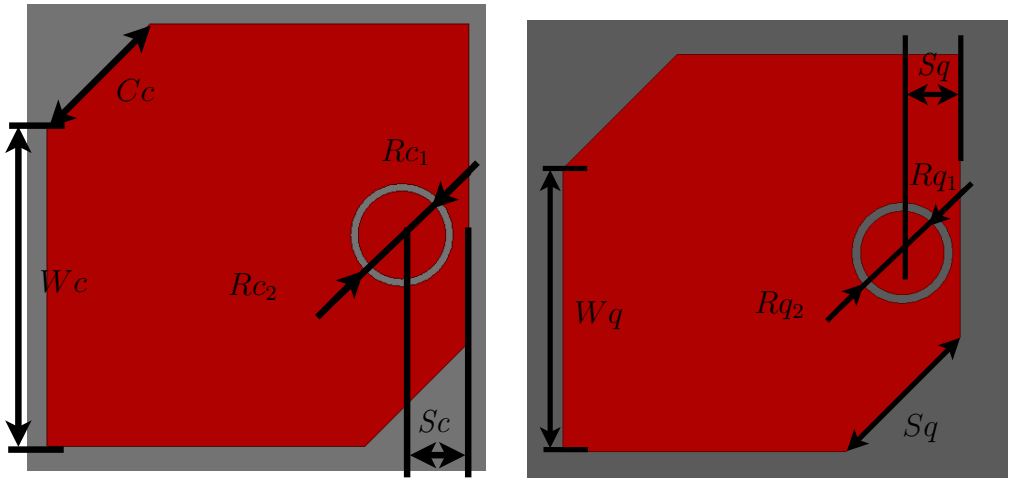

Figure 24 – (a) Reception *Capacitive Coupling Ratangular Patch antenna*. (b) Transmission *Capacitive Coupling Ratangular Patch antenna*

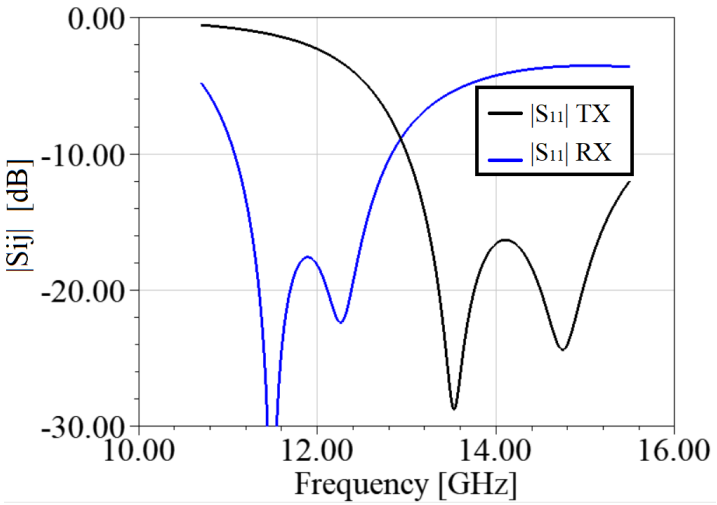

Figure 25 – In blue the reflection coefficient of the receiving antenna (figure 24 a) and in black the reflection coefficient of the transmitting antenna (figure 24 b).

coefficient and the axial ratio respectively. The reflection coefficient was better than -16 dB from 11.7 to 12.2 GHz and from 14 to 14.5 GHz. The axial ratio was better than 3.5 dB across the range.

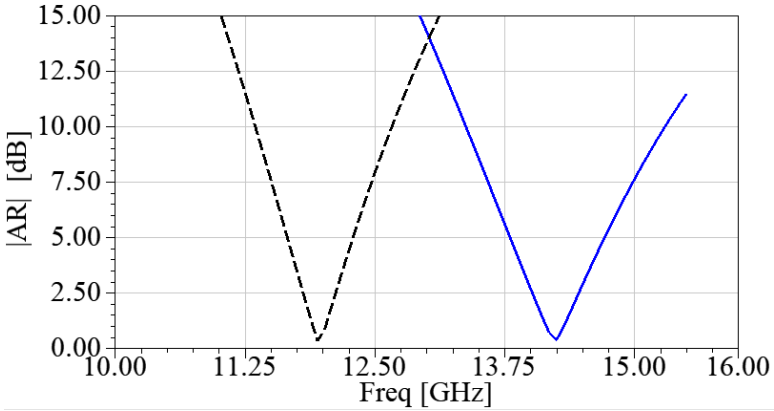

Figure 26 – In black the axial ratio of the receiving antenna (figure 24 a) and in blue the axial ratio of the transmitting antenna (figure 24 b).

3.3 Conclusion

This work brings four antennas design for phased arrays. The *Circular Microstrip Broadband*, *Dual-Band Patch with Bents Slots*, in them, a single element works for both transmission and reception, therefore significantly reducing the occupied area, In the first one, it is possible to add a second communication channel at the same time and frequency simply plugging into the second port of the antenna.

The *Truncated Rectangular Patch Feed on Center* and *Capacitive Coupling Ratangular Patch*, work in Ku sub bands, with one radiating element for transmission and the other for reception. Using these models increases the isolation between the transmission and reception chain since an antenna can be seen as a filter, however these models add the cost of two beamforming circuits, one dedicated for transmission and other for reception. Design of two 500 MHz sub bands is easier than designing circuits that cover the entire Ku band. In the present work, meeting the requirements of the sponsoring company in terms of bandwidth and polarization, the *Circular Microstrip Broadband* was chosen to be manufactured.

4 Beamformer

In fully digital beamforming an AD/DA converter is required for each antenna cell in the array, a single converter for applications that exceed tens of giga samples per second costs over thousands of dollars. The present solution processes all antenna signals, using only etching passive boards and even eliminates synchronization problems because the signal is delivered to the next stages in a single channel.

4.1 Linear Phased Array Antenna Theory

In practical situations where it is desired to establish a satellite communication link or radar applications, the transmitted and received power are easily accessible metrics, the main information is the far-field irradiation pattern, which is the response of an antenna as a function of direction. For uniformly-spaced arrays, the design methods are identical to the methods for designing finite impulse response (FIR) digital filters in digital signal processing (DSP), such as window-based and frequency-sampling designs, the Annex D shows the duality between time-domain and space-domain. In fact, historically, these methods were first developed in antenna theory and only later were adopted and further developed in DSPs (ORFANIDIS, 2016). The reciprocity theorem allows us to look at the radiating system in reception or transmission. In (ORFANIDIS, 2016) it is shown that we can find the radiated field by performing the Fourier transform in the spatial domain of the current density. Assuming a current density $\boldsymbol{J(r)}$, where $\boldsymbol{r}(x,y,z) \in \mathbb{R}^3$ is the position of the radiating element in a rectangular coordinate system. The radiation vector can be written as,

$$\boldsymbol{F}_{rad}(\boldsymbol{k}) = \int_{\mathbb{R}^3} e^{j\,\boldsymbol{k}\cdot\boldsymbol{r}}\,\boldsymbol{J}(\boldsymbol{r})\,\mathrm{d}\,v(\boldsymbol{r}). \tag{4.1}$$

Where $\mathrm{d}v(\mathbf{r})$ is the infinitesimal volumetric element. Assuming another radiating element positioned at the position $\boldsymbol{d}_n(x, y_n, z)$ shifted in y axis, the radiation vector stay,

$$\boldsymbol{F}_{dn}(\boldsymbol{k}) = \int_{\mathbb{R}^3} e^{j\,\boldsymbol{k}\cdot\boldsymbol{r}}\,\boldsymbol{J}_{dn}(\boldsymbol{r})\,\mathrm{d}\,v(\boldsymbol{r}), \tag{4.2}$$

$$\boldsymbol{r}_n = \boldsymbol{r} - \boldsymbol{d}_n, \tag{4.3}$$

$$\boldsymbol{J}(\boldsymbol{r}_n) = \boldsymbol{J}(\boldsymbol{r} - \boldsymbol{d}_n) = \boldsymbol{J}_{dn}(\boldsymbol{r}). \tag{4.4}$$

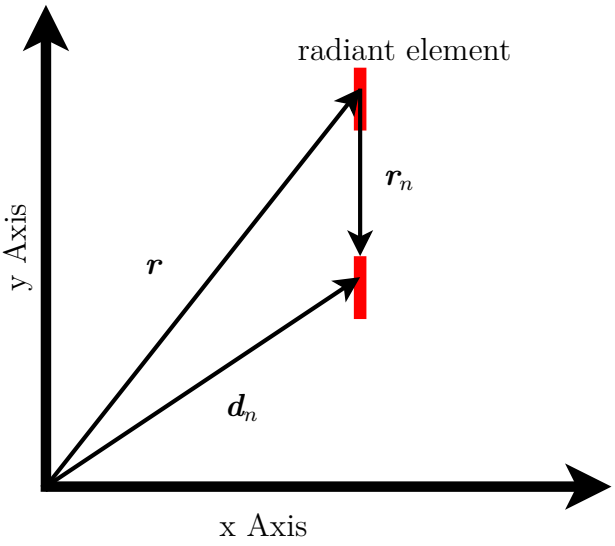

Figure 27 – Translational Phase Shift.

$\boldsymbol{d}_n$ is invariant with $\boldsymbol{r}$, so $\mathrm{d}v(\mathbf{r}_n) = \mathrm{d}v(\mathbf{r})$, replacing in the equation 4.2,

$$\boldsymbol{F}_{dn}(\boldsymbol{k}) = \int_{\mathbb{R}^3} e^{j\,\boldsymbol{k}\cdot(\boldsymbol{r}_n+\boldsymbol{d}_n)}\,\boldsymbol{J}(\boldsymbol{r}_n)\,\mathrm{d}v(\boldsymbol{r}) = \int_{\mathbb{R}^3} e^{j\,\boldsymbol{k}\cdot\,\boldsymbol{d}_n}\,e^{j\,\boldsymbol{k}\cdot\boldsymbol{r}_n}\,\boldsymbol{J}(\boldsymbol{r}_n)\,\mathrm{d}\,v(\boldsymbol{r}), \tag{4.5}$$

$$\boldsymbol{F}_{dn}(\boldsymbol{k}) = e^{j\,\boldsymbol{k}\cdot\boldsymbol{d}_n}\int_{\mathbb{R}^3} e^{j\,\boldsymbol{k}\cdot\boldsymbol{r}_n}\,\boldsymbol{J}(\boldsymbol{r}_n)\,\mathrm{d}\,v(\boldsymbol{r}_n), \tag{4.6}$$

$$\boldsymbol{F}_{dn}(\boldsymbol{k}) = e^{j\,\boldsymbol{k}\cdot\boldsymbol{d}_n}\,\boldsymbol{F}_{rad}(\boldsymbol{k}). \tag{4.7}$$

$e^{j\,\boldsymbol{k}\cdot\boldsymbol{d}_n}$ is called array factor $A(\boldsymbol{k})$, assuming a fixed observation point and constant frequency, $\boldsymbol{F}_{rad}$ is related to the electric field $\boldsymbol{E}$ for a constant, here called C_{path}.

$$\boldsymbol{E} = C_{path}\boldsymbol{F}_{rad} \tag{4.8}$$

$$\boldsymbol{E}_{total}(\Phi) = A\,\boldsymbol{E}_{elementary} \tag{4.9}$$

Suppose 4 elements equal spacing by a distance d with uniform excitation equal to 1, and using the superposition theorem.

Array factor takes the form,

$$A(\boldsymbol{k}) = e^{j\,\boldsymbol{k}\cdot\,\boldsymbol{d}_0} + e^{j\,\boldsymbol{k}\cdot\,\boldsymbol{d}_1} + e^{j\,\boldsymbol{k}\cdot\,\boldsymbol{d}_2} + e^{j\,\boldsymbol{k}\cdot\,\boldsymbol{d}_3}. \tag{4.10}$$

Where $\boldsymbol{d}_0 = 0\,\hat{\mathbf{a}}_y$, $\boldsymbol{d}_1 = d\,\hat{\mathbf{a}}_y$, $\boldsymbol{d}_2 = 2d\,\hat{\mathbf{a}}_y$, $\boldsymbol{d}_3 = 3d\,\hat{\mathbf{a}}_y$, and $\boldsymbol{k} = k_x\hat{\mathbf{a}}_x + k_y\hat{\mathbf{a}}_y + k_z\hat{\mathbf{a}}_z$ gives the wave propagation direction.

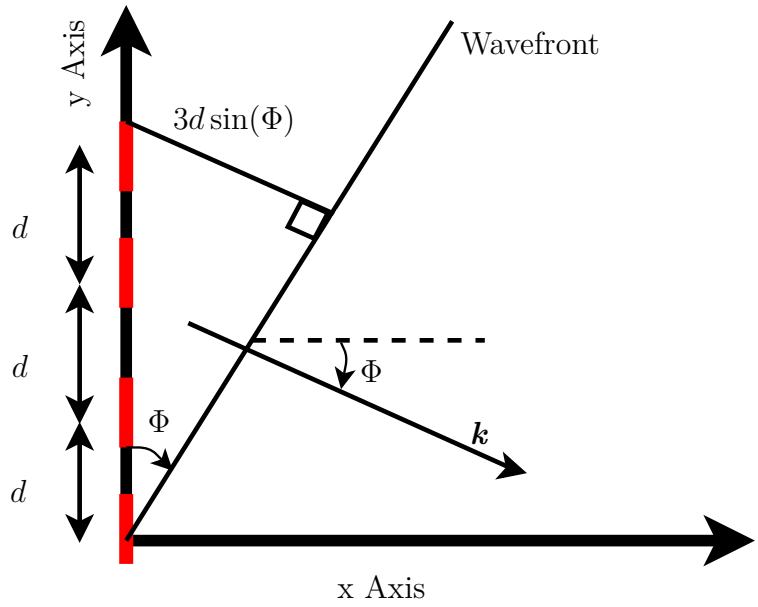

Figure 28 – Four radiant elements, in red color, of equal amplitude and spacing.

The inner product of vectors can be written as,

$$\boldsymbol{k} \cdot \boldsymbol{d}_n = |\boldsymbol{k}|\,|\boldsymbol{d}_n|\,\sin(\Phi). \tag{4.11}$$

Substituting in the equation 4.10,

$$A(\Phi) = e^0 + e^{j\,|\boldsymbol{k}|\,d\,\sin(\Phi)} + e^{j\,|\boldsymbol{k}|\,2d\,\sin(\Phi)} + e^{j\,|\boldsymbol{k}|\,3d\,\sin(\Phi)}. \tag{4.12}$$

The equation 4.12 is a power series of ratio $e^{j\,|\boldsymbol{k}|\,d\,\sin(\Phi)}$ and can be written as follows,

$$A(\Phi) = \frac{1 - e^{j\,|\boldsymbol{k}|\,4d\,\sin(\Phi)}}{1 - e^{j\,|\boldsymbol{k}|\,d\,\sin(\Phi)}}. \tag{4.13}$$

Replacing $|\boldsymbol{k}|$ by $\frac{2\pi}{\lambda}$, where λ is the wave-lengt,

$$A(\Phi) = \frac{1 - e^{j\,\frac{2\pi}{\lambda}\,4d\,\sin(\Phi)}}{1 - e^{j\,\frac{2\pi}{\lambda}\,d\,\sin(\Phi)}}, \tag{4.14}$$

$$A(\Phi) = \frac{\sin(\frac{4\pi\,d}{\lambda}\,\sin(\Phi))}{4\,\sin(\frac{\pi\,d}{\lambda}\,\sin(\Phi))}. \tag{4.15}$$

4.2 Single Rotman Lens design

The Rotman Lens is a broadband true time delay beamformer. There are three main regions of operation of the lens: the focal arc, traces the outline of the beam ports, that set the pointing direction; the inner lens contour, that traces the contour of the array ports, which are connected to the delay lines; and finally, the external contour, which is where the antennas are located, located between the delay lines and the antennas. The main design parameters of the Rotman lens are shown in Figure 29, where α is the focal angle, Φ the scanning angle, G the on-axis focal length, F the off-axis focal length, N the half the length of the antenna array, W_n the delay line, W_0 central delay line, F_1, F_2 and F_0 is the focal points, and R the circular lens radius.

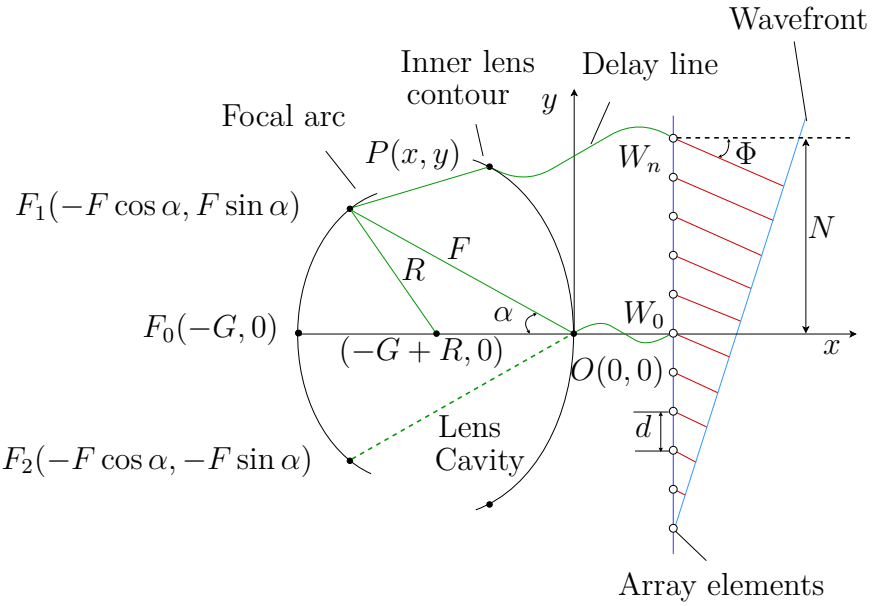

Figure 29 – Geometry and design parameters of a Rotman lens. The lens consists of a focal arc where the beam ports are located. The internal contour arc that is connected to the delay lines and later to the antennas. The essential parameters for the design of the Rotman lens are exhibited above. Among them, there are parameters related to the focal points, its angles and distances, and others related to the antenna array.

To design the lens, a first approximation is done based on geometric optics. It is also assumed that the beam ports are connected with all the output ports. The propagation delay of the wave traveling inside the lens is proportional to the physical distance between the input and output ports. This model allows the optimization of the cavity size and line length, as well as the possibility to reduce aberration errors. Optical equations of equal distances are obtained in (SUÁREZ, 2015; Attaran; Rashidzadeh; Kouki, 2016; Rotman; Turner, 1963) and are deduced from three rays starting from perfect focal points that produce flat waves with angles of Φ, $0\,^\circ$ and $-\Phi$ and is expressed as:

$$\begin{cases} F_0 P + W = G + W_0 \\ F_1 P + W + N \sin\Phi = F + W_0 \\ F_2 P + W - N \sin\Phi = F + W_0 \end{cases} \tag{4.16}$$

The second step is done in a full-wave simulation environment, where the metrics optimization such as losses, internal reflections, coupling effects, array factor, is done.

Several sensibility analysis has been performed on the main parameters of the Rotman lens. Each parameter influences an aspect of the lens geometry and, subsequently, the array factor (SUÁREZ, 2015; Attaran; Rashidzadeh; Kouki, 2016). The parameter α is the maximum beam angle, Φ is the angle that defines the maximum scanning angle. The parameter g determines the normalized distance from the central focal point F_0 to the central point of the inner contour of the lens (0.0) and is obtained by $g = G/F$, where G is the maximum body length in the x axis. The parameter g influences the curvature of the focal arc, the lens aberration, and the delay lines. The further away from the value $g = 1$, the greater the difference in the length of these lines. It has been observed that by decreasing G it is possible to improve the phase error and the losses within the lens, so it is important to find a compromise between G and F. Parameter N is related to the size of the antenna array to be connected to the lens output, and is influenced by the spacing between the antennas. Larger values of N increase the area and the computational charge in simulation full wave (FEM, MoM, FDTD). Dummy ports (DM) decrease reflections within the lens, one should generally seek for the geometry in which the distance between DM sets is greater than the distance between beam ports and array ports. Optimizing the lengths of the delay lines decrease side lobes.

To perform the impedance matching between the $50\,\Omega$ outer lines and the lens core, tapers are used. The tapers have a gradual opening, where the narrow end connects the $50\,\Omega$ stripline port, while the wider side connects to the lens core forming a design similar to a horn antenna, this reduces the impedance mismatch. Besides, there is a uniform distribution of energy inside the lens, allowing broadband operation. According to (Musa; Smith, 1989; Musa; Smith, 1986) the cone opening must be between $\lambda/2$ and λ, making the transition smoother and providing better performance.

It has been observed that lenses with an odd number of beam ports provide better performance than the ones with even quantities when evaluating phase errors over the whole Ku-band. This is due to the fact that with an odd number of ports, these lie on the three focal points: the central F_0 and at the F_1 and F_2 points. This reduces the aberrations in the lens, thus decreasing the pointing error and lowering the reflection coefficient. Therefore, for this project, an odd number of beam ports is chosen. The lenses were simulated in the Ansys HFSS software. A fourth focal point can be obtained if the array can be arbitrarily curved.

Both lenses were primarily designed at the central frequency $f_0 = 13.1\,\text{GHz}$, and adjusted to cover the 2.8 GHz bandwidth. Their focal angle is $\alpha = 40°$, with a scanning angle $\Phi = \pm 30°$ and $g = 1.05$. The ports positions match the antenna $\lambda_0/2 = 11.45\,\text{mm}$ element spacing. The respective focal distance for θ and ϕ-planes lenses are $G_\theta = 21\,\text{mm}$ and $G_\phi = 22\,\text{mm}$.

Two stacks of stripline Rotman lens are designed. One stack has lenses with 5 beam ports and 4 array ports scanning θ plane and the other has lenses with 3 beam ports and 4 array ports scanning ϕ plane. Grounded MVTIs are strategically placed between the ports to prevent coupling and fluctuation. Figure 30 shows the lenses structure. The choice of having 3×5 beams feeding a 4×4 antenna array is only based on showing that the number of beams is independent of the array size, unlike usual Butler matrices structures. As shown in Figure 30, both lenses have 4 dummy ports to reduce unwanted internal reflection. The capacitive transitions added a small phase error. Regardless of whether the lens is the first or the last in the stack, the amount of capacitive transitions to cover the entire electrical path is the same, this added a measured average error of 3.8°. Figure 35 present the manufactured resulting stacks of lenses. Figure 61 shows the lenses PCB stack up. With four lenses stacked, and equally spaced ports.

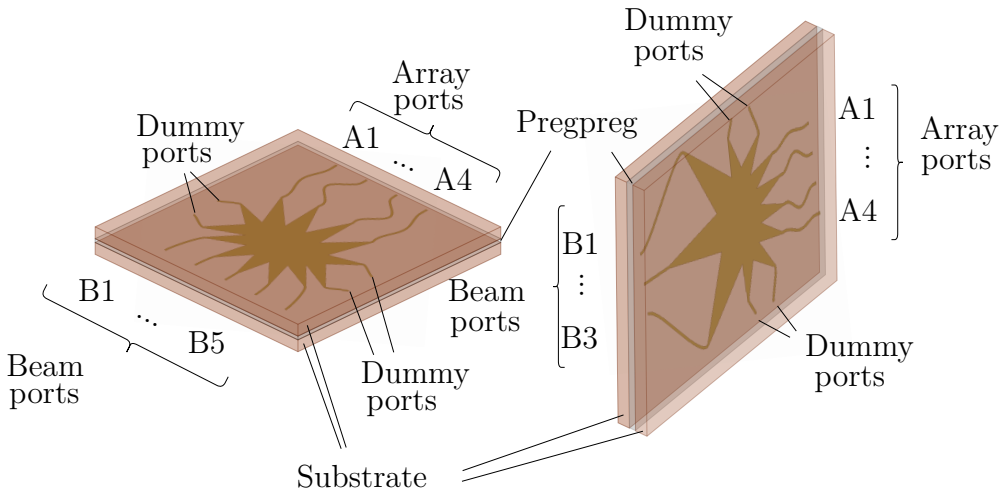

Figure 30 – θ- and ϕ-plane stripline Rotman lenses, both designed independently. The θ-plane lens has 5 beam ports and 4 array ports. The ϕ-plane lens has 3 beam ports and 4 array ports. Both lenses have 4 dummy ports.

4.3 Stacked Rotman Lens

This section presents the details of the interconnection scheme, routing setup, and stack-up features used to achieve beam-steering along space using the two Rotman lenses stacks and the antenna array while maintaining a low profile PCB based assembly.

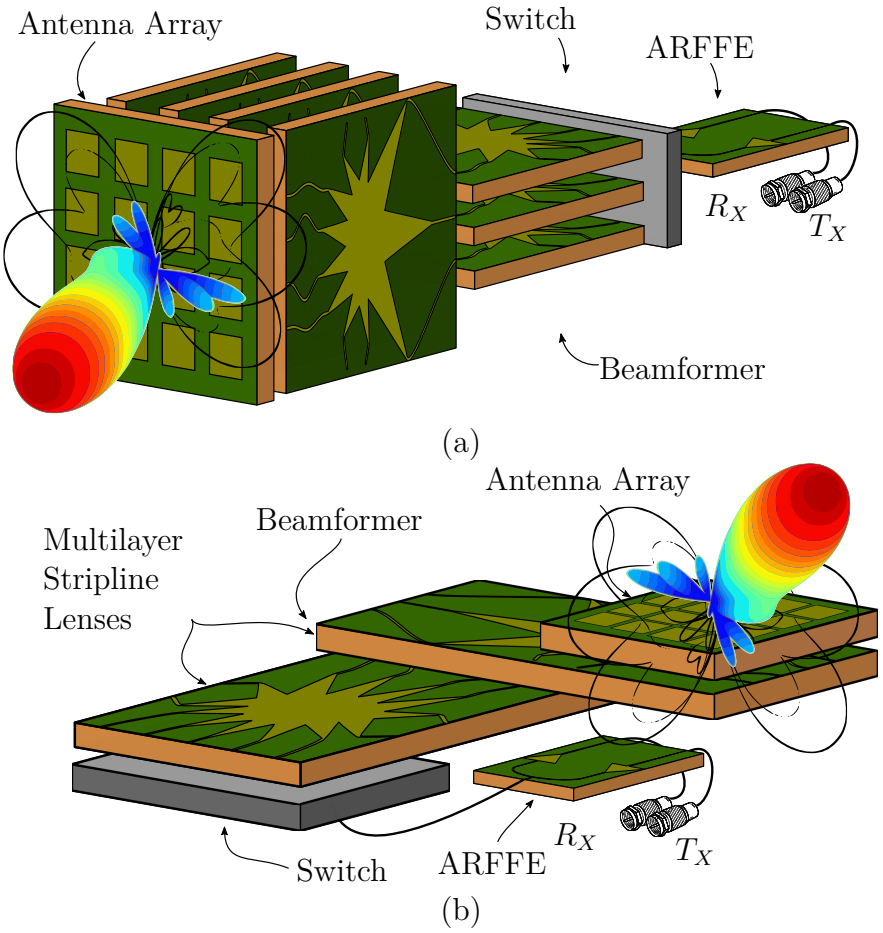

Figure 31 – The above figures compare two 3D views of (a) a classical non-planar implementation of the classical bulky Rotman lenses based system, and (b) the proposed planar implementation of the entire beam-forming system.

There are two orthogonal stages of lenses, each one applying the phase delay in one plane (θ and ϕ), as shown in Figure 32. The first stage is composed of three lenses with five beam ports by four array ports, and the second stage has four lenses with three beams ports by four array ports.

As depicted in Figure 32, the beam selection is made by an RF switch matrix, that directs the signal to the desired beam port. The beam steering is done by the body of lenses. The orthogonal connection is done when each output port of a θ-plane lens is connected to a different layer of ϕ-plane stack.

In addition to the phase difference caused by the lens body, each lens of the ϕ-plane (second stage) receives the signal with a different electrical length caused by different amount of layers crossed. However, this difference is compensated in the output path, the amount of layers to cross is reversed, this results in only the phase delay inserted by the lens body.

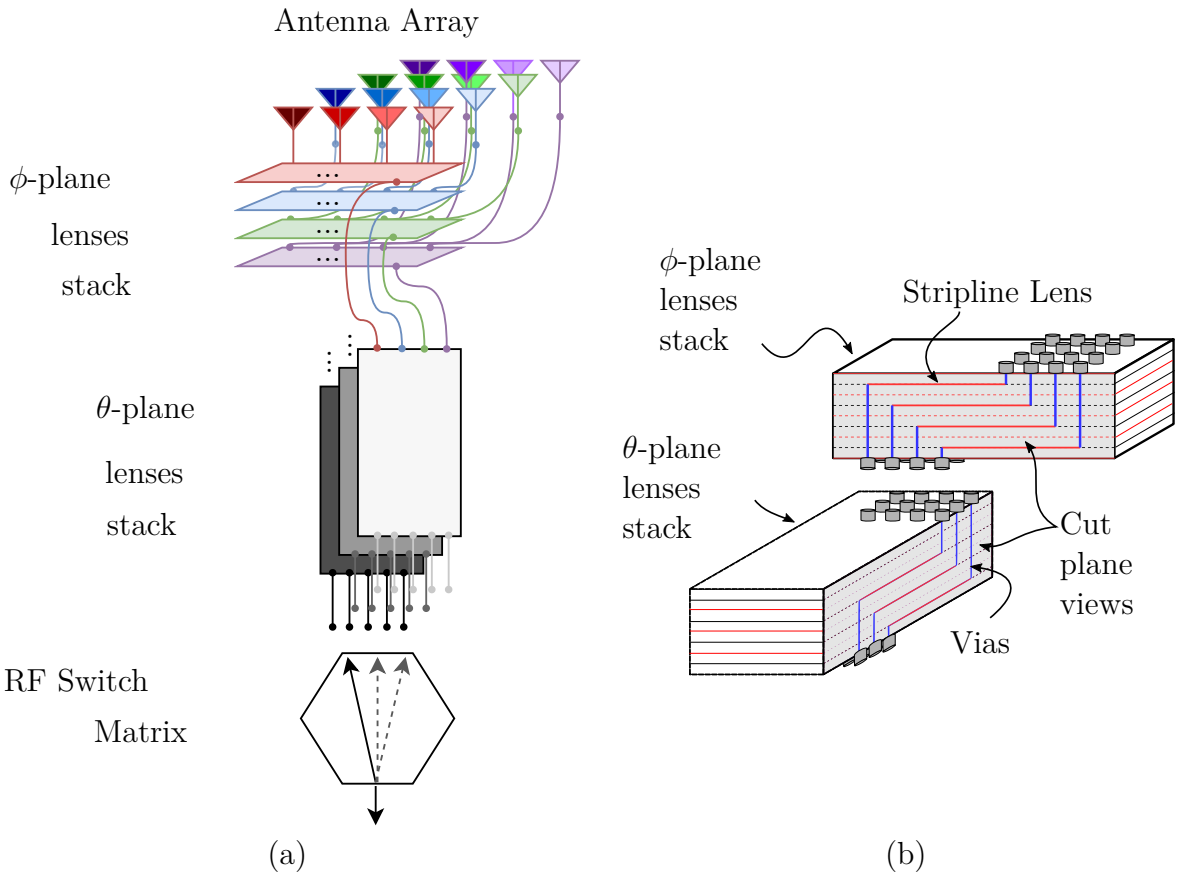

Figure 32 – System's assembly. (a) Orthogonal Rotman lenses block diagram with two stages of lenses connected. The first stage comprises three 5×4 lenses, and the second stage has four 3×4 lenses. Each stage scans on one plane in the space (ϕ and θ). The resultant beam direction is the linear combination of both planes pointing. (b) Representation of the beamformer interconnection showing how the lenses are arranged in the assembly.

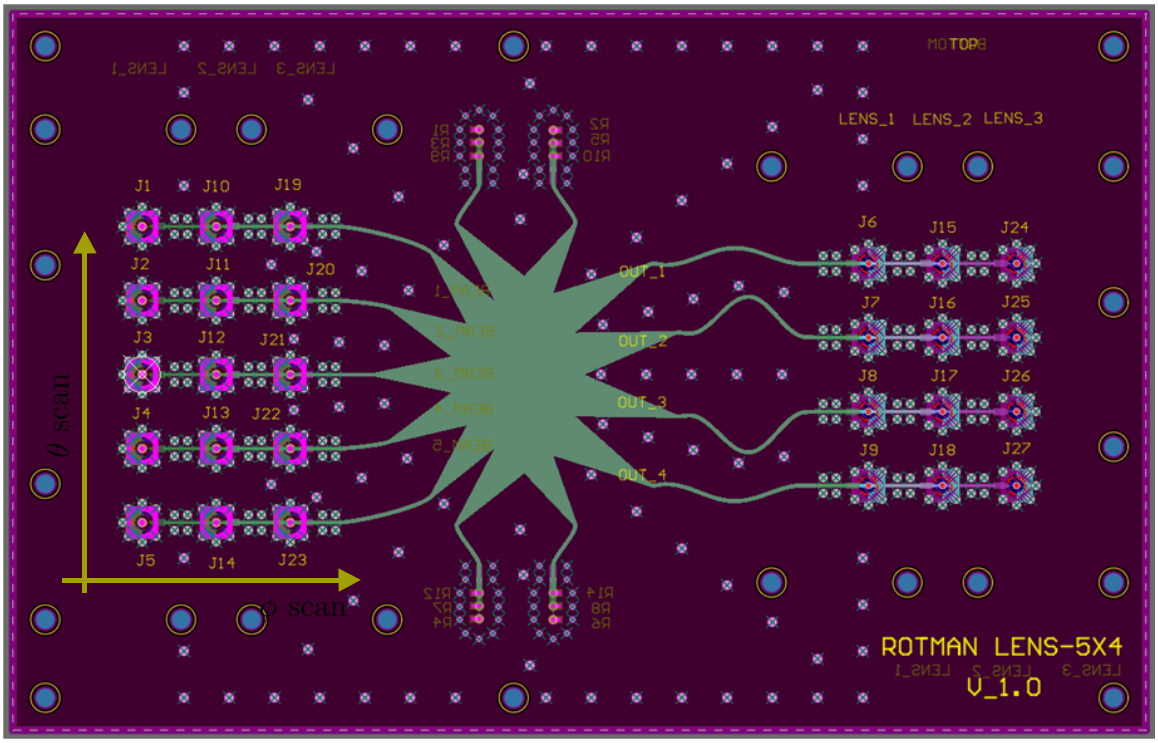

Figure 33 – Layout of θ-plane lenses stack, thirteen layers on Altium Designer Software.

Table 5 – Mapping correspondence table between Altium Software connectors in the layout and named radiation pattern measured.

Layout conector			Beam		
J1	J10	J19	Beam 1	Beam 6	Beam 11
J2	J11	J20	Beam 2	Beam 7	Beam 12
J3	J12	J21	Beam 3	Beam 8	Beam 13
J4	J13	J22	Beam 4	Beam 9	Beam 14
J5	J14	J23	Beam 5	Beam 10	Beam 15

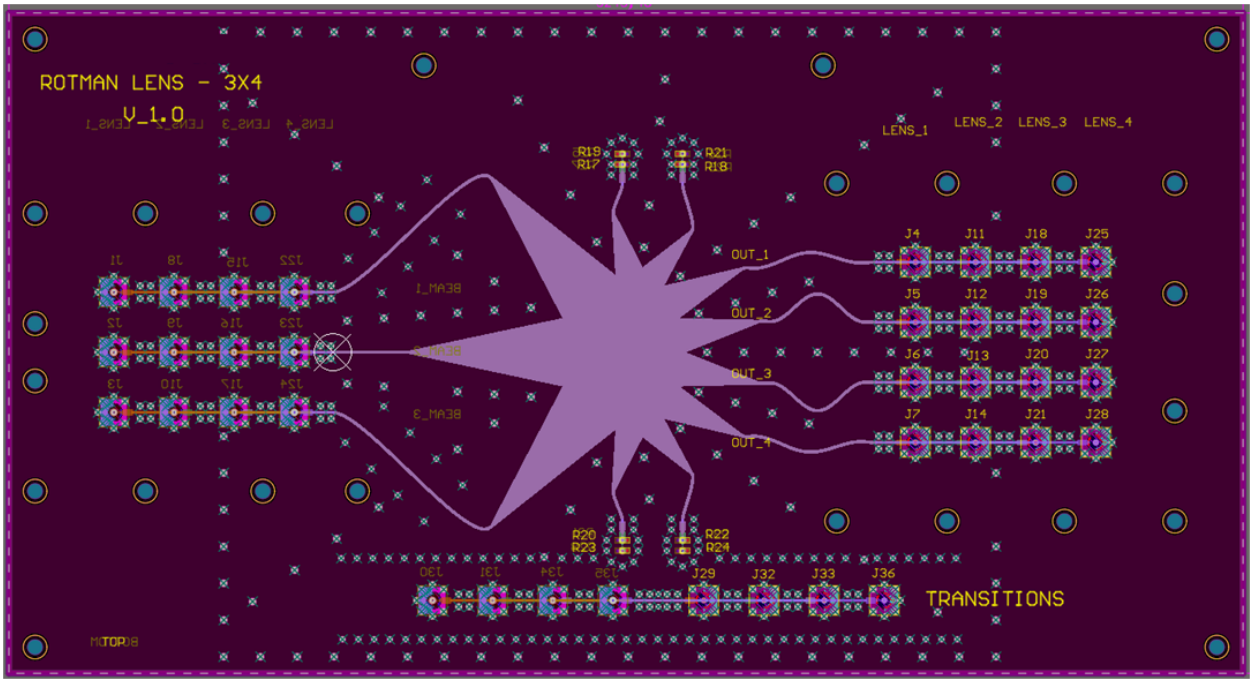

Figure 34 – Layout of ϕ-plane lenses stack, thirteen layers on Altium Designer Software.

The ϕ-plane lenses stack needs 13 layers and the θ-plane lenses stack needs 10 layers. To reduce the cost of the prototype 3 layers was added to the θ-plane lenses stack so that both boards could be manufactured in the same process and the same laminates. The layouts are shown in Figures 33 and 34, the mapping between the board connectors and the formed beams are shown in Table 5. The result of the manufacturing process is shown in figure 35.

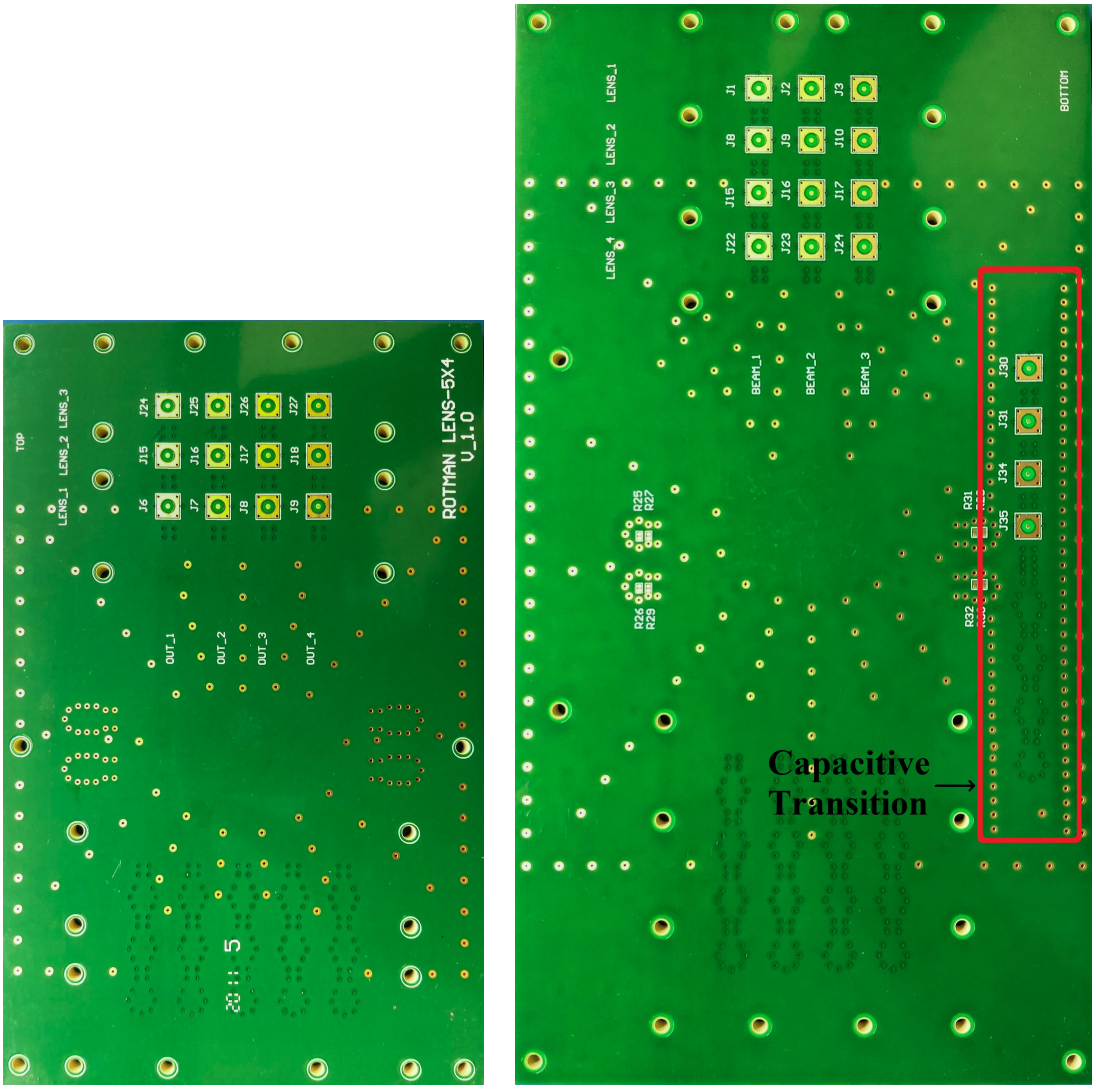

(a) (b)

Figure 35 – Photography of the (a) θ-plane lenses. 95.5 mm × 85.6 mm (b) ϕ-plane lenses PCBs. 75.2 mm × 108.7 mm. Because it is a stripline circuit, it can not be seen directly in the picture, but there can be noticed the GND MVTIs at the contour of the tapered lines, as well as the pads for resistor at the dummy ports, and the pads for SMA connectors.

The entire system possesses 15 beam ports, providing 15 different beams, and 16 array ports to be connected in a 4×4 antenna array.

The connections were designed for planar assembly, connecting the lenses and antenna PCB in parallel planes, as shown in Figures 31, 32 and 61. The PCBs were interconnected using SMP board-to-board transitions. These allowed for quick mounting and inter-boards misalignment tolerance and also allowing a complete characterization for each lens and antenna array element. A nylon structure was prepared to assemble the system with the proper board spacing and mechanical steadiness. Previous dual-plane beam scanning using Rotman lenses has been reported in (Babar Abbasi; Fusco; Matthaiou,

2019), but the connections turn the solution into a bulky and fragile system. Differently, the solution proposed in this manuscript allows a planar robust structure and this fact constitutes a novel contribution to the state of the art. Moreover, the whole structure can be manufactured in one single board, exchanging the inter-board connectors for built-in connections. In an industrial manufacture production, a BGA like soldering technique has to be carried out instead of these SMP connectors to joint each stack of the overall structure. Therefore, the beamformer can be manufactured using an industrial large scale manufacture process, drastically reducing its production cost.

4.4 Results

The measurements of S-parameters of the lens are performed with a 2-port vectorial network analyzer, so each path has been analyzed separately, with 50 Ω loads at the remaining ports. With the values the normalized array factors of both lenses are calculated and compared with their simulated values. Figures 37-46 compares the simulated and measured array factor of θ- plane, and the Figures 47-59, for ϕ -plane lenses.

4.4.1 θ-plane Lenses Measurement (5 input by 4 output ports)

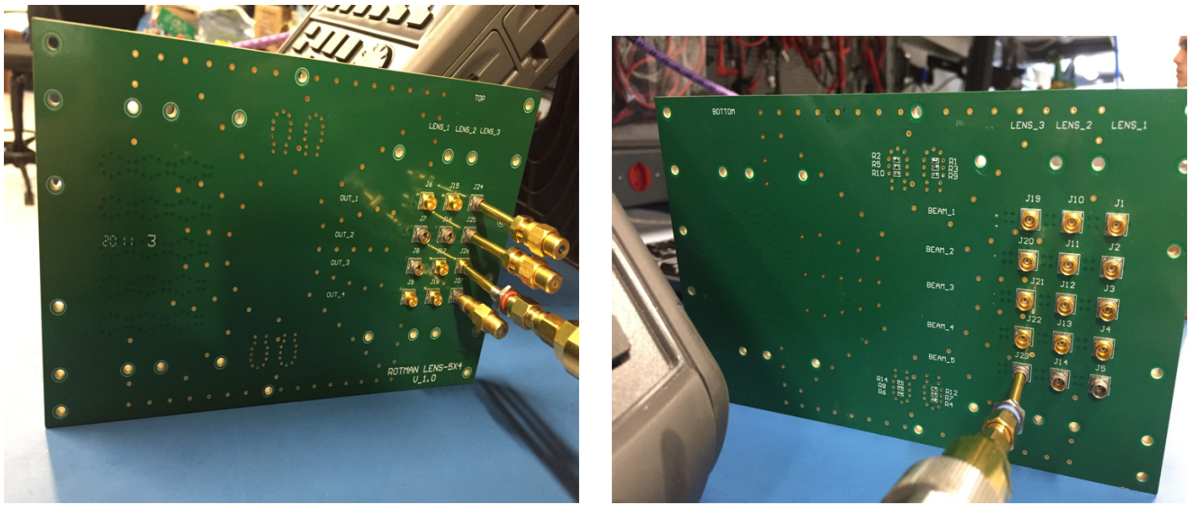

(a) (b)

Figure 36 – Measurement θ-plane lenses scattering parameters with Keysight N9917B FieldFox Handheld Microwave Analyzer, (a) top layer view, (b) Bottom layer.

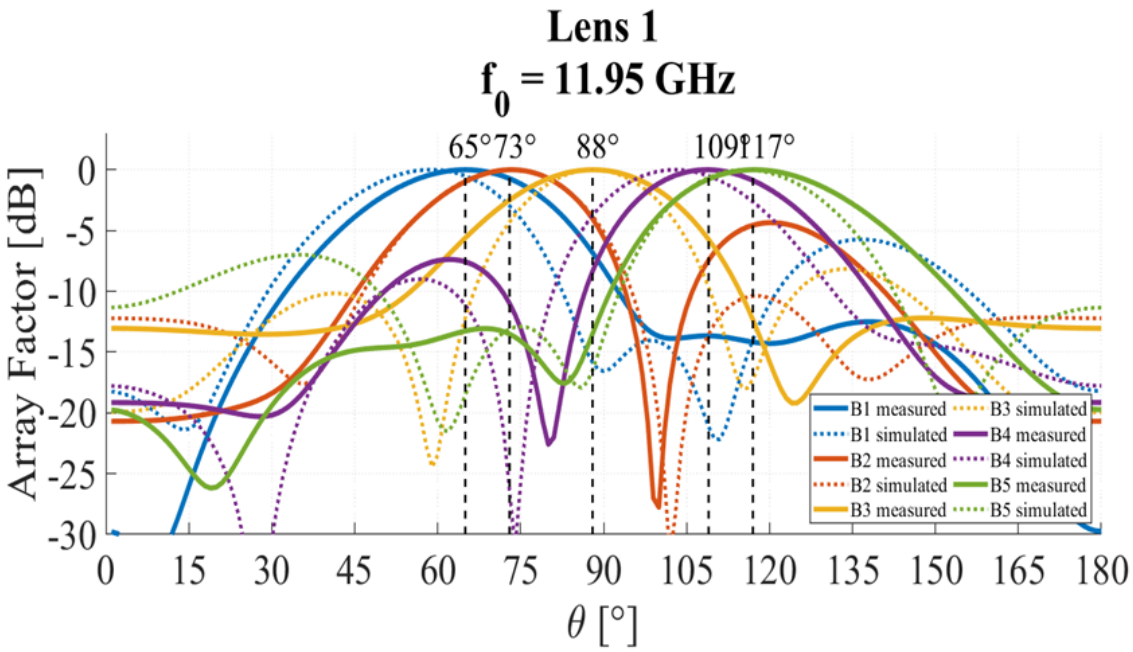

Figure 37 – Array factor calculated from measured S parameter. For the first lens at 11.95 GHz.

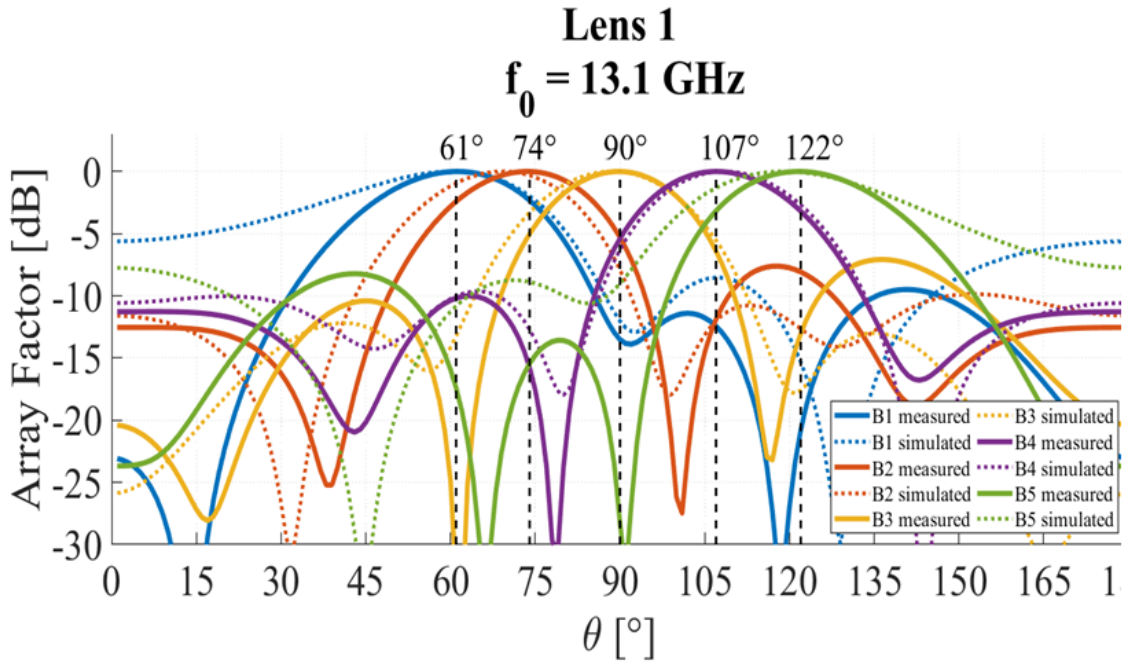

Figure 38 – Array factor calculated from measured S parameter. For the first lens at 13.10 GHz.

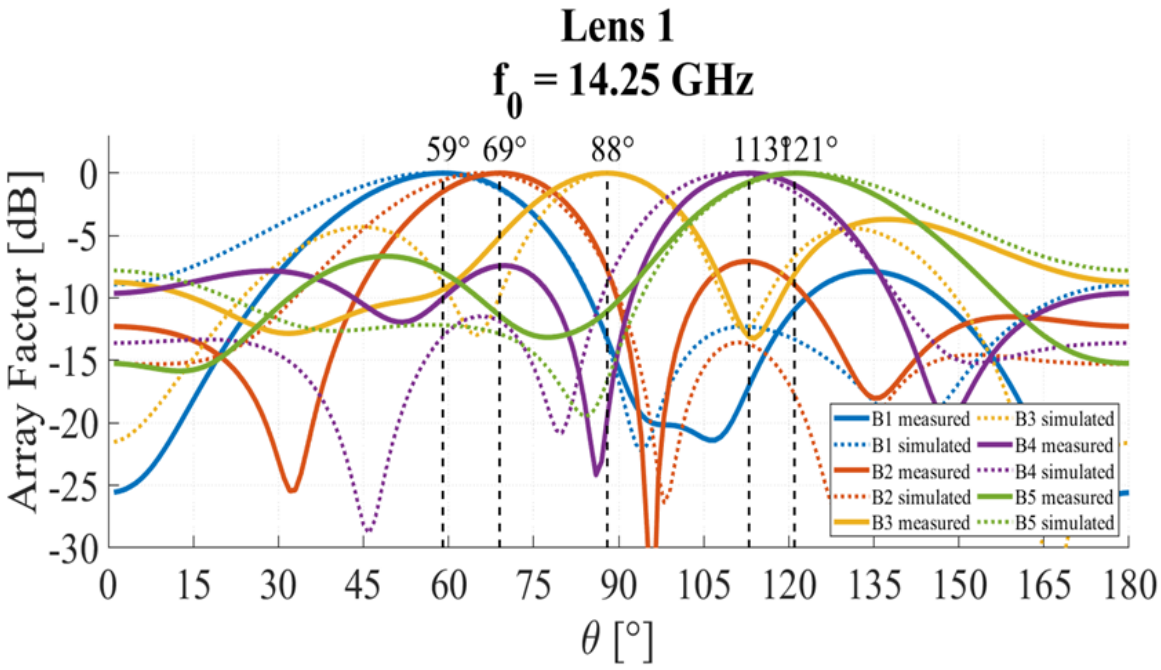

Figure 39 – Array factor calculated from measured S parameter. For the first lens at 14.25 GHz.

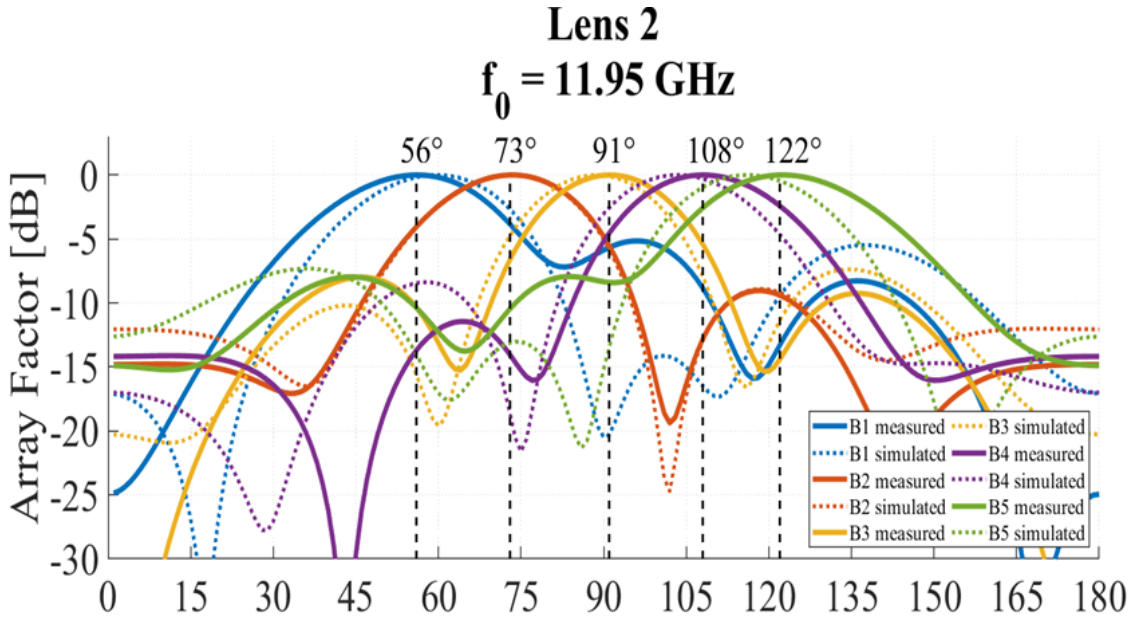

Figure 40 – Array factor calculated from measured S parameter. For the second lens at 11.95 GHz.

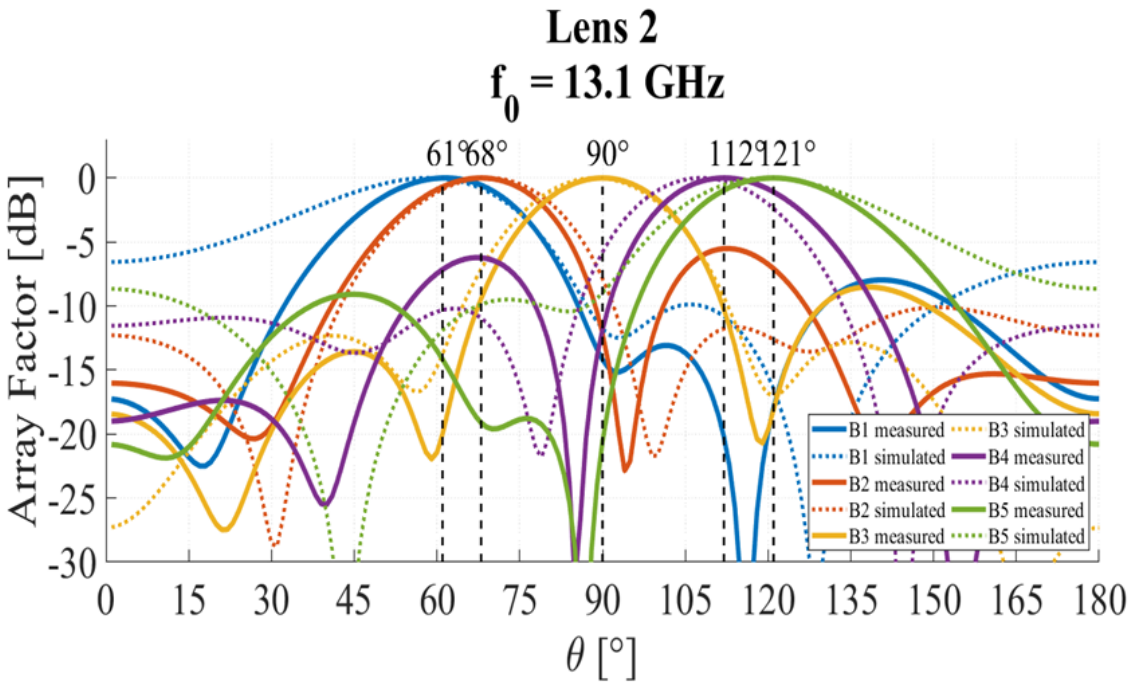

Figure 41 – Array factor calculated from measured S parameter. For the second lens at 13.10 GHz.

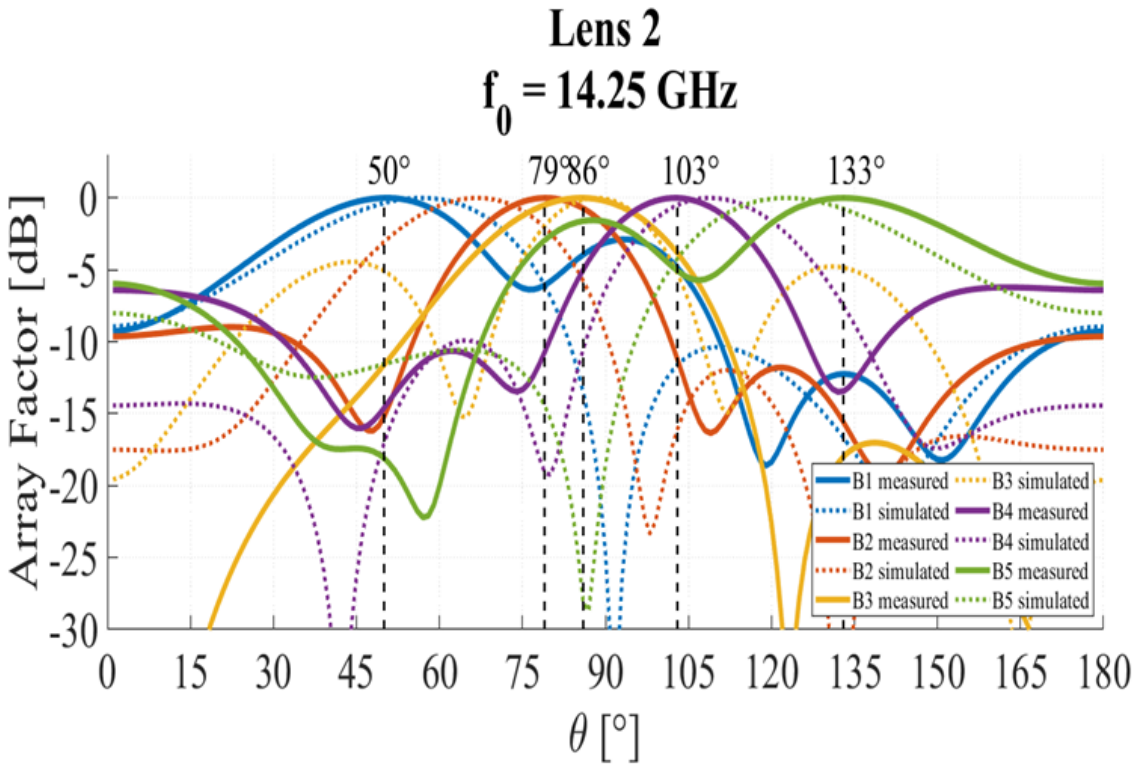

Figure 42 – Array factor calculated from measured S parameter. For the second lens at 14.25 GHz.

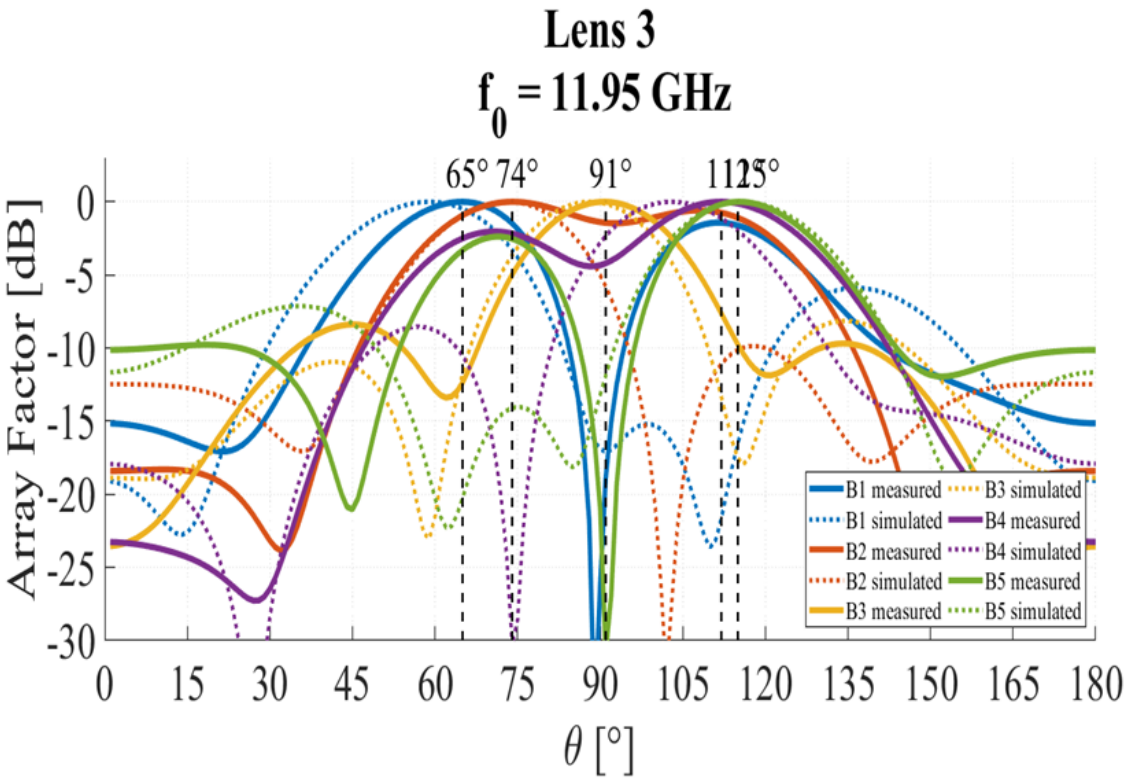

Figure 43 – Array factor calculated from measured S parameter. For the third lens at 11.95 GHz.

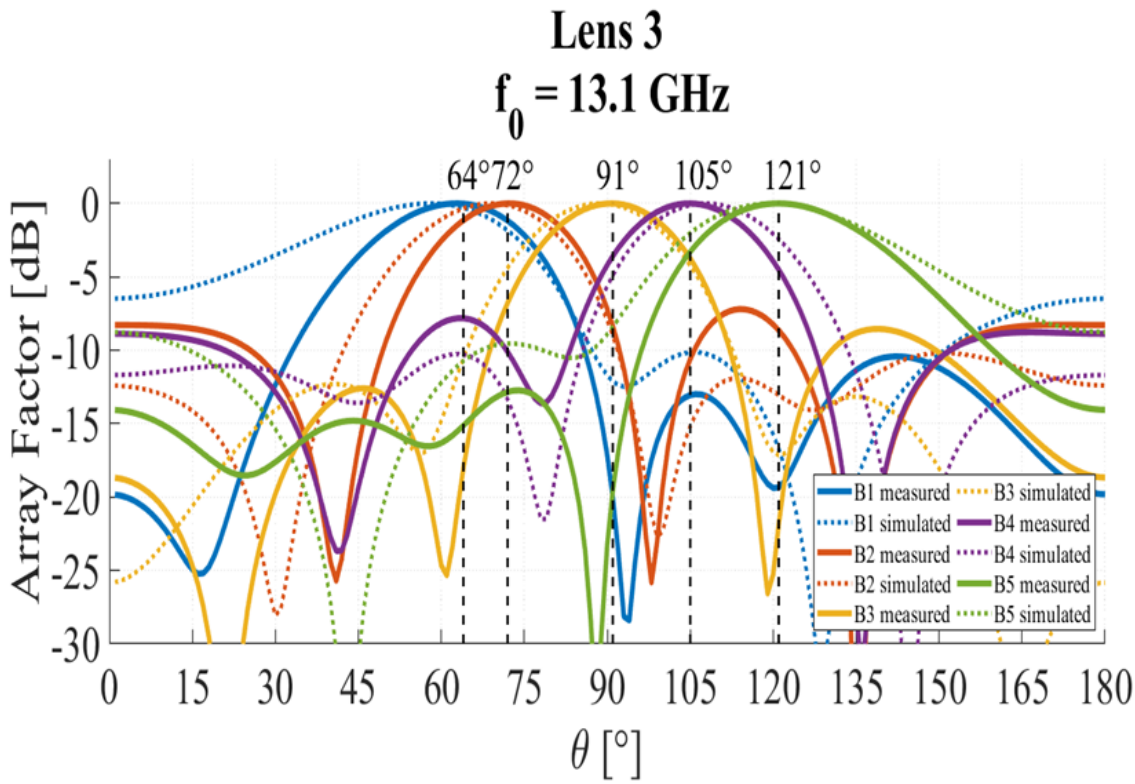

Figure 44 – Array factor calculated from measured S parameter. For the third lens at 13.10 GHz.

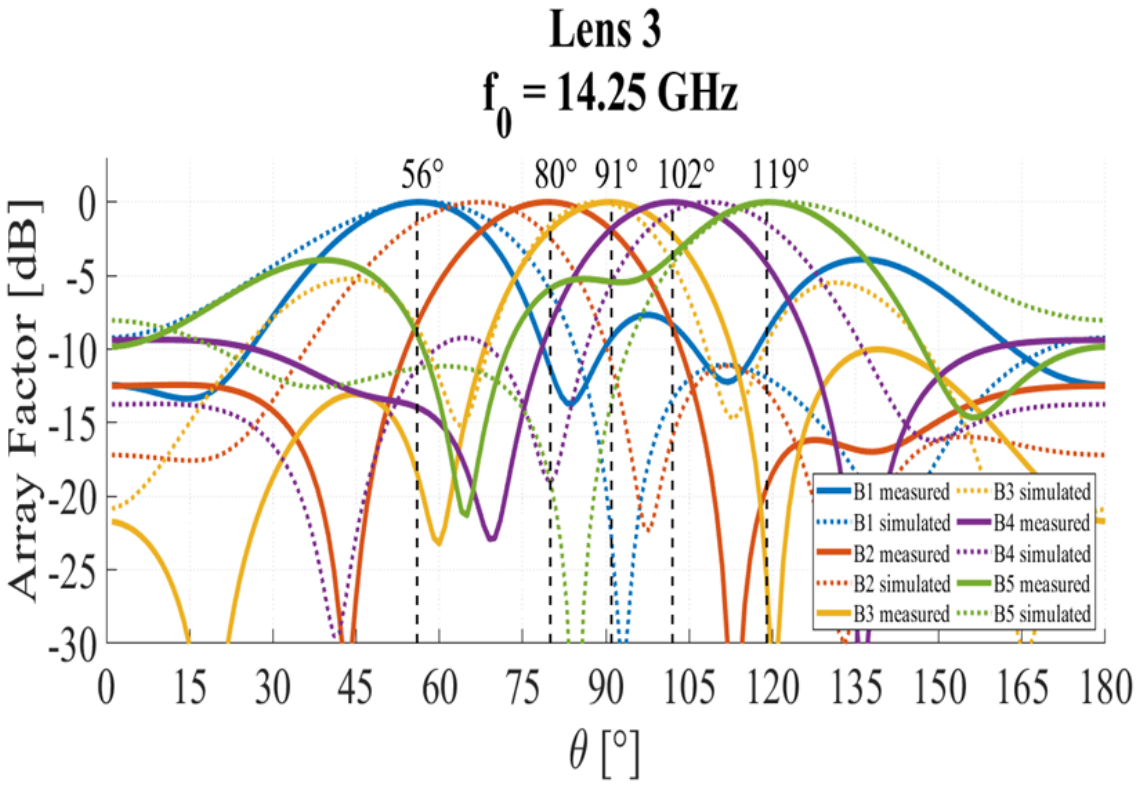

Figure 45 – Array factor calculated from measured S parameter. For the third lens at 14.25 GHz.

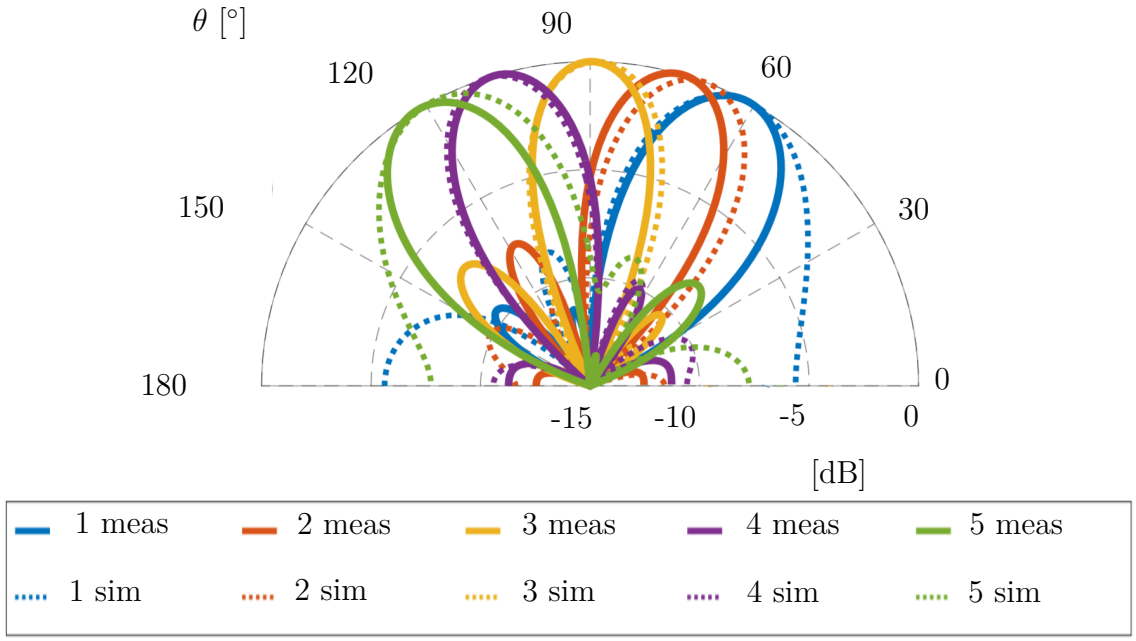

Figure 46 – Measured and simulated polar of the normalized array factor of θ-plane lens for all beam ports powered at 13.1 GHz. The measured and simulated values were close even with the imperfections caused by the manufacturing process the array factor is showed robust.

Table 6 – θ-plane Rotman lens characterization summary.

Beam #	θ-plane Rotman lens	
	$\|S_{11}\|$[dB]	IL [dB]
1	-15.9	-5.1
2	-8.8	-5.6
3	-8.8	-4.7
4	-9.3	-4.7
5	-10.3	-4.3

Note: Measurements carried out at 13.1 GHz.

The S-parameters of lenses from θ-plane lens stacks was analyzed separately as shown in figure 36, and presented in Table 6. The average reflection coefficient is -10.3 dB, and the average insertion loss is -4.87 dB. If we discount the transition loss, the insertion loss of the θ-plane lenses are -2.97 dB.

4.4.2 ϕ-plane Lenses Measurement (3 input by 4 output ports)

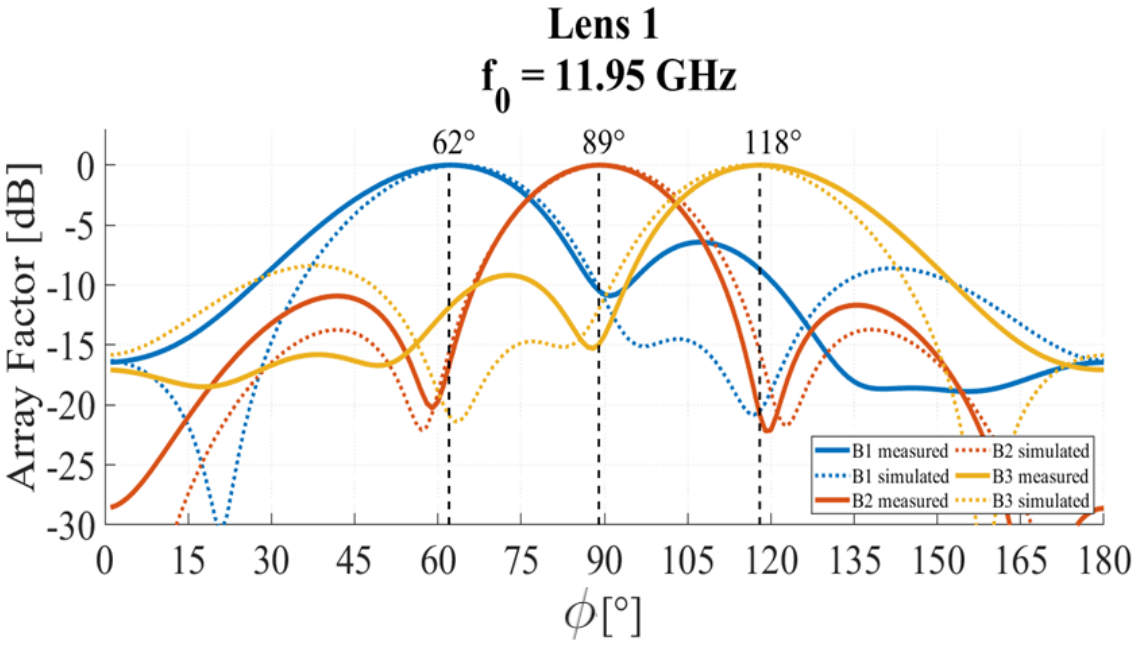

Figure 47 – ϕ-plane array factor calculated from measured S parameter. For the first lens at 11.95 GHz.

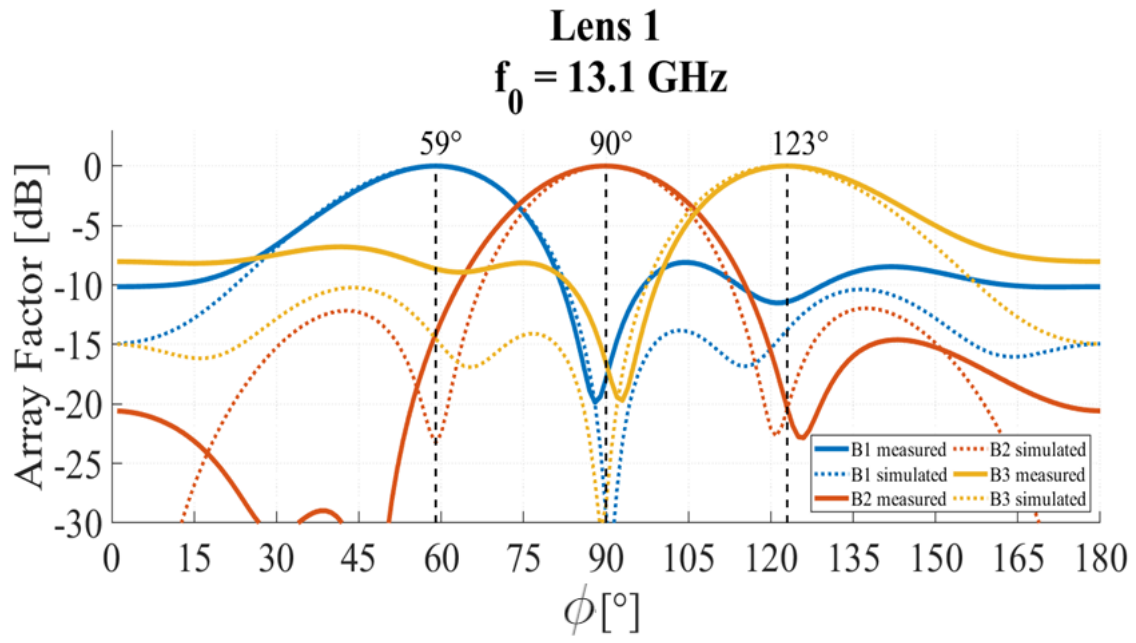

Figure 48 – ϕ-plane array factor calculated from measured S parameter. For the first lens at 13.10 GHz.

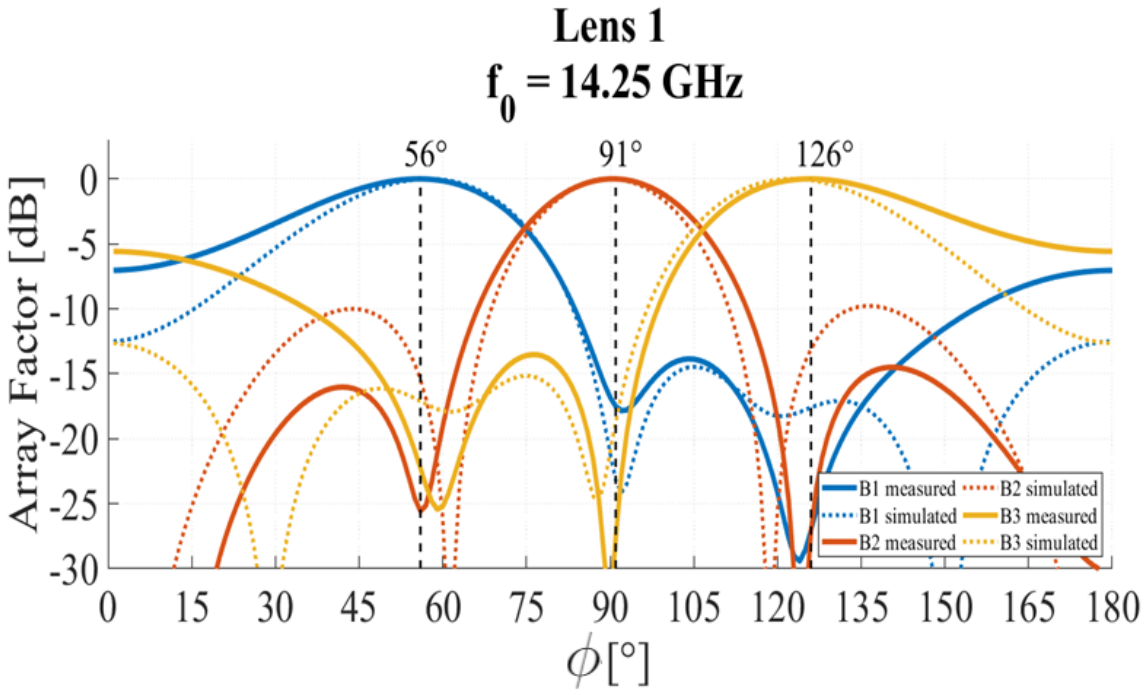

Figure 49 – ϕ-plane array factor calculated from measured S parameter. For the first lens at 14.25 GHz.

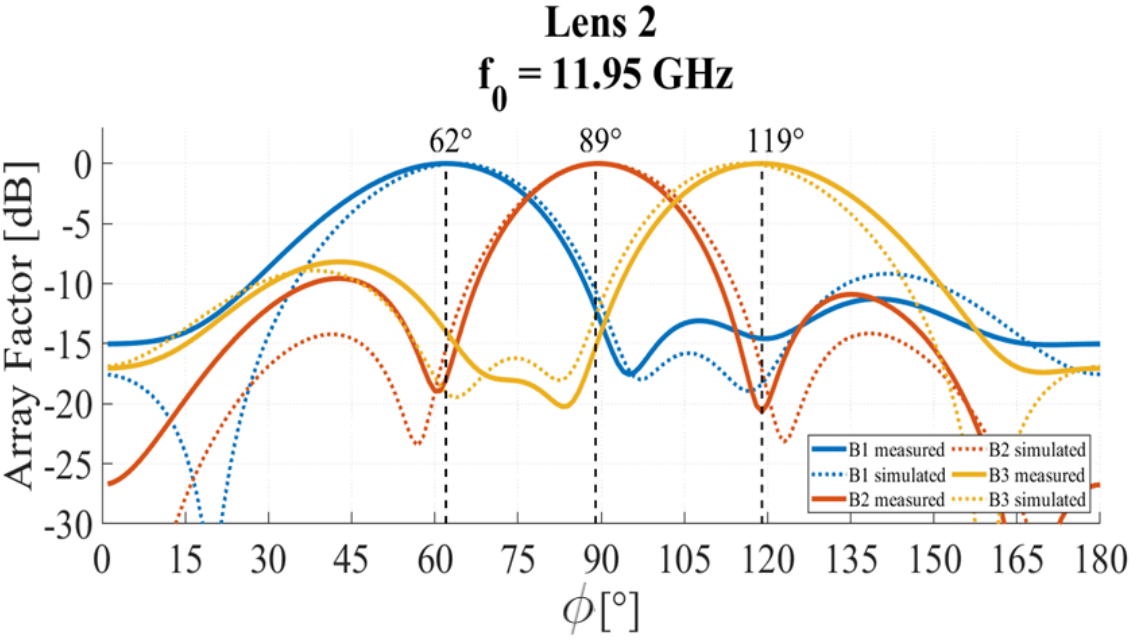

Figure 50 – ϕ-plane array factor calculated from measured S parameter. For the second lens at 11.95 GHz.

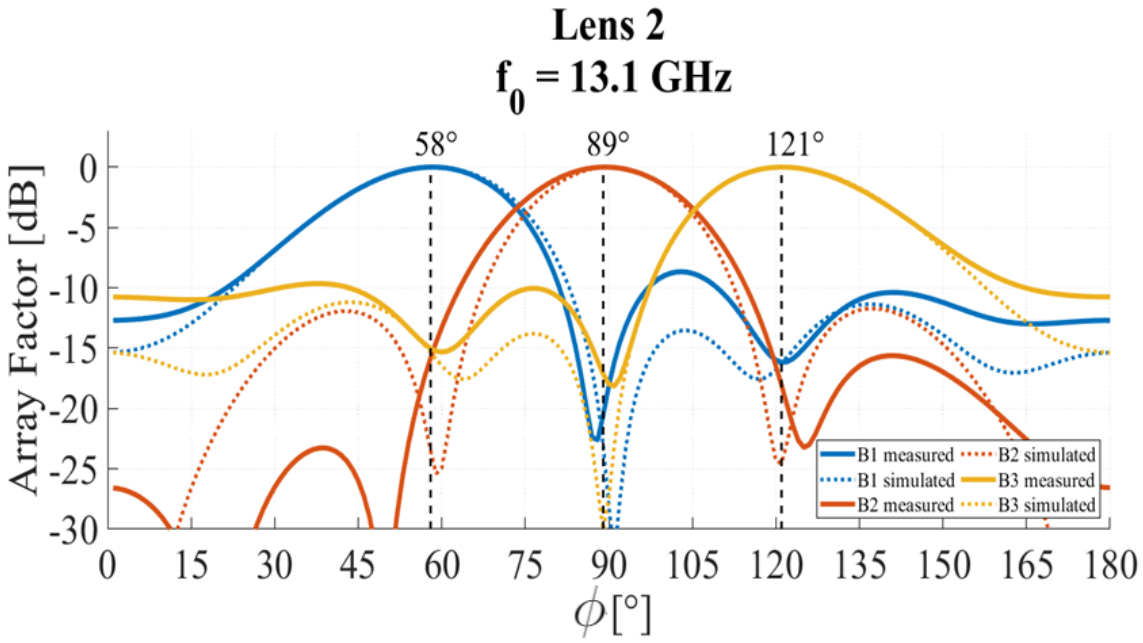

Figure 51 – ϕ-plane array factor calculated from measured S parameter. For the second lens at 13.10 GHz.

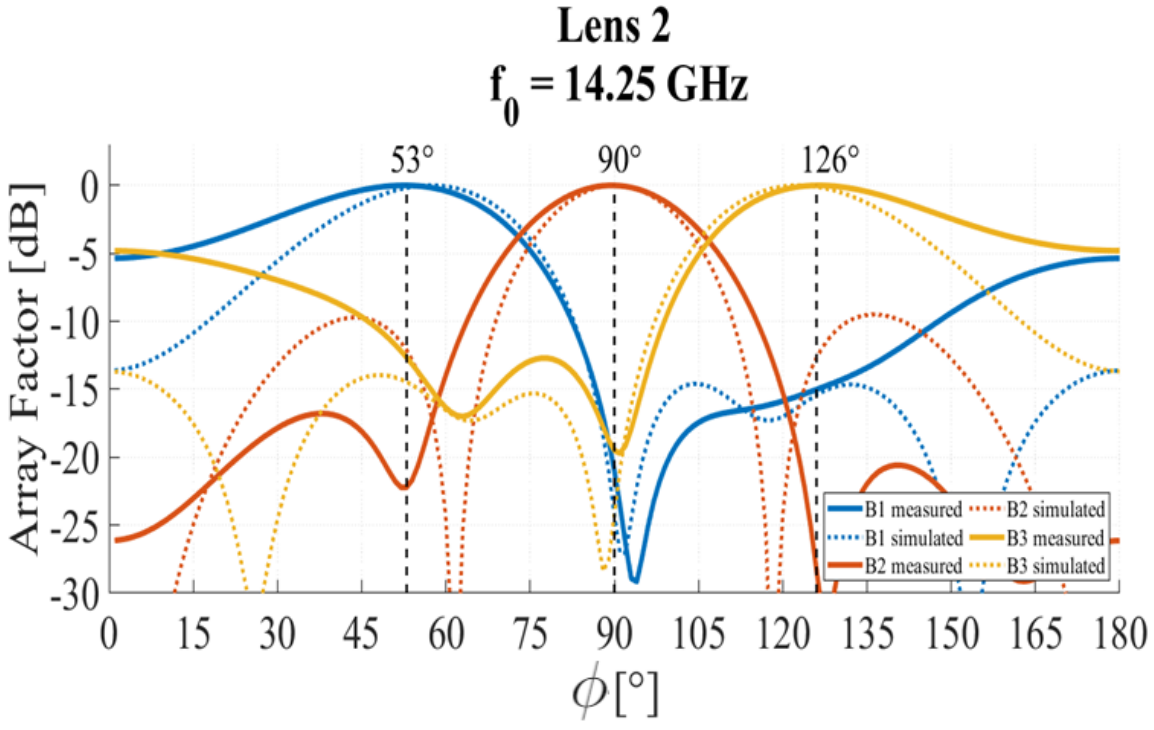

Figure 52 – ϕ-plane array factor calculated from measured S parameter. For the second lens at 14.25 GHz.

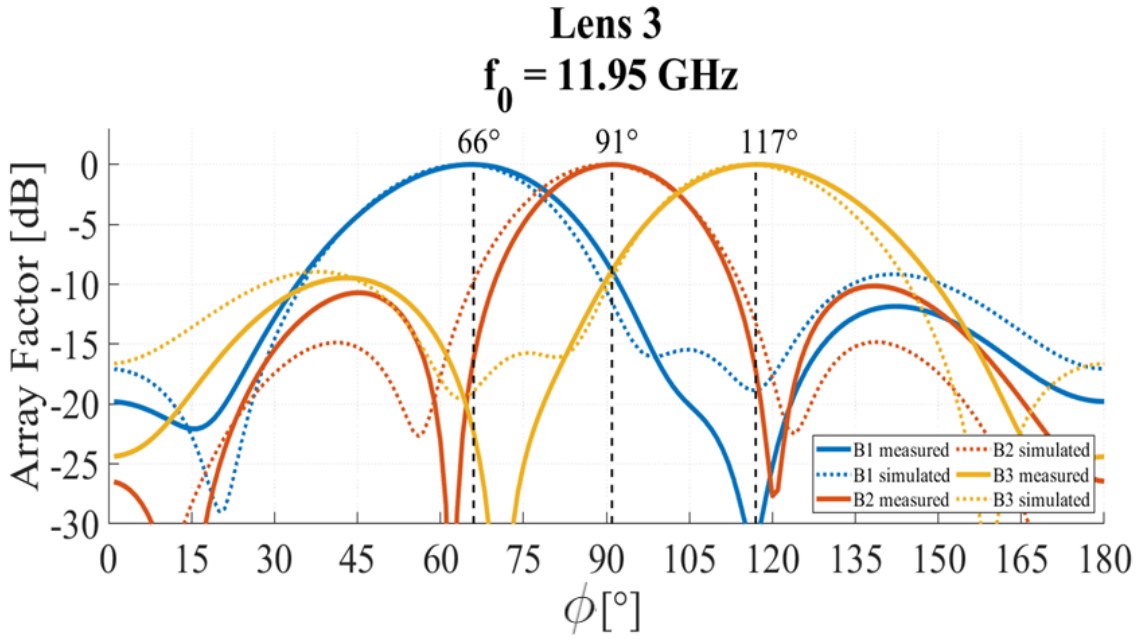

Figure 53 – ϕ-plane array factor calculated from measured S parameter. For the third lens at 11.95 GHz.

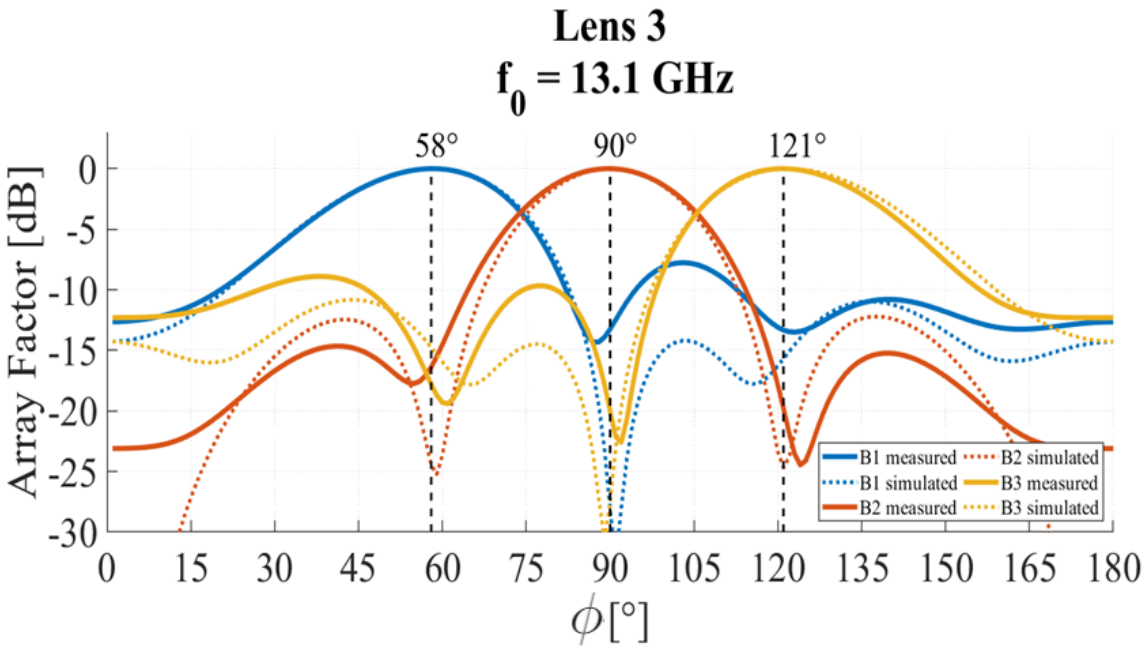

Figure 54 – ϕ-plane array factor calculated from measured S parameter. For the third lens at 13.10 GHz.

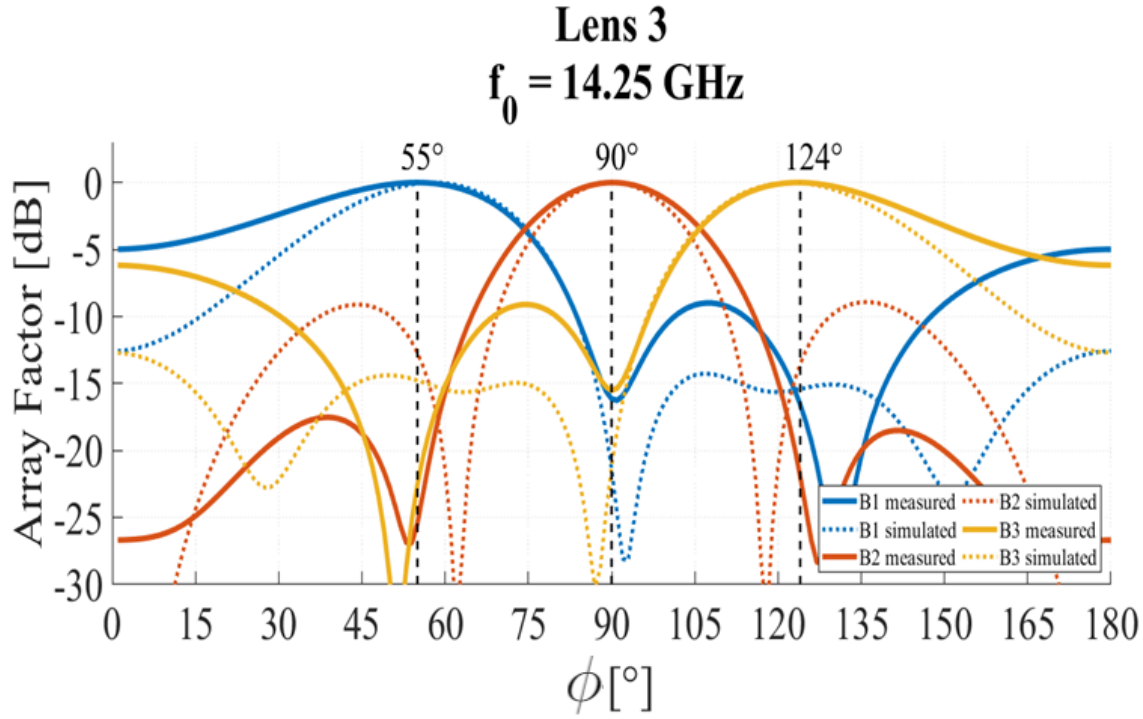

Figure 55 – ϕ-plane array factor calculated from measured S parameter. For the third lens at 14.25 GHz.

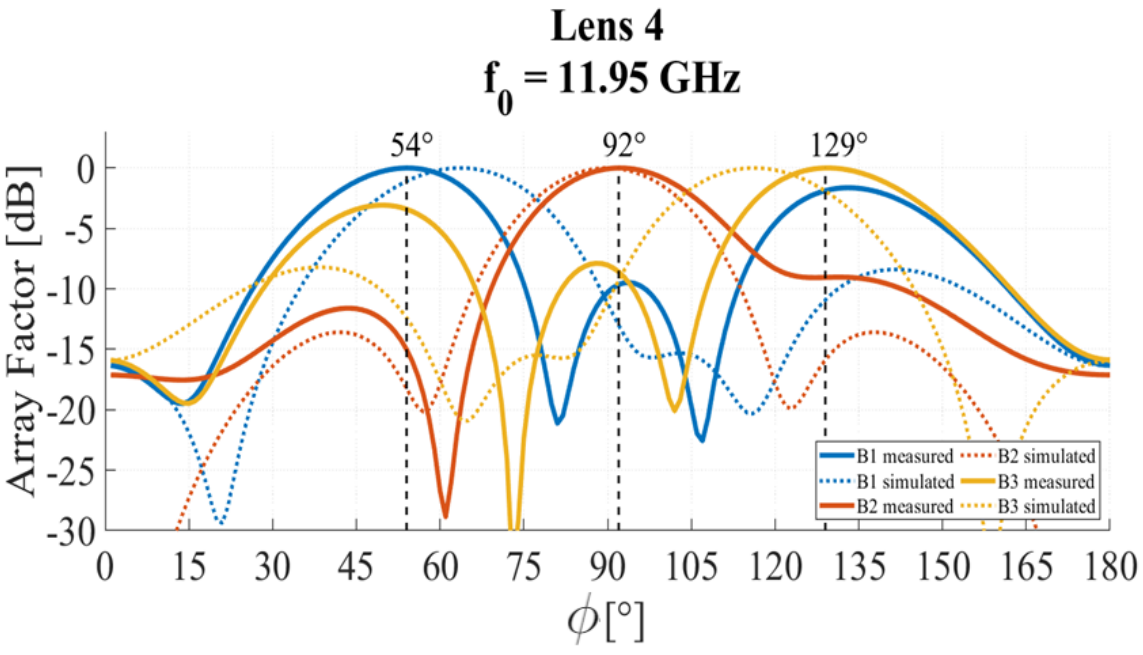

Figure 56 – ϕ-plane array factor calculated from measured S parameter. For the fourth lens at 11.95 GHz.

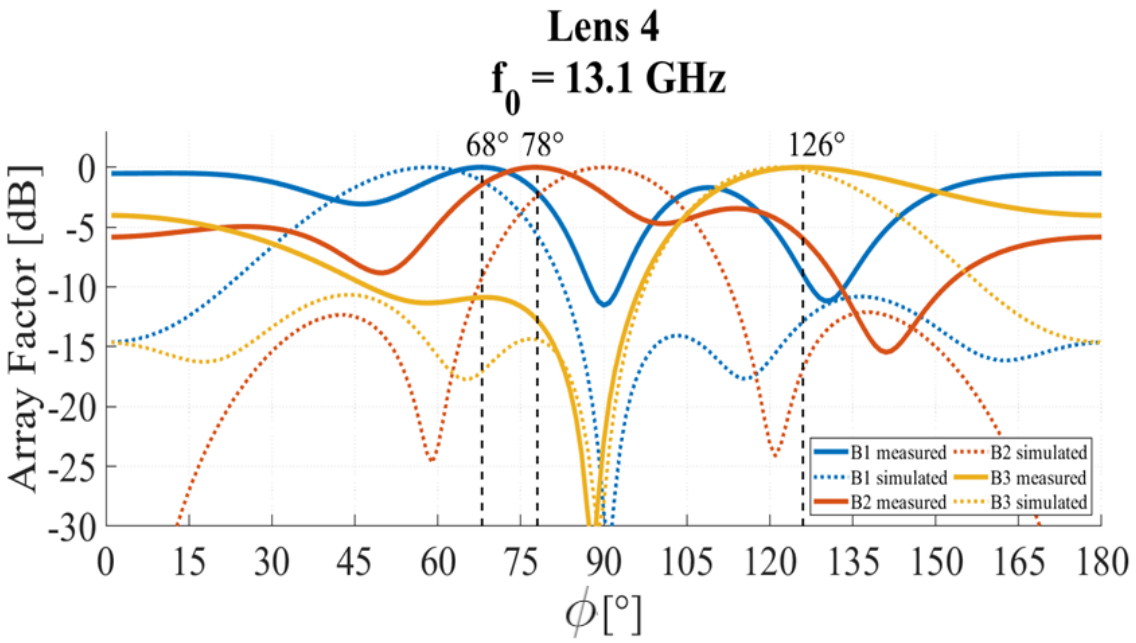

Figure 57 – ϕ-plane array factor calculated from measured S parameter. For the fourth lens at 13.10 GHz.

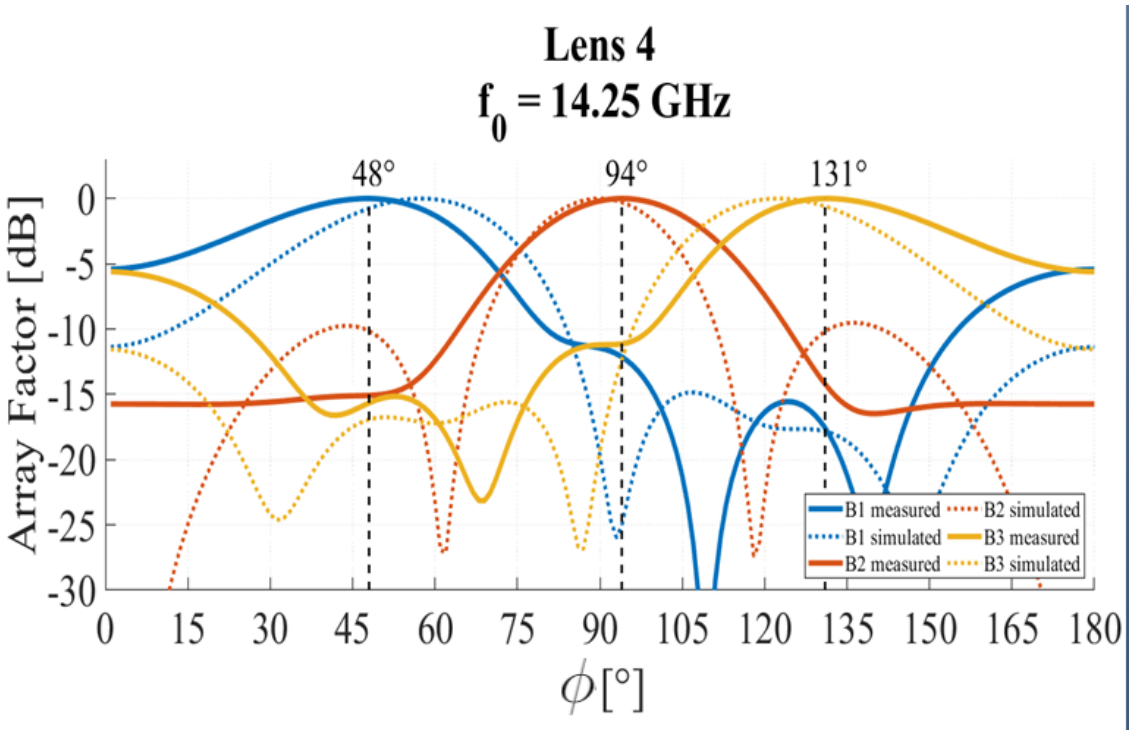

Figure 58 – ϕ-plane array factor calculated from measured S parameter. For the fourth lens at 14.25 GHz.

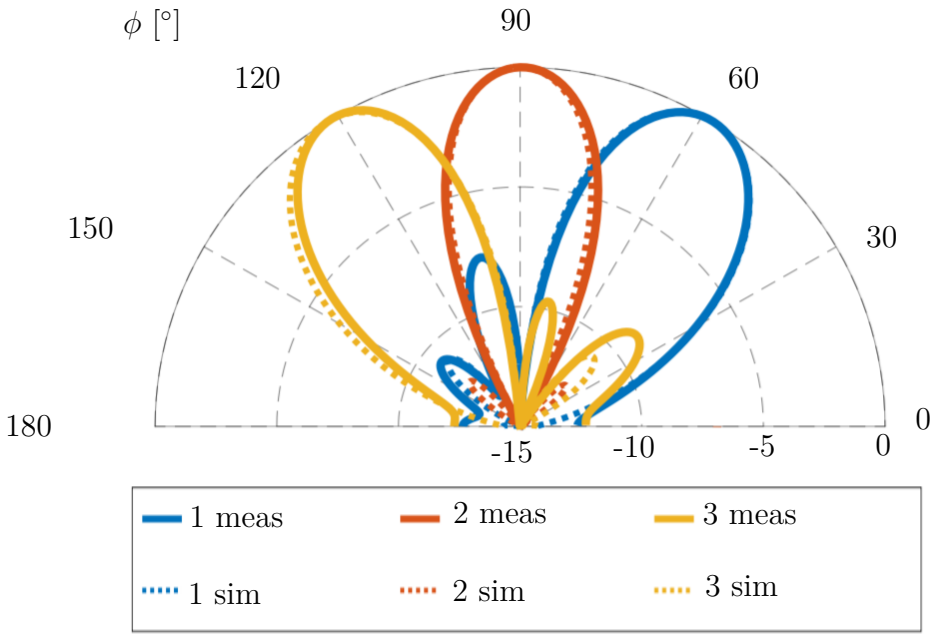

Figure 59 – Measured and simulated values of the normalized array factor of ϕ-plane lens for all beam ports powered at 13.1 GHz.

Table 7 – ϕ-plane Rotman lens characterization summary.

Beam #	ϕ-plane Rotman lens	
	$\|S_{11}\|$[dB]	IL [dB]
1	-21.8	-5.9
2	-13.1	-5.4
3	-25.2	-5.9

Note: Measurements carried out at 13.1 GHz.

The S-parameters of lenses from ϕ-plane was analyzed separately, are presented in Table 7. For the ϕ-plane lenses, the average reflection coefficient is -18.5 dB, and the average insertion loss is -5.72 dB. If we discount the transition loss, the insertion loss is -3.82 dB.

4.4.3 Conclusion

The scanning angle of the θ-plane lenses is $\pm 31\,^{\circ}$, while for the ϕ-plane lenses it is $\pm 29\,^{\circ}$. The measured values are consistent with the simulated values, and even with the imperfections the effects added by the capacitive transitions, the array factor proved to be robust. This is due to error reduction techniques applied, such as the distance between DM, the optimized g parameter. The length of the delay lines was parameter optimized to decrease the side lobe. Besides, the characteristic of the true time delay lens makes the energy inside the lens travel a real path and turns the lag robust in frequency bandwith, providing a very reliable array factor.

5 Phased Array Antenna

The phased array allows electromagnetic energy to exit the device. Kraus defines a radio antenna as "Structure associated with the region of transition between a guided wave and a free-space wave, or vice versa" (Kraus, 1988). Phased array has been showing itself to be a very suitable technology for beamforming systems, especially associated with microstrip technology. Currently a search with the words "phased array antenna" on the IEEE Xplore platform returns 27k articles, of which a significant percentage implementing microstrip.

5.1 Radiant System Assembly

The boards have been assembled using bullets SMPs, EM simulations of their performance were made, the result of are located in Figure 60. The reflection coefficient was better than -18 dB in the entire required range. Figure 61 (a) shows the bullets in the template guide and Figure 61 (b) shows the connected boards.

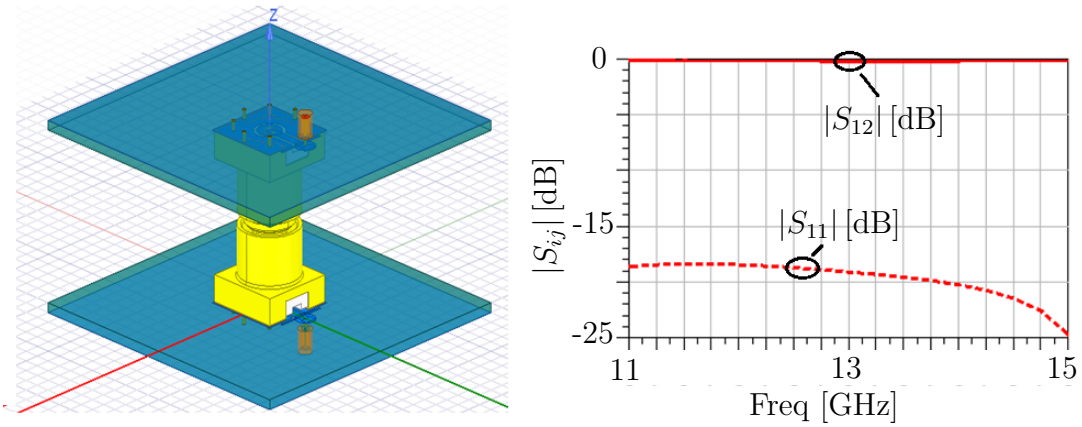

Figure 60 – Simulation of SMP bullets transition.

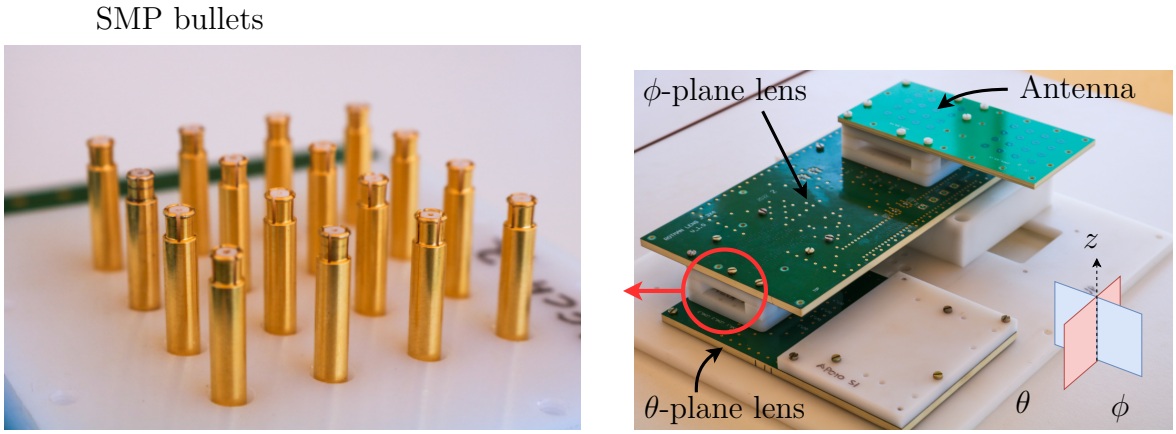

(a) (b)

Figure 61 – (a) SMP coaxial bullets used for board interconnections. (b) Photography of the entire system mounted. A nylon structure is used to provide mechanical steadiness. Here it can be seen that the system is planar, and the separation between each plane is only due to prototyping reasons.

5.2 Results

The photograph shown in Figure 62 bring the fabricated phased array antenna. The array was made using the elementary element *Circular Microstrip Broadband* detailed in the subsection 3.2.1.

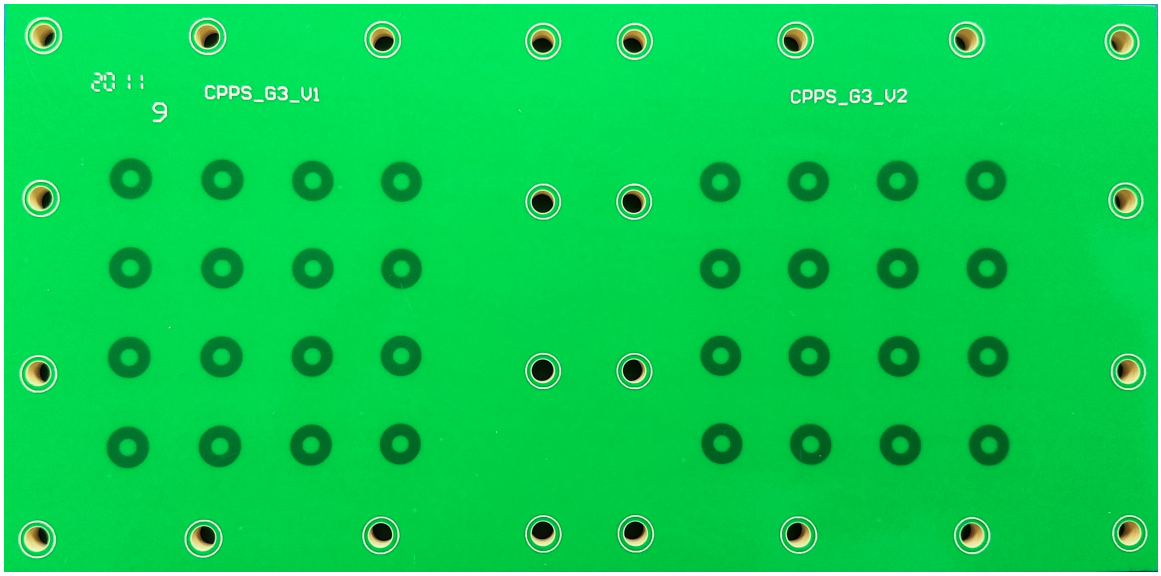

Figure 62 – Fabricated antenna array PCB. The board has 2 arrays that are identical, with exception of the variables d_3 and w_2. On the top side of the picture, d_3 is decreased by 30 μm and w_2 by 10 μm in relation to what is used in the array on the bottom. The elements on each array are spaced of 11.45 mm, which corresponds to half wavelength in vacuum at 13.1 GHz.

The system has been characterized in far-field using a standard horn antenna as a

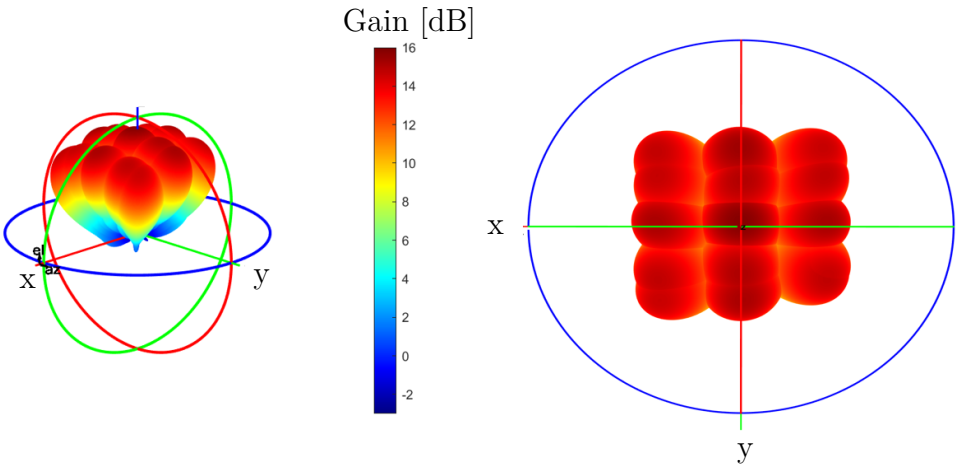

Figure 63 – Full wave simulation of the antenna array coupled with lenses.

reference element. It has been connected to an Agilent E8251A Signal Generator, and the antenna under test (AUT) has been connected to a Keysight N9917B FieldFox Handheld Microwave Analyzer, used as spectrum analyzer (SA), as shown in the figures 64 and 65.

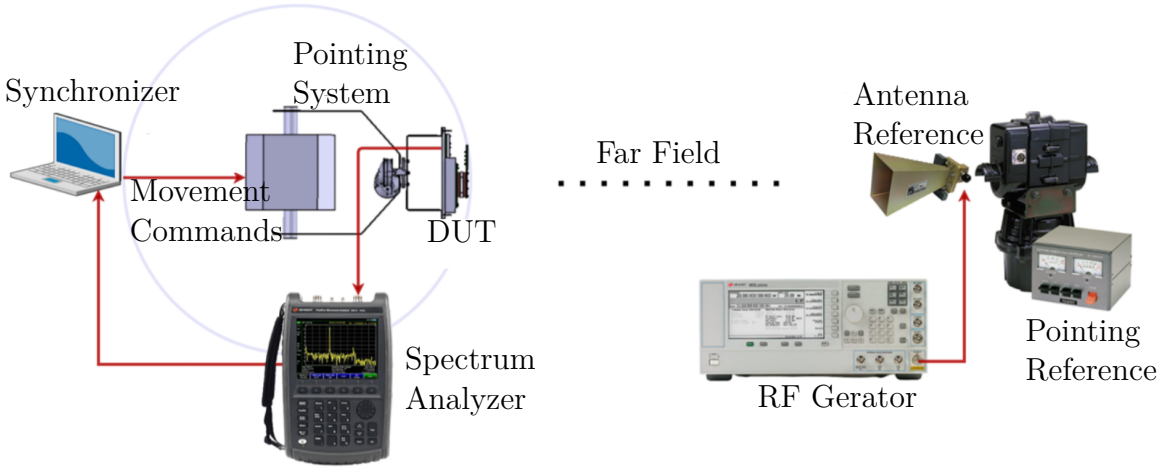

Figure 64 – Setup measurement radiation pattern.

The test structure has been mounted on a counter-weight with bulky metal parts that acted as secondary sources, causing some diffraction on diagrams observed in Figures 66, 67, 68, 69, 70, 71, 72. This effect can be observed on the power fluctuations around maximum beam directions. This can hide the real maximum radiated power and also slightly impacts the scan loss. Nevertheless, each lens array factor does not present any of this effect, which confirms that the perturbation is only related to this interfering radiation.

It can be seen that the beams are correctly steered in both planes, having the 15 beams pointing in different directions in space (figure 63), resulting from the combination of the angles ϕ and θ.

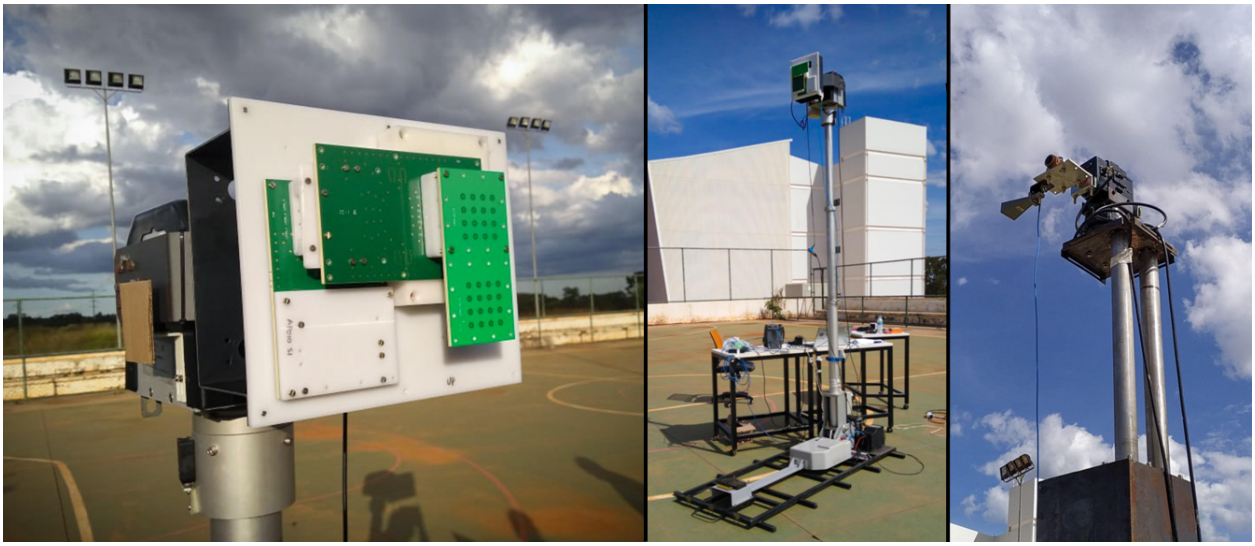

Figure 65 – Photograph of setup measurement of radiation pattern.

5.2.1 Radiation Pattern Measurament at 11.95 GHz

In order to validate the proposed architecture, small lenses and arrangements were designed. A lot of beam ports and array ports is theoretically required in a precise system with many narrow beams. Aberrations and secondary lobes reduce as the system grows, making it an easily scalable architecture. It can be seen that at 11.95 GHz the beams get wider, this happens because the aberrations increase when away from the center frequency, and the length of the antenna array gets smaller if normalized by the wave-length.

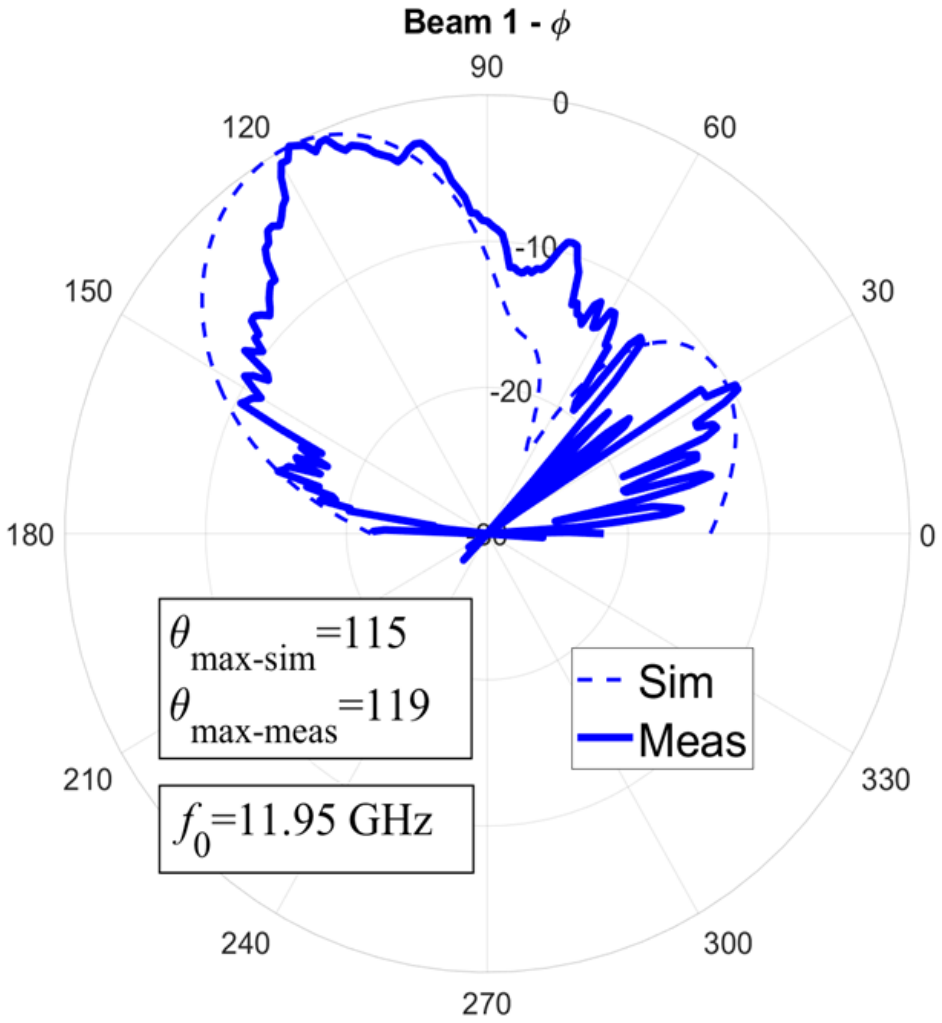

Figure 66 – Radiation pattern measured (solid line) and simulated (dashed line) in the central frequency of the reception band. When powered to port J1 (reference on Figure 33).

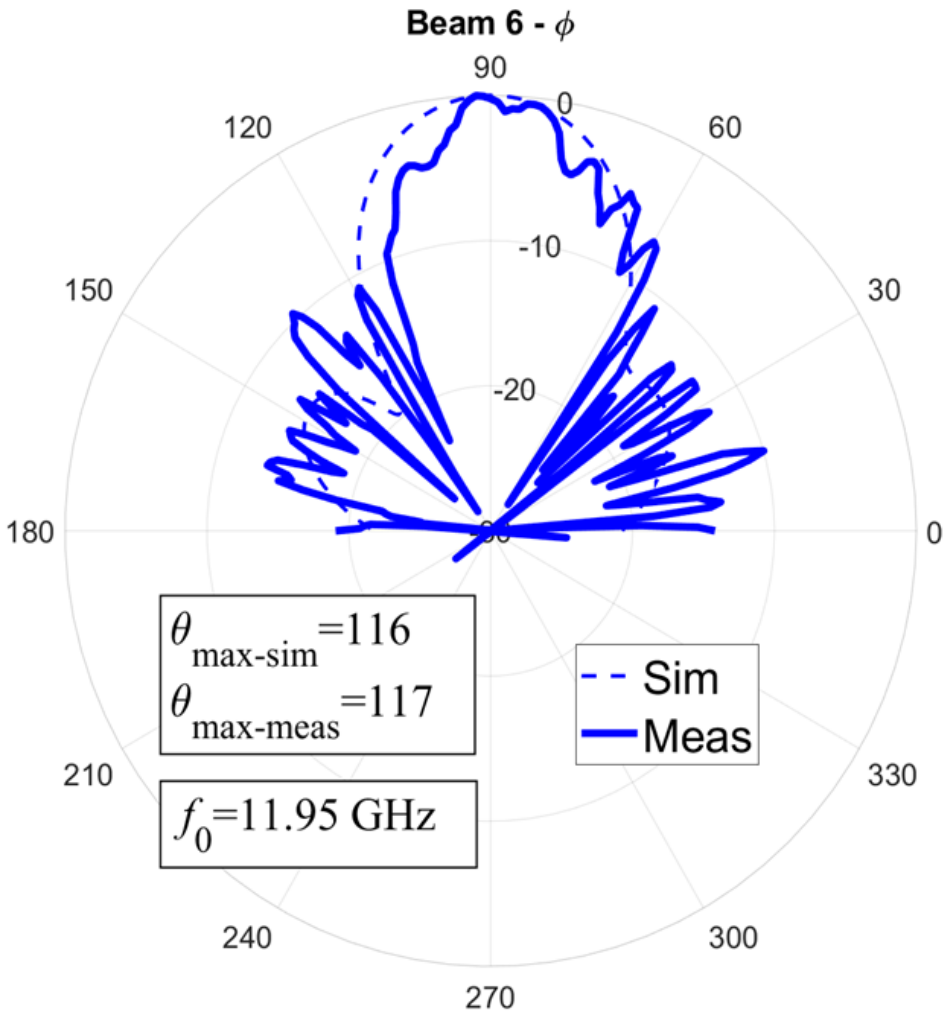

Figure 67 – Radiation pattern measured (solid line) and simulated (dashed line) in the central frequency of the reception band. When powered to port J10 (reference on Figure 33).

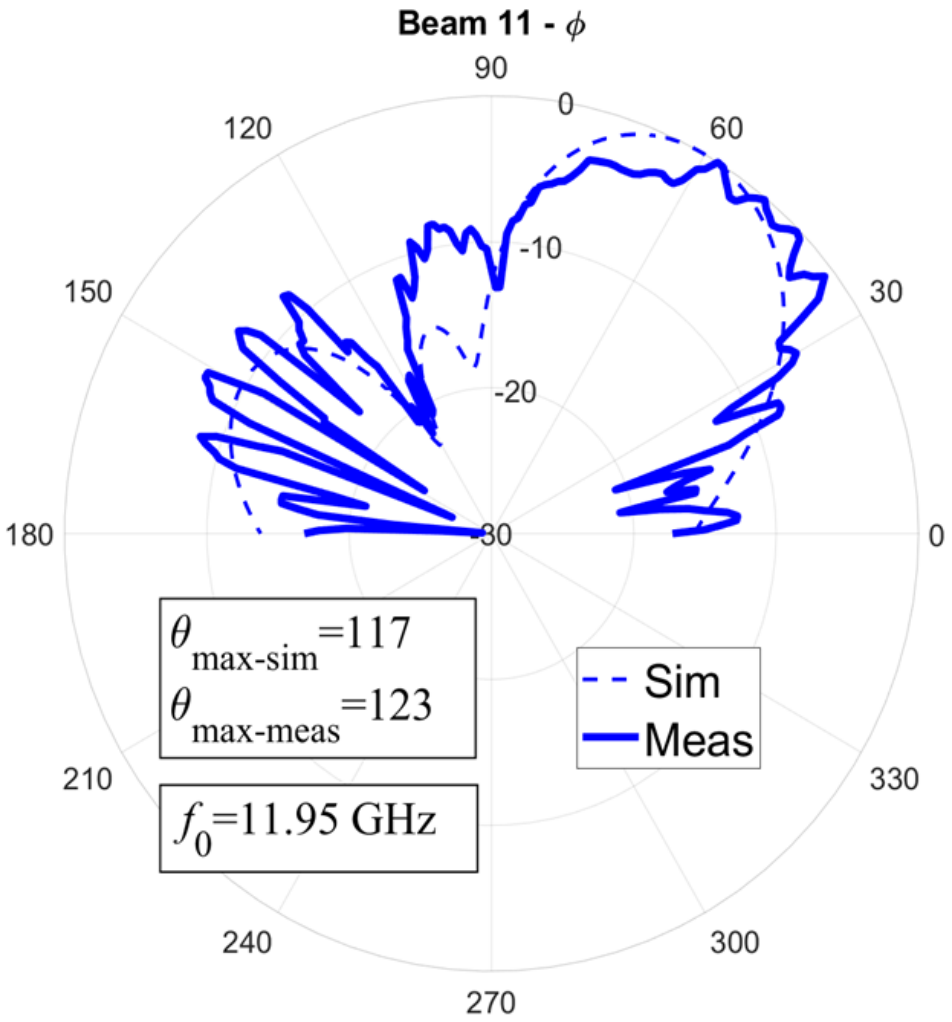

Figure 68 – Radiation pattern measured (solid line) and simulated (dashed line) in the central frequency of the reception band. When powered to port J19 (reference on Figure 33).

5.2.2 Radiation Pattern Measurament at 14.25 GHz

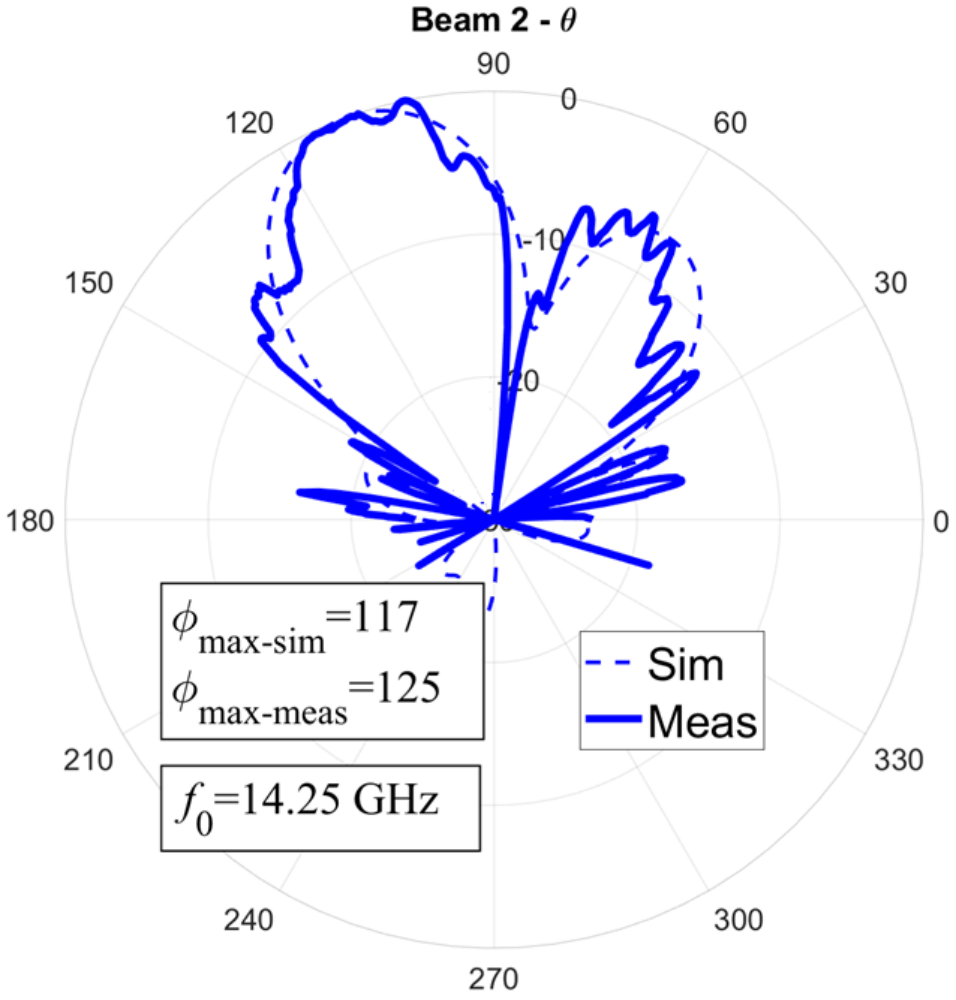

Figure 69 – Radiation pattern measured (solid line) and simulated (dashed line) in the central frequency of the reception band. When powered to port J2 (reference on Figure 33).

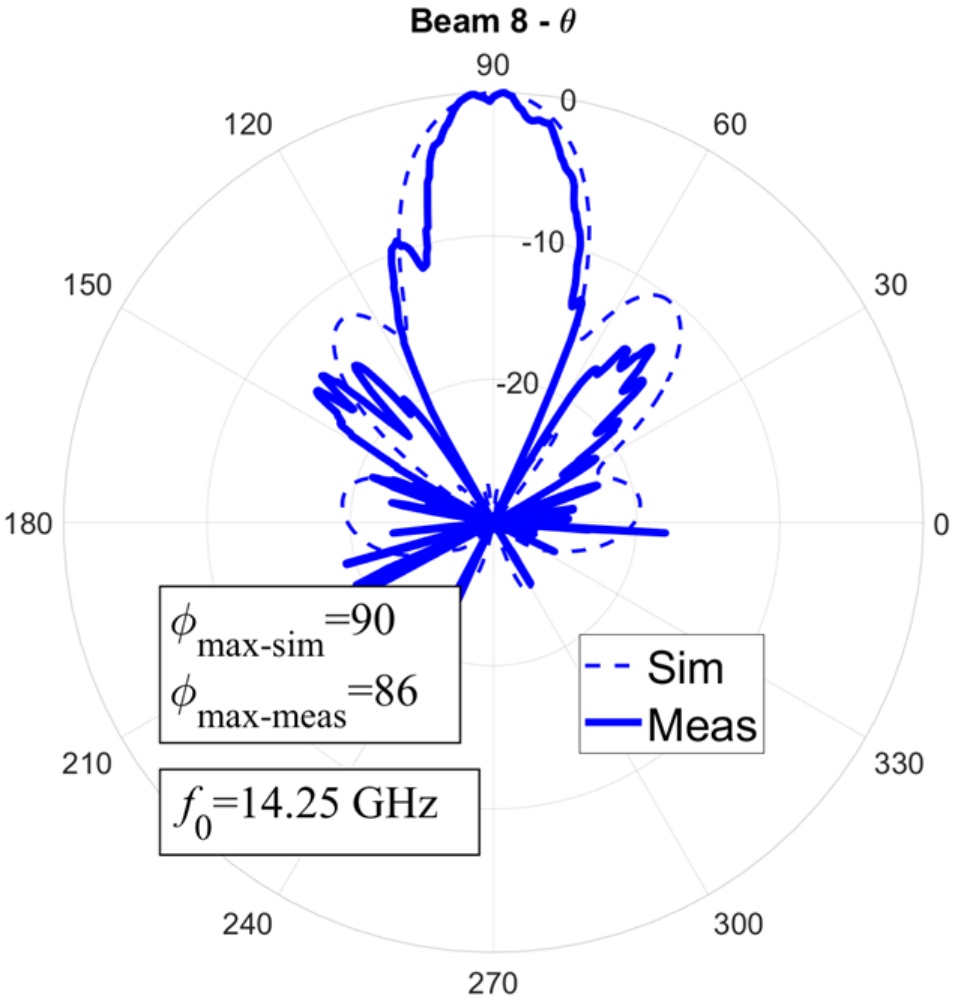

Figure 70 – Radiation pattern measured (solid line) and simulated (dashed line) in the central frequency of the reception band. When powered to port J12 (reference on Figure 33). This is the central beam in both planes.

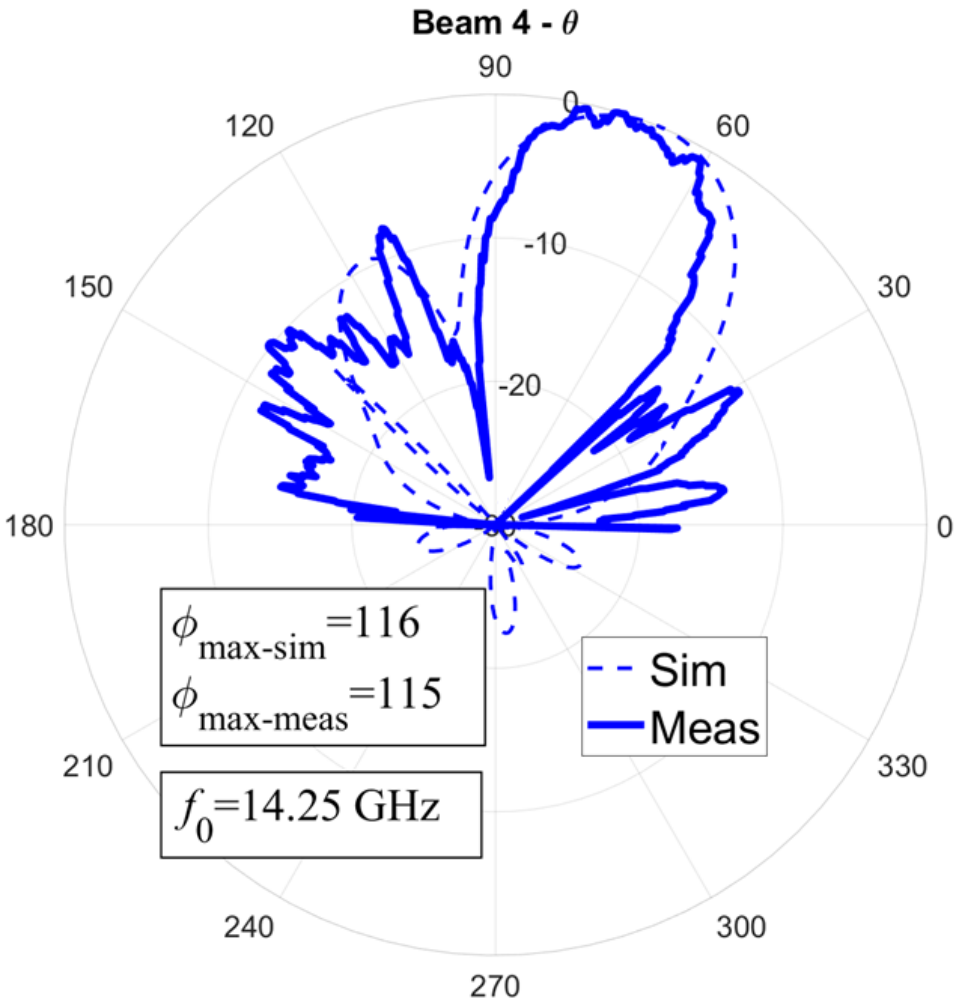

Figure 71 – Radiation pattern measured (solid line) and simulated (dashed line) in the central frequency of the reception band. When powered to port J4 (reference on Figure 33).

5.2.3 Radiation Pattern Measurament at 13.1 GHz

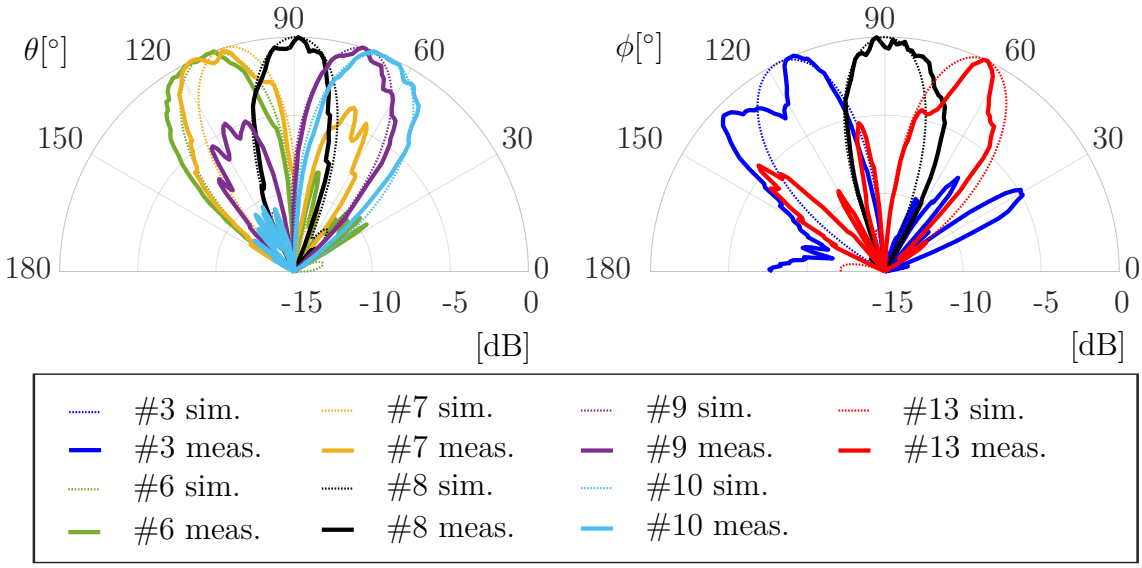

Figure 72 – Normalized radiation pattern of central beams over θ and ϕ planes at $f = 13.1\,\text{GHz}$, with $\phi = 90°$ and $\theta = 90°$, when scanning the other plane. The power fluctuations around maximum beam directions occurred due to unavoidable metal parts in the testing structure, which acted as secondary sources, causing diffraction effects that affected the radiation pattern measurement.

Table 8 – Scan-loss of each main beam.

Beam #	ϕ [°]		θ [°]		Scan-loss [dB]	
	Sim.	Meas.	Sim.	Meas.	Sim.	Meas.
1	125	109	117	118	2.5	0.84
2	119	112	107	102	0.9	0.59
3	117	113	89	93	0.9	2.27
4	120	110	71	66	0.9	0.36
5	122	115	62	63	2.5	1.39
6	90	88	112	110	0.8	0.07
7	90	91	107	116	0.1	0
8	90	92	90	89	0	0.57

Note: Maximum beam directions and power magnitude relative to the beam of highest power at $f = 13.1\,\text{GHz}$, representing the scan loss.

The maximum gain measured at 13.1 GHz was 4.9 dB at beam 7. The relative maximum power for each beam and its angles are presented in table 8. The reduced level in comparison to the antenna array gain is due to the path losses through the lenses. The scan loss is better than 2.28 dB.

6 Conclusion

The proposed system has been successfully designed to be compatible with the IPC-2252 standard for industrial RF PCB manufacture. It posses 15 beams pointing in different directions, with beam scanning in two orthogonal planes. The measured beams are in agreement with the simulations. Therefore, it is shown that the system can be used in land applications that need fast beam switching, either for adapting direction during terminal movement or for commuting the link to another satellite.

Even with the high risk associated with the manufacturing process, we have reached the limit of the technical capabilities of *Sequentital Build Up* technology. Test rounds of microstrip circuits were manufactured with Brazilian companies, but none of them met the technical requirements. The radiating system was sent for manufacturing in a foreign company, even though the manufacturing company warned of the high risk of failure, we achieved a prototype with good electrical and mechanical performance.

The antenna design includes several methods to increase bandwidth and set the axial ratio to attend circular polarization. Those insights are validated, proving that, despite its relatively narrow band intrinsic characteristic, the patch antenna can be enhanced to cover both reception and transmission frequency bands in the Ku-band.

The Rotman lens has shown to be a robust solution for beamforming. Although the need for large operation bandwidth generates aberrations, the pointing angles fit the predictions. Therefore, it is a reliable solution for the proposed system.

The orthogonal interconnection of lenses and antenna array is done in a planar structure, which improves mechanical strength and optimizes space usage. Given the manufacturing procedures, the multi-layer capacitive transition has been an essential technique to achieve that feature, being strongly robust to manufacturing variations. Moreover, this type of transition can be used in other designs to work-around industrial process limitations.

To have a modular prototype that can be individually characterized, the boards had been assembled using a board-to-board adaptor. Nevertheless, the system can be manufactured in one single board or assembling them with a BGA-like soldering process, which drastically reduces the mass production cost of the final product. Consequently, the presented work turns out to be a tremendously reduced profile multi-beam antenna.

It is possible to fine-tune the beam and consequently improve the resolution for RWR radar applications by increasing the number of antenna cells, as shown in Graphic 16 the coupling between neighboring antennas is better than -20 dB in the operating range,

being a scalable solution.

As future work, it is logically suggested, for industrial scale production, to consider Rotman lenses fabricated in low-temperature cofired ceramic (LTCC) technology. The DuPont company has the capacity to manufacture stacks with more than 100 layers (DuPont, 2021). It eliminates the problem shown in Chapter 2. The superior dielectric constant reduces the size of the Rotman lens. It is also possible to include active components, this has the potential to increase the SNR ratio, by the Friss equation, improves SNR when LNAs are closer to the antennas.

Bibliography

ALBULET, M. *SPACEX NON-GEOSTATIONARY SATELLITE SYSTEM*. [S.l.], 2016. Citado na página 15.

Alessandro, S. et al. Analog beamforming network for ka band satellite on the move terminal with phase shifting technique based on i/q mixer. In: *2015 European Radar Conference (EuRAD)*. [S.l.: s.n.], 2015. p. 445–448. Citado na página 15.

Attaran, A.; Rashidzadeh, R.; Kouki, A. 60 ghz low phase error rotman lens combined with wideband microstrip antenna array using ltcc technology. *IEEE Transactions on Antennas and Propagation*, v. 64, n. 12, p. 5172–5180, 2016. Citado 2 vezes nas páginas 50 and 51.

Babar Abbasi, M. A.; Fusco, V. F.; Matthaiou, M. Millimeter wave hybrid beamforming with rotman lens: Performance with hardware imperfections. In: *2019 16th International Symposium on Wireless Communication Systems (ISWCS)*. [S.l.: s.n.], 2019. p. 203–207. Citado 2 vezes nas páginas 17 and 58.

Balanis, A. C. Microstrip and mobile communications antennas. In: _____. *Anntena theory: Analysis and Design*. [S.l.]: John Wiley & Sons, 2016. p. 783. Citado 3 vezes nas páginas 27, 30, and 44.

Balanis, A. C. Microstrip and mobile communications antennas. In: _____. *Anntena theory: Analysis and Design*. [S.l.]: John Wiley & Sons, 2016. p. 860. Citado na página 29.

Blackshear, E. D. The evolution of build-up package technology and its design challenges. *IBM Journal of Research and Development*, v. 49, 2005. Citado na página 21.

Cheung, S. et al. A broadband dual-circular polarization patch antenna using quadruple l-probe feed. *IEEE International Symposium on Antennas and Propagation and USNC/URSI National Radio Science Meeting*, 2017. Citado na página 32.

Dassault Systemes. *Antenna Magus*. 2019. Disponível em: <https://www.3ds.com/products-services/simulia/products/antenna-magus/>. Citado na página 39.

DELOS, P. *An Interview with Analog Devices Discussing RF Electronics for Phased Array Applications*. [S.l.], 2020. Citado na página 17.

Dong, G. et al. Research on the influence of vias on signal transmission in multi-layer pcb. In: *13th IEEE International Conference on Electronic Measurement Instruments (ICEMI)*. [S.l.: s.n.], 2017. p. 406–409. Citado na página 21.

DuPont. *DuPont Green Tape 951*. [S.l.], 2021. Disponível em: <https://www.dupont.com/products/greentape-951-ltcc-material-system.html>. Citado na página 88.

Eom, S. Y. et al. Design and test of a mobile antenna system with tri-band operation for broadband satellite communications and dbs reception. *IEEE Transactions on Antennas and Propagation*, v. 55, n. 11, p. 3123–3133, 2007. Citado na página 15.

European Space Agency. *Microwave lenses harnessed for multi-beam forming*. 2020. Citado na página 17.

FCC News. *FCC AUTHORIZES SPACEX TO PROVIDE BROADBAND SERVICES VIA SATELLITE CONSTELLATION*. [S.l.], 2018. Citado na página 15.

Fuchs, B. et al. Modeling, design and performances of half maxwell fish-eye lens antennas. In: *IEEE European Conference on Antennas and Propagation*. Edinburgh, UK: [s.n.], 2007. Citado na página 15.

Fuchs, B. et al. Scattering of spherically and hemispherically stratified lenses fed by any real source. *IEEE Transactions on Antennas and Propagation*, v. 56, n. 2, p. 450–460, 2008. Citado na página 15.

George, R.; Castro, A.; Sharma, S. Comparison of a four stage sequentially rotated wideband circularly polarized high gain microstrip patch array antennas at ku-band. *European Conference on Antennas and Propagation (EUCAP)*, 2017. Citado 2 vezes nas páginas 5 and 38.

HALL, L. T.; HANSEN, H. J.; ABBOTT, D. Rotman lens for mm-wavelengths. In: INTERNATIONAL SOCIETY FOR OPTICS AND PHOTONICS. *Smart Structures, Devices, and Systems*. [S.l.], 2002. v. 4935, p. 215–221. Citado na página 17.

Hall, P. S. Application of sequential feeding to wide bandwidth, circularly polarised microstrip patch arrays. *IEE Proceedings H - Microwaves, Antennas and Propagation*, v. 136, n. 5, p. 390–398, 1989. Citado 2 vezes nas páginas 5 and 38.

Hall, P. S.; Vetterlein, S. J. Review of radio frequency beamforming techniques for scanned and multiple beam antennas. *IEE Proceedings H - Microwaves, Antennas and Propagation*, v. 137, n. 5, p. 293–303, 1990. Citado na página 17.

Hamici, Z. Fast beamforming with fault tolerance in massive phased arrays using intelligent learning control. *IEEE Transactions on Antennas and Propagation*, v. 67, n. 7, p. 4517–4527, 2019. Citado na página 15.

Harrington, R. F. Time-harminic eletromagnetc fields. In: _____. [S.l.]: John Wiley and Sons, 2001. cap. 2, p. 38. Citado na página 101.

Harrington, R. F. Time-harminic eletromagnetc fields. In: _____. [S.l.]: John Wiley and Sons, 2001. cap. 5, p. 198. Citado na página 102.

Ho, I. An Ovenview of SBU (Sequential Build-Up)/Microvia Technologies. In: *Proceedings, 3rd International Symposium on Advanced Packaging Materials Processes, Properties and Interfaces*. [S.l.: s.n.], 1997. Citado na página 21.

ITU. *Maximum permissible level of off-axis e.i.r.p. density from very small aperture terminals (VSATs)*. [S.l.], 1995. Citado na página 15.

Johannsen, K.; Mathur, U. Tvro antenna size, ku band versus c band. *IEEE Transactions on Broadcasting*, BC-33, n. 3, p. 84–88, 1987. Citado na página 15.

Kim, D. et al. Fully digital beamforming receiver with a real-time calibration for 5g mobile communication. *IEEE Transactions on Antennas and Propagation*, v. 67, n. 6, p. 3809–3819, 2019. Citado na página 15.

Kraus, J. D. *Antennas*. 2. ed. [S.l.]: McGraw-Hill, 1988. Citado na página 75.

Lafond, O. et al. Millimeter wave reconfigurable antenna based on active printed array and inhomogeneous lens. In: *IEEE European Microwave Conference*. Amsterdam, The Netherlands: [s.n.], 2008. Citado na página 15.

Lafond, O. et al. Reconfigurable antenna in mm-waves based on stratified lens and sources array. In: *IEEE European Conference on Antennas and Propagation*. Berlin, Germany: [s.n.], 2009. Citado na página 15.

LAMBRECHT, A.; BEER, S.; ZWICK, T. True-time-delay beamforming with a rotman-lens for ultrawideband antenna systems. *IEEE transactions on antennas and propagation*, IEEE, v. 58, n. 10, p. 3189–3195, 2010. Citado na página 17.

Lee, R. Q. et al. Steerable space fed lens array for low-cost adaptive ground station applications. In: *IEEE Antennas and Propagation Society International Symposium*. Honolulu, HW, USA: [s.n.], 2007. Citado 2 vezes nas páginas 4 and 15.

LEE, W.; KIM, J.; YOON, Y. J. Compact two-layer rotman lens-fed microstrip antenna array at 24 ghz. *IEEE Transactions on Antennas and Propagation*, IEEE, v. 59, n. 2, p. 460–466, 2010. Citado na página 17.

Li, Y. et al. Multibeam 3-d-printed luneburg lens fed by magnetoelectric dipole antennas for millimeter-wave mimo applications. *IEEE Transactions on Antennas and Propagation*, v. 67, n. 5, p. 2923–2933, 2019. Citado na página 15.

Lv, H. et al. Holographic design of beam-switchable leaky-wave antenna. *IEEE Antennas and Wireless Propagation Letters*, v. 18, n. 12, p. 2736–2740, 2019. Citado na página 15.

McGrath, D. Planar three-dimensional constrained lenses. *IEEE Transactions on Antennas and Propagation*, v. 34, n. 1, p. 46–50, 1986. Citado na página 17.

Muraguchi, M.; Yukitake, T.; Naito, Y. Optimum design of 3-db branch-line couplers using microstrip lines. *IEEE Transactions on Microwave Theory and Techniques*, v. 31, n. 8, p. 674–678, 1983. Citado na página 34.

Musa, L.; Smith, M. Microstrip rotman lens port design. In: *Antennas and Propagation Society International Symposium*. [S.l.: s.n.], 1986. v. 24, p. 899–902. Citado na página 51.

Musa, L.; Smith, M. S. Microstrip port design and sidewall absorption for printed rotman lenses. *IEE Proceedings H - Microwaves, Antennas and Propagation*, v. 136, n. 1, p. 53–58, 1989. Citado na página 51.

ORFANIDIS, S. *Electromagnetic Waves and Antennas*. Sophocles J. Orfanidis, 2016. 449-452 p. Disponível em: <https://books.google.com.br/books?id=4n5ezQEACAAJ>. Citado na página 47.

Parikh, H.; Pandey, S.; Modh, K. Wideband and high gain stacked microstrip antenna for ku band application. In: *2012 Nirma University International Conference on Engineering (NUiCONE)*. [S.l.: s.n.], 2012. p. 1–5. Citado na página 32.

Pawlak M. S. Reuther, A. F. J. H. High isolation substrate integrated coaxial feed for ka-band antenna arrays. *Proceedings of the 37th European Microwave Conference*, 2007. Citado na página 22.

Rahimian, A. Enhanced rf steerable beamforming networks based on butler matrix and rotman lens for its applications. In: *2010 IEEE Region 8 International Conference on Computational Technologies in Electrical and Electronics Engineering (SIBIRCON)*. [S.l.: s.n.], 2010. p. 567–572. Citado na página 17.

REMEZ, E. Z. J.; ZOHAR, R. In: . [S.l.: s.n.]. Citado 3 vezes nas páginas 4, 15, and 16.

Riley, K. F.; Hobson, M. P.; Bence, S. J. Mathematical methods for physics and engineering. In: _____. 3. ed. [S.l.]: Cambridge University Press, 2006. cap. 18, p. 602. Citado na página 105.

Rondineau, S. et al. Ground stations of arrays to increase the leo download capacity. In: *IEEE European Microwave Conference*. Manchester, UK: [s.n.], 2006. Citado 2 vezes nas páginas 4 and 15.

Rondineau, S.; Himdi, M.; Sorieux, J. A sliced spherical luneburg lens. In: *IEEE Antennas and Wireless Propagation Letters*. [S.l.: s.n.], 2003. v. 2, p. 163 – 166. Citado na página 15.

Rotman, W.; Turner, R. Wide-angle microwave lens for line source applications. *IEEE Transactions on Antennas and Propagation*, v. 11, n. 6, p. 623–632, 1963. Citado 2 vezes nas páginas 17 and 50.

Sakakibara, K. et al. Design of 2d rotman-lens multi-beam antenna using multi-layer substrate integrated waveguide. In: *2018 IEEE MTT-S International Conference on Microwaves for Intelligent Mobility (ICMIM)*. [S.l.: s.n.], 2018. p. 1–4. Citado na página 17.

SANETEL. *SANETEL-S2/S3 Mobile Marine Satellite TVRO Antenna*. [S.l.], 2015. Citado na página 15.

SCHULWITZ, L.; MORTAZAWI, A. A tray based rotman lens array with beamforming in two dimensions for millimeter-wave radar. In: *2010 IEEE International Symposium on Phased Array Systems and Technology*. [S.l.: s.n.], 2010. p. 850–853. Citado 3 vezes nas páginas 4, 15, and 16.

SUÁREZ, L. F. C. *Antenas multihaz con Lente de Rotman para las bandas de microondas y milimétricas realizadas en diferentes tecnologias*. Tese (Doutorado) — Universitat Politècnica de València, 2015. Citado 2 vezes nas páginas 50 and 51.

Technologies, A. C. *03m On The Move Phased Array Antenna*. 2016. Citado na página 15.

Tsai, C. et al. Design of microstrip-to-microstrip via transition in multilayered ltcc for frequencies up to 67 ghz. *IEEE Transactions on Components, Packaging and Manufacturing Technology*, v. 1, n. 4, p. 595–601, 2011. Citado na página 22.

Wang, K. L.; Yang, K. P. Compact dual-frequency microstrip antenna with a pair of bent slots. *IET ELECTRONICS LETTERS*, v. 34, n. 3, 1998. Citado na página 39.

WEISS, S.; KELLER, S.; LY, C. Development of simple affordable beamformers for army platforms. In: *Proceedings of GOMACTech–07 Conference, Lake Buena Vista, FL*. [S.l.: s.n.], 2006. Citado na página 17.

Wu, Z.; Y.Lou; Yung, E. A circular patch fed by a switch line balun with printed l-probes for broadband cp performance. *IEEE Antennas and Wireless Propagation Letters*, v. 6, p. 608–611, 2007. Citado na página 32.

Xu, G.; Xu, H.; Jin, W. Study on stabilization and tracking for sotm. In: *2009 9th International Conference on Electronic Measurement Instruments*. [S.l.: s.n.], 2009. p. 1–240–1–244. Citado na página 15.

Zhang, C. et al. A circularly polarized metasurface antenna based on holographic method. In: *2019 International Conference on Microwave and Millimeter Wave Technology (ICMMT)*. [S.l.: s.n.], 2019. p. 1–3. Citado na página 15.

Zhou, Y. et al. Virtual channel space-time processing with dual-polarization discrete lens antenna arrays. *IEEE Transactions on Antennas and Propagation*, v. 53, n. 8, p. 2444–2455, aug 2005. Citado na página 17.

Annex

ANNEX A – Roots of Bessel Function

Zeros of the Derivatives of Bessel's Functions of the First Kind

Number of Zeros	$J'_0(x)$	$J'_1(x)$	$J'_2(x)$	$J'_3(x)$	$J'_4(x)$	$J'_5(x)$
1	3.83171	1.84118	3.05424	4.20119	5.31755	6.41562
2	7.01559	5.33144	6.70613	8.01524	9.2824	10.51986
3	10.17347	8.53632	9.96947	11.34592	12.68191	13.98719
4	13.32369	11.706	13.17037	14.58585	15.96411	17.31284
5	16.4706	14.86359	16.34752	17.78875	19.19603	20.57551

ANNEX B – Vector Identities

$$\nabla \cdot (\nabla \times \mathbf{A}) = 0$$

$$\nabla \times \nabla \psi = 0$$

$$\nabla(\phi + \psi) = \nabla\phi + \nabla\psi$$

$$\nabla(\phi\psi) = \phi\nabla\psi + \psi\nabla\phi$$

$$\nabla \cdot (\mathbf{A} + \mathbf{B}) = \nabla \cdot \mathbf{A} + \nabla \cdot \mathbf{B}$$

$$\nabla \times (\mathbf{A} + \mathbf{B}) = \nabla \times \mathbf{A} + \nabla \times \mathbf{B}$$

$$\nabla \cdot (\psi \mathbf{A}) = \mathbf{A} \cdot \nabla\psi + \psi \nabla \cdot \mathbf{A}$$

$$\nabla \times (\psi \mathbf{A}) = \nabla\psi \times \mathbf{A} + \psi \nabla \times \mathbf{A}$$

$$\nabla(\mathbf{A} \cdot \mathbf{B}) = (\mathbf{A} \cdot \nabla)\mathbf{B} + (\mathbf{B} \cdot \nabla)\mathbf{A} + \mathbf{A} \times (\nabla \times \mathbf{B}) + \mathbf{B} \times (\nabla \times \mathbf{A})$$

$$\nabla \cdot (\mathbf{A} \times \mathbf{B}) = \mathbf{B} \cdot \nabla \times \mathbf{A} - \mathbf{A} \cdot \nabla \times \mathbf{B}$$

$$\nabla \times (\mathbf{A} \times \mathbf{B}) = \mathbf{A}\nabla \cdot \mathbf{B} - \mathbf{B}\nabla \cdot \mathbf{A} + (\mathbf{B} \cdot \nabla)\mathbf{A} - (\mathbf{A} \cdot \nabla)\mathbf{B}$$

$$\nabla \times \nabla \times \mathbf{A} = \nabla(\nabla \cdot \mathbf{A}) - \nabla^2 \mathbf{A}$$

ANNEX C – Wave Equation on Cylindrical Coordinate

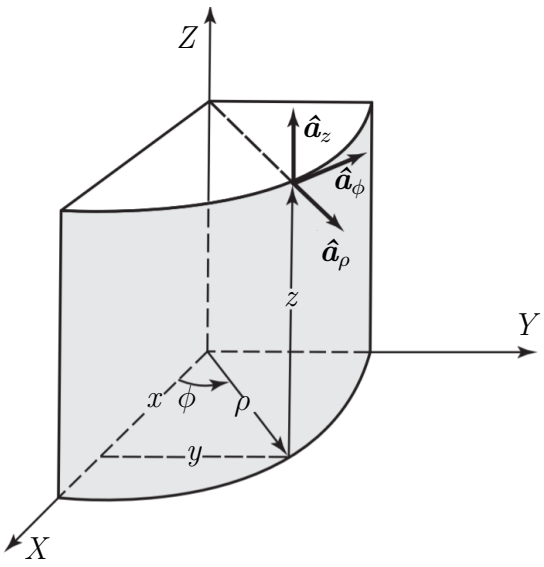

Figure 73 – Cylindrical coordinate system with corresponding unit vectors.

In (Harrington, 2001a) is that the wave equation in a lossless and sourceless medium can be written as follows,

$$\nabla^2\mathbf{E} - k^2\mathbf{E} = 0, \tag{C.1}$$

where

$$k^2 = -\omega^2\mu\epsilon. \tag{C.2}$$

The wave equation vector in cylindrical coordinates can be written as follows,

$$\mathbf{E}\big(\rho,\phi,z\big) = \hat{\mathbf{a}}_\rho E_\rho\big(\rho,\phi,z\big) + \hat{\mathbf{a}}_\phi E_\phi\big(\rho,\phi,z\big) + \hat{\mathbf{a}}_z E_z\big(\rho,\phi,z\big), \tag{C.3}$$

$$\nabla^2\big(\hat{\mathbf{a}}_\rho E_\rho + \hat{\mathbf{a}}_\phi E_\phi + \hat{\mathbf{a}}_z E_z\big) = -k^2\big(\hat{\mathbf{a}}_\rho E_\rho + \hat{\mathbf{a}}_\phi E_\phi + \hat{\mathbf{a}}_z E_z\big). \tag{C.4}$$

Expanding in three scalar EDP and using vector identity shown in the annex B, we have,

$$\nabla^2 E_\rho + \left(- \frac{E_\rho}{\rho^2} - \frac{2}{\rho^2}\frac{\partial E_\phi}{\partial\phi} \right) + k^2 E_\rho = 0, \tag{C.5}$$

$$\nabla^2 E_\phi + \left(- \frac{E_\phi}{\rho^2} - \frac{2}{\rho^2}\frac{\partial E_\rho}{\partial \phi} \right) + k^2 E_\phi = 0, \tag{C.6}$$

$$\nabla^2 E_z + k^2 E_z = 0. \tag{C.7}$$

The scalar Helmholtz equation in cylindrical coordinates (Harrington, 2001b) takes the form of,

$$\nabla^2 \psi\big(\rho, \phi, z\big) = \frac{1}{\rho}\frac{\partial}{\partial \rho}\left(\rho \frac{\partial \psi}{\partial \rho}\right) + \frac{1}{\rho^2}\frac{\partial^2 \psi}{\partial \phi^2} + \frac{\partial^2 \psi}{\partial z^2} + k^2 \psi = 0. \tag{C.8}$$

Using the method of separation of variables the solution presents the following form,

$$\psi = R(\rho)\varphi(\phi)Z(z). \tag{C.9}$$

Substituting in the equation C.8

$$\varphi Z \frac{d^2 R}{d\rho^2} + \varphi Z \frac{1}{\rho}\frac{dR}{d\rho} + RZ\frac{1}{\rho^2}\frac{d^2\varphi}{d\phi^2} + R\varphi\frac{d^2 Z}{dz^2} + k^2 R\varphi Z = 0. \tag{C.10}$$

Dividing by $R\varphi Z$, and adding the separation constant k_z.

$$\frac{1}{R}\frac{d^2 R}{d\rho^2} + \frac{1}{R}\frac{1}{\rho}\frac{dR}{d\rho} + \frac{1}{\varphi}\frac{1}{\rho^2}\frac{d^2\varphi}{d\phi^2} + \frac{1}{Z}\frac{d^2 Z}{dz^2} = -k^2. \tag{C.11}$$

$$\boxed{\frac{d^2 Z}{dz^2} + k_z^2 Z = 0} \tag{C.12}$$

Putting the equation C.12 into C.11,

$$\frac{1}{R}\frac{d^2 R}{d\rho^2} + \frac{1}{R}\frac{1}{\rho}\frac{dR}{d\rho} + \frac{1}{\varphi}\frac{1}{\rho^2}\frac{d^2\varphi}{d\phi^2} + \frac{1}{Z}(-Zk_z^2) = -k^2. \tag{C.13}$$

Multiplying by ρ^2,

$$\frac{\rho^2}{R}\frac{d^2 R}{d\rho^2} + \frac{\rho}{R}\frac{dR}{d\rho} + \frac{1}{\varphi}\frac{d^2\varphi}{d\phi^2} + \rho^2(-k_z^2 + k^2) = 0. \tag{C.14}$$

Taking the third term of the equation C.14, we can set arbitrary constant m^2.

$$\frac{d^2\varphi}{d\phi^2} + m^2\varphi = 0 \tag{C.15}$$

Multiplying the equation C.14 by R and replacing the equation C.15.

$$\rho^2\frac{d^2R}{d\rho^2} + \rho\frac{dR}{d\rho} + (k_z^2\rho^2 - m^2)R = 0 \tag{C.16}$$

Dividing by ρ^2,

$$\frac{d^2R}{d\rho^2} + \frac{1}{\rho}\frac{dR}{d\rho} + (k_z^2 - \frac{m^2}{\rho^2})R = 0. \tag{C.17}$$

Defining k_ρ,

$$k_\rho^2 = k^2 - k_z^2. \tag{C.18}$$

Inserting k_ρ into equation C.17,

$$k_z^2\frac{d^2R}{dk_\rho^2} + \frac{k_z^2}{k_\rho}\frac{dR}{dk_\rho} + k_z^2(1 - \frac{m^2}{k_\rho^2})R = 0. \tag{C.19}$$

Dividing by k_z^2,

$$\frac{d^2R}{dk_\rho^2} + \frac{1}{k_\rho}\frac{dR}{dk_\rho} + (1 - \frac{m^2}{k_\rho^2})R = 0. \tag{C.20}$$

We have three EDPs. If inhomogeneities and discontinuities of the medium are excluded, the field is necessarily periodic with respect to ϕ and the value of m is limited to the integers. Equation C.20 is Laplace equation, applying the frobenius method, the method is to look for the following form solution,

$$R(k_\rho) = \sum_{n=1}^{\infty} a_n k_\rho^{(n+\alpha)}. \tag{C.21}$$

Where α is the lowest order of power series, the conditions for the coefficients of expansion are,

$$(\alpha^2 - m^2)a_0 = 0, \tag{C.22}$$

$$[(\alpha + 1)^2 - m^2]a_1 = 0. \tag{C.23}$$

We have the following recurrence equation,

$$a_{n+2} = \frac{-1}{(n - \alpha + 2)^2 - m^2}. \tag{C.24}$$

If $a_0 \neq 0 \rightarrow \alpha = \pm m$, or $a_1 \neq 0 \rightarrow \alpha = \pm m - 1$, only one condition can be satisfied simultaneously. Taking the first condition $a_0 \neq 0$ and $a_1 = 0$.

$$R(k_\rho) = k_\rho^{\pm m}(a_0 + a_2 k_\rho^4 ...), \tag{C.25}$$

for $\alpha = m$ implies,

$$a_{2j} = \frac{(-1)^j}{2^{2j} j! \prod_{n_2=1}^{j}(m + n_2)}. \tag{C.26}$$

The uniqueness theorem tells us that in space-time there can be only one solution for the vector field **E**. It also means to state that m can assume only integer values. So the product simplifies to the factorial.

For integer values of m, making $m_2 = m$,

$$\prod_{n_2=1}^{j}(m_2 + n_2) = \frac{(m_2 + j)!}{m_2!}, \tag{C.27}$$

a_{2j} take the form,

$$a_{2j} = \frac{(-1)^j m_2!}{2^{2j} j!(m_2 + j)!} a_0. \tag{C.28}$$

For non-integer m the gamma function C.29 and its identity C.30 are used,

$$\Gamma(x) \equiv \int_0^\infty t^{x-1} e^{-t}\, dt, \quad \Re(x) > 0, \tag{C.29}$$

$$\Gamma(x + 1) = x\Gamma(x), \tag{C.30}$$

For arbitrary argument,

$$\Gamma(x+j+1) = (x+j)(x+j-1)(x+j-2)...(x+2)(x+1)\Gamma(x+1). \tag{C.31}$$

Replacing in the equation C.27,

$$\prod_{n_2=1}^{j}(m+n_2) = (m+1)(m+2)...(m+j-1)(m+j) = \frac{\Gamma(m+j+1)}{\Gamma(m+1)} \tag{C.32}$$

a_{2j} for non-integer m takes the following form,

$$a_{2j} = \frac{(-1)^j}{2^{2j}j!}\frac{\Gamma(m+1)}{\Gamma(m+j+1)}a_0. \tag{C.33}$$

Replacing in the equation C.21,

$$R(k_\rho) = a_0\Gamma(m+1)2^m\sum_{j=0}^{\infty}\frac{(-1)^j}{j!\Gamma(m+j+1)}\left(\frac{k_\rho}{2}\right)^{m+2j}. \tag{C.34}$$

a_0 can be broadly defined as,

$$a_0 = \frac{1}{2^m\Gamma(1+m)}. \tag{C.35}$$

Replacing in the equation C.34, thus the term that precedes the sum becomes unitary and we have the so-called Bessel function of the first kind of index m. It is known as J_m,

$$J_m = \sum_{j=0}^{\infty}\frac{(-1)^j}{j!\Gamma(m+j+1)}\left(\frac{k_\rho}{2}\right)^{m+2j}. \tag{C.36}$$

For non-integer m, the second solution can be obtained by replacing m with $-m$. The proof is found in reference (Riley; Hobson; Bence, 2006), and generates the following solution for the second kind Bessel function,

$$N_m(k_\rho) = \frac{cos(m\pi)J_m - J_{-m}(k_\rho)}{sin(m\pi)}. \tag{C.37}$$

The solution to the Bessel equation takes the form C.38 where C_1 and C_2 are constants to be defined by the boundary constraints of the initial value problem (PVI),

$$R(\rho) = C_1J_m(k_\rho) + C_2N_m(k_\rho). \tag{C.38}$$

For each of the equations there are two solutions $R(\rho)$, $\varphi(\phi)$ and Z(z). All are valid solutions, however for later solution of the cavity method it is more appropriate to choose the following form,

$$\psi = R(\rho)\varphi(\phi)Z(z), \tag{C.39}$$

$$\varphi(\phi) = C_3 sin(m\phi) + C_4 cos(m\phi), \tag{C.40}$$

$$Z(z) = C_5 e^{-jk_z z} + C_6 e^{+jk_z z}, \tag{C.41}$$

$$\psi = \Big[C_1 J_m(k_\rho) + C_2 N_m(k_\rho)\Big]\Big[C_3 \sin(m\phi) + C_4 \cos(m\phi)\Big]\Big[C_5 e^{-jk_z z} + C_6 e^{+jk_z z}\Big]. \tag{C.42}$$

ANNEX D – Duality between time-domain and space-domain signal processing

discrete-time signal processing	discrete-space array processing
time-domain sampling $t_n = nT$	space-domain sampling $x_n = nd$
sampling time interval T	sampling space interval d
sampling rate $1/T$ [samples/sec]	sampling rate $1/d$ [samples/meter]
frequency Ω	wavenumber k_x
digital frequency $\omega = \Omega T$	digital wavenumber $\psi = k_x d$
Nyquist interval $-\pi \le \omega \le \pi$	Nyquist interval $-\pi \le \psi \le \pi$
sampling theorem $\Omega \le \pi/T$	sampling theorem $k_x \le \pi/d$
spectral images	grating lobes or fringes
frequency response $A(\omega)$	array factor $A(\psi)$
z-domain $z = e^{j\omega}$	z-domain $z = e^{j\psi}$
transfer function $A(z)$	transfer function $A(z)$
DTFT and inverse DTFT	DSFT and inverse DSFT
pure sinusoid $e^{j\omega_0 n}$	narrow beam $e^{-j\psi_0 n}$
windowed sinusoid $w(n)e^{j\omega_0 n}$	windowed narrow beam $w(n)e^{-j\psi_0 n}$
resolution of multiple sinusoids	resolution of multiple beams
frequency shifting by AM modulation	phased array scanning
filter design by window method	array design by window method
bandpass FIR filter design	angular sector array design
frequency-sampling design	Woodward-Lawson design
DFT	Blass matrix
FFT	Butler matrix